UNIVERSITY OF CALIFORNIA,
IRVINE

Silver-Based Bonding Systems for Heterogeneous Integration of High-Power Photonics

DISSERTATION

submitted in partial satisfaction of the requirements
for the degree of

DOCTOR OF PHILOSOPHY

in Engineering

by

Roozbeh Sheikhi

Dissertation Committee:
Professor Frank Shi, Chair
Professor Chin C. Lee
Professor James Earthman

2021

DEDICATION

To

my amazing wife and caring family who have offered me unconditional love and support and made it possible for me to complete this work.
Thank you.

TABLE OF CONTENTS

LIST OF FIGURES

Page

LIST OF TABLES

ACKNOWLEDGEMENTS

I have had the honor to learn and work among some of the most knowledgeable and caring individuals over the past few years. Without the continuous support of these truly amazing mentors and friends, finishing my PhD. studies would have not been possible.

I would like to express my deepest gratitude to Professor Chin C. Lee. He gave me the opportunity to work on a very interesting project and provided immense insights on how to perform a well-organized research project. Despite many obstacles, he never shied away from supporting me, hence I am truly grateful to him.

I would also like to express my appreciation to Professor Frank Shi, who has been providing me with insightful guidance on the direction of my research project. Professor Shi broadened my understanding of electronics packaging and provided me with knowledge necessary to conclude my PhD. studies and to hopefully grow in my future career.

I would also like to thank my PhD. committee members, Professor James Earthman and Professor Daniel R. Mumm for their insightful comments on my research at different stages of my PhD. journey.

I would also like to thank my very good friend Dr. Yongjun Huo. He has been a great friend and mentor to me for the past few years and have been instrumental in successful implementation of this research project. Moreover, I am grateful to my colleagues and friends Jielin Guo, Jack Ngo, Dr. Jiaqi Wu, Dr. Shao-wei Fu and yipin Wu, for providing their expertise and valuable insight. In addition, I am also appreciative to IMRI staff members, Dr. Jian-Guo Zheng and Dr. Qiyin Lin for teaching me various experimental techniques. I am also grateful to the administrative staff of Materials and Manufacturing Technologies program

and department of Electrical Engineering and Computer Science at UC Irvine for enabling me to carry out this research project.

Lastly, I am exceptionally grateful to my wife, family and friends. They have always supported me and provided me invaluable advice. Their limitless support and encouragement kept me motivated throughout my studies and has enabled me to conclude my PhD. journey. I am forever grateful to you all.

VITA

Roozbeh Sheikhi

2013 Bachelor of Science

Materials Science and Engineering

Iran University of Science and Technology

2015 Master of Science

Materials Science and Engineering

Sharif University of Technology

2021 Doctor of Philosophy in Engineering

Materials and Manufacturing Technology

University of California, Irvine

PUBLICATIONS

Journal Publications

- Roozbeh Sheikhi, Yongjun Huo, Frank G. Shi, and Chin C. Lee. "Low Temperature VECSEL-to-Diamond Heterogeneous Integration with Ag-In Spinodal Nanostructured Layer." *Scripta Materialia* 194 (2021): 113628.
- Roozbeh Sheikhi, Yongjun Huo, Chin-Hao Tsai, C. R. Kao, Frank G. Shi, and Chin C. Lee. "Prior-to-bond annealing effects on the diamond-to-copper heterogeneous integration using silver–indium multilayer structure." *Journal of Materials Science: Materials in Electronics* 31, no. 10 (2020): 8059-8071.
- Roozbeh Sheikhi and Junghyun Cho. "Growth kinetics of bismuth nickel intermetallics." *Journal of Materials Science: Materials in Electronics* 29, no. 22 (2018): 19034-19042.

Conference proceedings

- Roozbeh Sheikhi, Yongjun Huo, and Chin C. Lee. "Fluxless bonding technique of diamond to copper using silver-indium multilayer structure." In *2019 IEEE 69th Electronic Components and Technology Conference (ECTC)*, pp. 150-156. IEEE, 2019.
- Junghyun Cho, Roozbeh Sheikhi, Sandeep Mallampati, Liang Yin, and David Shaddock. "Bismuth-based transient liquid phase (TLP) bonding as high-temperature lead-free solder alternatives." In *2017 IEEE 67th Electronic Components and Technology Conference (ECTC)*, pp. 1553-1559. IEEE, 2017.
- Roozbeh Sheikhi, Sandeep Mallampati, Russel Tobias and Junghyun Cho. "Bismuth-Nickel transient liquid phase bonds for high temperature electronics." In *2016 MRS Fall Meeting and Exhibit*, 2016.

ABSTRACT OF THE DISSERTATION

Silver-Based Bonding Systems for Heterogeneous Integration of High-Power Photonics

by

Roozbeh Sheikhi

Doctor of Philosophy in Engineering

Materials and Manufacturing Technology

University of California, Irvine, 2021

Professor Frank Shi, Chair

The rapid development of miniaturized and high power electronic and optoelectronic devices has led to significant technological and societal changes during the past few decades. In order for these advancements to carry on, there is need for new materials with superior thermal, electrical and mechanical characteristics that are also compatible with existing high throughput manufacturing capabilities.

In electronic and optoelectronic assemblies, the overall performance and reliability of the device is dependent on the active die and the housing surrounding it. The housing also known as the package is comprised of different components. One of these components is the die attach material that provides mechanical adhesion, electrical conductivity (if needed) and thermal path between the die and its substrate. This dissertation implements Ag-In and Nano-Ag sintering as novel bonding technologies for packaging of high-power photonic

devices. Implementation of these two systems is shown to enhance the performance of high-power semiconductors lasers and Light Emitting Diodes (LEDs) respectively.

In chapters three and four, Ag-In bonding technology is developed for packaging of high power Vertical External Cavity Surface Emitting Lasers (VECSELs). The package consists of a VECSEL chip, diamond heat spreader and copper heat sink all integrated by multi-layer Ag-In bonding layers. Low temperature heterogeneous integration with diamond is the key technology in pushing upwards the high-power limit of VECSELs. This work successfully demonstrates a functional high-power VECSEL-to-diamond device with a modified Ag-In transient liquid phase (TLP) bonding technology. The proposed Ag-In bonding technology provides a low-temperature process that suppresses thermally activated diffusion and thermo-mechanical stress to the minimal level within the epitaxial layers while optimizing the heat-spreading capability of the diamond. The final joint is a very thin, void free joint that provides an effective heat dissipation path in the package. Interestingly, with experimental and thermodynamic evidence, a distinct nanostructure from spinodal decomposition has been discovered in the Ag-In bonding layer for the first time, whose structural feature is beneficial to the reliability of a VECSEL-to-diamond device. Conceptually, this work opens a new bonding technology category, i.e., Ag-In spinodal bonding.

Chapter four implements the same Ag-In bonding technology for integration of CVD diamond and copper heat sinks. This chapter is focused on the undersupply of molten In during bonding, an issue that results in voiding in the bonding layer. Consequently, increasing the Ag grain size is explored as a possible solution for slowing the diffusion of In into Ag and resolving the aforementioned drawback of Ag-In system.

In chapter five, nano Ag sintering is implemented as a die attach material with the goal of enhancing the performance of high-power LEDs. A new formulation for synthesis of Ag nanoparticles (AgNp) is suggested and a low temperature sintering process is introduced. The developed bonding layer is very thin and is shown to enhance the luminance performance of the LED by providing improved heat dissipation compared to commercially available LED packages using Ag epoxy. This chapter provides the preliminary results that show the promising capabilities of this system and paves the way for further studies using this boding technique.

In the final chapter, a brief overview of design principles of a vacuum bonding chamber for laboratory-scale bonding applications is provided. This chapter aims to document the design steps and features of the chamber that was designed and built in early days of the authors PhD studies. This bonding chamber was used extensively throughout the experimental activities that resulted in the findings presented in the dissertation.

Chapter 1

Introduction

1.1 Electronics packaging

Today's electronics devices are smaller, faster, more powerful and reliable. The Electronic packaging technology is crucial for achieving these technological advancements. The performance of electronic systems as well as their reliability and cost are determined not only by the electrical design but also by the packaging materials. Electronics packaging refers to the packaging of integrated circuit (IC) chips (dies), their interconnection for signal and power transmission and heat dissipation. Packaging materials serve as electrical conductors or insulators, provide structure and form, provide thermal paths and protect the circuitry from environmental factors such as moisture, contamination, hostile chemicals and radiation.

As the speed and power of device increases, heat dissipation problems arise that can limit the performance of the electronics, these issues need to be resolved. The solution involves the devising of innovative packaging schemes and the continuing search for more advanced materials. Hierarchically, electronic packaging begins from the interface of a semiconductor chip, which is considered as the first-level or chip-level packaging, to higher level packaging such as board-level and system package leads, and the encapsulation [1].

1.2 Semiconductor package structure

Initially a review of different components in a typical IC package is presented. Although the focus of this dissertation is packaging of optoelectronic devices, there are many overlaps in terms of materials and technologies between IC and optoelectronics packaging. Thus, it is beneficial to review the conventional IC packaging at the first step.

A package consists of the semiconductor die mounted and interconnected to a substrate with metal traces that is encapsulated to seal and protect the device from the environment. The electronic package must serve four functions: (1) Provide electrical interconnection to and from the chip (2) Act as an electrical space spreader to take electronic functionality from the dense surface of the chip to the coarser pitched outside world. (3) Isolate the semiconductor die from environmental effects and (4) Provide a path for conduction of heat away from the device.

Here the focus is on the first level packaging that is where the die is bonded onto a substrate. The bonding can take place with a conductive or non-conductive adhesive layer. Electrical interconnection is made possible through a variety of materials and techniques. Interconnection can take place through wirebonds, conductive pillars/posts, solders or conductive epoxy-based adhesives. After bonding of active semiconductor die onto the carrier, the encapsulant can be applied as a molding cap to protect the die from environmental effects. In the flip chip design where interconnection takes place through conductive posts, the chip is flipped and the active side of chip with input/ouput pads is facing the substrate. This is in contrast to the wirebond scheme where input/output pads are facing up. Also in the case of flip chip packaging, an epoxy based underfill layer can be

added to protect the fragile, fine chip bonding/solder posts from mechanical shock and fatigue [2][3]. Typical wirebond and flip chip packaging structures are shown in figure 1.1. Cost, performance, and package size are the principal drivers in selecting the type of packaging. For example, applications such as portable consumer electronics often require small form factor and high-speed thus in these circumstances the flip-chip packaging is the better solution. In other cases, typically where interconnection input/output is lower, the existing infrastructure, flexibility and material costs of wire bonding provides advantages [4] [5].

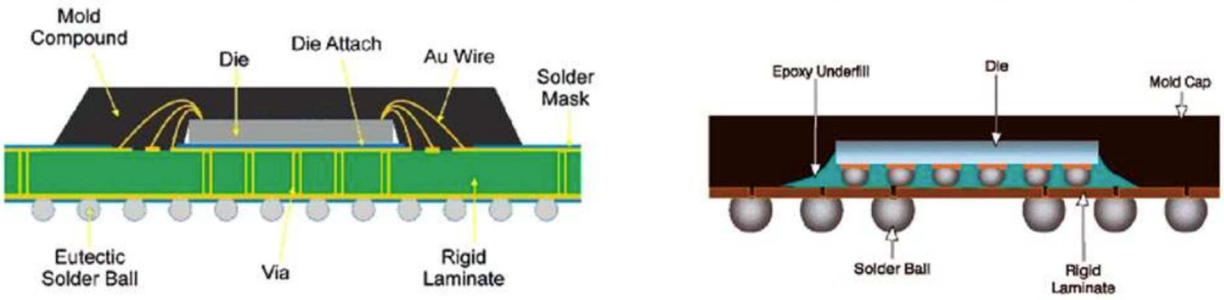

Figure 1.1 Typical first level package structure (left) wirebond package (right) flip chip package, source: Amkor

1.3 Die-attach materials in package

Die-attachment systems provide the needed mechanical adhesion between the die and the substrate. This is the fundamental task of a die attach material. Moreover, electrical interconnection for some cases with good thermal path for heat dissipation is necessary based on the specific applications. Die-attachment materials should also be mechanically robust to survive the field use conditions, for example in case of dropping a device, the functionality will be dependent on the survival of the joint/die attach layer. Thus, it can be

argued that the overall performance, reliability and lifetime of the electronic system is dependent on the bonding materials and technologies being used in the package. Therefore, die-attachment materials, which connect the chip and device to the rest of the electronic system, play a crucial role to ensure system works consistently. In words, die-attachment materials and technology are extremely important to the development of electronic packaging technology. Table 1.1 provides an overview of the current material solutions that are being used within the domain of electronics packaging. Since the present study is focused on high power optoelectronics packaging, in following sections a detailed description of die attach systems that are mostly common in high power laser packaging will be discussed.

Table 1.1 common die attach materials used in electronic packaging

Die-attachment material	Melting temperature (°C)	Remark
Electrically conductive adhesive (ECA) [Ag filled epoxy]	100	Pro: Low processing cost, high conductivity Con: Not compatible for high temperature electronics
Eutectic lead-tin solder [Sn63Pb37]	183	Pro: low melting point, good flowability Con: RoHS restrictions due to environmental and health concerns of lead
Lead free solder (SAC) [SnAgCu]	217	Pro: High working temperature Con: Formation of intermetallics and high fabrication temperature
Eutectic gold-tin [Au80Sn20]	280	Pro: High thermal conductivity and excellent mechanical properties Con: high fabrication temperature
In	157	Pro: very low fabrication temperatures Con: prone to creep
Sintered nano-silver	961	Pros: high thermal and electrical conductivity Con: expensive and excessive voiding

1.4 Semiconductor lasers

In this section a brief discussion on the origin of lasing in semiconductor lasers is provided. Semiconductor lasers use a semiconductor material as the gain medium. The physical origin of gain in a semiconductor is shown in figure 1.2. Without pumping, most of the electrons are in the valence band. Assuming pumping using an optical source, a pump beam with a photon energy slightly higher than the bandgap energy of gain medium can excite electrons into a higher state in the conduction band, from where they quickly decay to states near the bottom of the conduction band. At the same time, the holes generated in the valence band move to the top of the valence band. Electrons in the conduction band can then recombine with these holes, emitting photons with an energy near the bandgap energy. This process can also be stimulated by incoming photons with suitable energy.

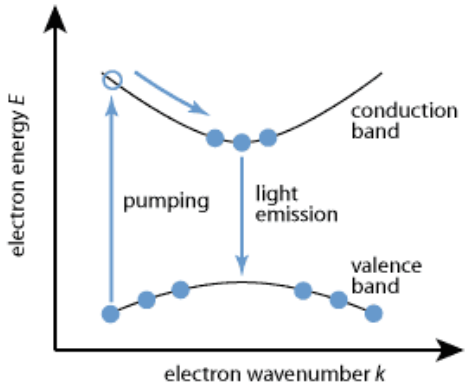

Figure 1.2 Physical origin of gain in semiconductor lasers, source: www.rp-photonics.com/semiconductor_lasers

Semiconductor lasers are fabricated on polished semiconductor wafers with lithographic techniques. Common semiconductor materials for the active regions are GaAs, AlGaAs, GaP, InGaP, GaN, InGaAs, InP, and GaInP. A wide range of wavelengths can be achieved and much of the visible, near-infrared, and midinfrared spectral region can be covered.

Electron-hole pairs in these devices can either be generated by an electrical or an optical source/pump. In electrically pumped laser diodes, electron-hole pairs are generated by an electrical current in a region where n-doped and p-doped semiconductor materials meet. In optically pumped semiconductor lasers, carriers are generated by absorbed pump light. Semiconductor lasers are the most important type of lasers currently being used. They have widespread applications in optical telecommunications, optical data storage, medical treatments, metrology, spectroscopy and material processing [6][7].

1.4.1 VECSEL

Structurally, the VECSEL chip is made of a highly reflective mirror and a semiconductor gain region that can be coupled with an external cavity mirror. The gain region usually includes several quantum-well (QW) layers that are separated by spacer or barrier layers. The typical mirror structure is a semiconductor distributed brag reflector (DBR). DBR consists of alternating layers of GaAs/AlAs. In general, the single pass gain of a vertical cavity QW device is quite small due to the short interaction length between the laser mode and the gain material. Hence, the small gain is usually compensated by using a large number of QWs and by maximizing their coupling with the laser mode. This is achieved by placing the QWs periodically at the antinodes of the optical standing wave. Such resonant periodic gain (RPG) architecture has historically been employed in light-emitting devices. If the QWs introduce large strains into the structure, strain compensation layers are usually placed at the nodes of the optical field. These strain compensating layers can also act as barriers, confining the pump-generated carriers to a specific QW [8].

VECSELs are usually optically pumped (OP-VECSEL), although electrical pumping can also be employed. There have been significant challenges with developing electrically pumped VECSELs due to the requirement for high-quality doped DBRs and the difficulties in injecting carriers uniformly over a large area. These limitations are avoided in optically pumped VECSELs, which permit the use of uniform carrier excitation over a large area. [9]

1.4.2 Thermal management of OP-VECSEL

In the VECSEL chip only a portion of pump energy is converted into useful photons, while a significant part of it is transferred to phonons via non-radiative recombination and thermalization due to quantum defects. These effects can lead to excessive heating with increasing pump power, which then reduce the emission efficiency even further via increased non-radiative recombination and carrier leakage [10].

In addition to the reduced emission efficiency, heating will have other undesirable effects on the performance of VECSELs. As heating of the RPG occurs, red-shift in emission wavelength will happen. This can lead to a mismatch between the emission wavelength and the resonant periodic gain structure. Eventually, the output power of a VECSEL will exhibit a thermal roll-over with increased pump power. Thus, for achieving high power operation it is critical to maximize the heat transfer away from the gain region. In addition to effective heat removal, heat generation should also be minimized by reducing the quantum-defect and non-radiative processes within the active region [10][11]. The need for significant heat dissipation can be addressed by utilizing innovative package designs and materials. This will be discussed further in the next section.

1.4.3 Package design of OP-VECSEL

Packaging of the VECSEL can play a key role in effective heat dissipation and therefore the overall performance of the device. Two methods are commonly used for efficient thermal dissipation in VECSELs. Both of these approaches place a high thermal conductive heat spreader element between the gain mirror and the heat sink. These two methods are shown schematically in figure 1.3. The so-called 'intracavity heat spreader' method places a transparent heat spreader element onto the gain mirror. Diamond is by far the best material for this purpose, owing to its high thermal conductance (up to ~2000 W $m^{-1} \cdot K^{-1}$) and wide transmission window, the drawback in this case is the high cost of transparent CVD diamond and possible modulation of output laser beam while passing through the heat spreader.

Another option for effective heat dissipation is schematically shown in figure 1.3 (right) and is known as the flip-chip configuration. In the flip-chip configuration, a reversely grown (first DBR mirror and then gain structure grown) epitaxial chip is bonded onto a diamond heat spreader, then, the initial GaAs substrate is completely removed by wet etching and only the DBR and gain region are remained bonded onto the diamond. For GaAs substrate removal, one can use InGaP or Al(Ga)As etch stop layers and NH_4OH:H_2O_2 based etchants. After the substrate removal, the remained active epitaxial membrane (thickness < 10 μm) is extremely fragile. Therefore, the heterogeneous bonding joint is essential to the performance and long-term reliability of a VECSEL device, whose thickness is a crucial parameter to consider in the package design [12]. Specifically, a thinner joint is highly preferred for enhancing the heat transportation [13] [14] whereas a thicker joint facilitates the management of thermo-mechanical stresses induced by the coefficient of thermal expansion (CTE) mismatch (see

table 1.2 for CTE values) between the compound semiconductor and diamond [15]. A low temperature bonding process would mitigate the thermo-mechanical stress level to allow a thinner joint without causing further issues, such as micro-cracks generation or stress induced peak-shift [16]. Thus, a low temperature bonding process is inherently beneficial to the VECSEL-to-diamond heterogeneous integration, whereby pushing the thermal dissipation limits with an ultra-thin bonding layer.

After assembling the VECSEL onto the diamond, the backside of the diamond can be bonded onto a Copper heat sink for further extraction and spreading of the heat generated within the active region. Thus, in total two bonding steps need to be carried out and for each bonding layer, considerations need to be made in order to have reliable joints. For example, for the case of diamond to copper integration the difference in CTE is high (14 ppm K^{-1}) and thus a thicker joint capable of managing the mismatch between the two components is needed. This joint will be further discussed in chapter 4.

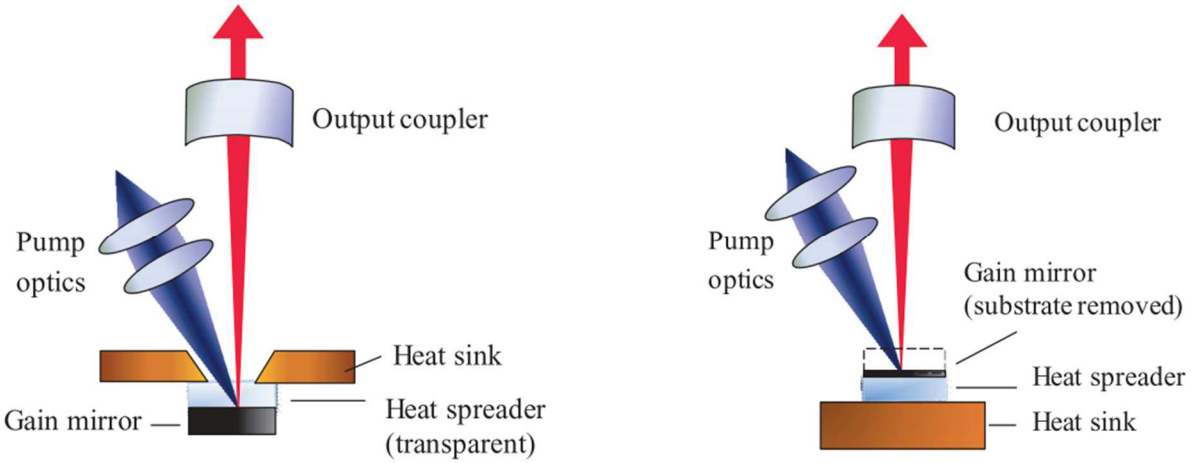

Figure 1.3 common strategies used for heat extraction of OP-VECSELs. (left) gain chip with intra cavity heat spreader. (right) flip-chip device with GaAs substrate removed [10]

Table 1.2 properties of different components within the OP-VECSEL assembly

Material	Thermal Conductivity ($Wcm^{-1}K^{-1}$)	CTE (ppm K^{-1})	
DBR (GaAs/AlAs)	0.67	GaAs: 6.86	AlAs: 4.9
RPG	0.24	-	
Diamond heat spreader	20	1.5	
Copper	4	15.5	
Gold-tin eutectic (Au80Sn20)	0.57	16	

1.5 Die attach materials for VECSEL packaging

1.5.1 Indium

Traditionally, Indium has been the most commonly used bonding material for laser diode packaging, but it suffers from severe creep and thermal fatigue issues due to its low yield strength. Indium solder is mostly advantageous in laser die bonding especially when optical coupling is not required, or the tolerance of optical coupling is large. Indium is a soft solder that can relieve the stresses caused by mismatch in CTE between the laser chip and mounting substrate. Indium has low melting temperature of 157°C, thus a low temperature bonding can be carried out by Indium which results in minimal thermal induced stresses in the laser epitaxial layer. It is also easy to use and is very low cost. There have been studies reporting sudden failures caused by electromigration of indium solder at high testing currents.[17]

1.5.2 Eutectic gold-tin (Au80Sn20)

Eutectic Au80Sn20 (wt %) bonding overcomes the disadvantageous thermal fatigue and creep rupture properties of soft solders, such as In, by staying in elastic deformation region,

although these same properties, on the other hand, could lead to high stresses due to the inability to relieve the stresses through plastic deformation developed throughout the bonding. The binary phase diagram for Au-Sn is shown in figure 1.4. The most important features of the Au-Sn binary system are steep liquidus lines on the Au-rich side of the eutectic composition (Au 71 at% Sn 29 at%) and the numerous intermetallic compounds existing at room temperature.

Eutectic composition is selected for bonding applications since it provides the lowest processing temperature possible. These solders can be applied in the form of preforms, pastes or plated layers on top of bonding pads with Au metallization. The resulting solder joint will have a melting point much higher than 280ºC due to diffusion of the Au metallization into the solder layer [18]. The fact that these joints can withstand high

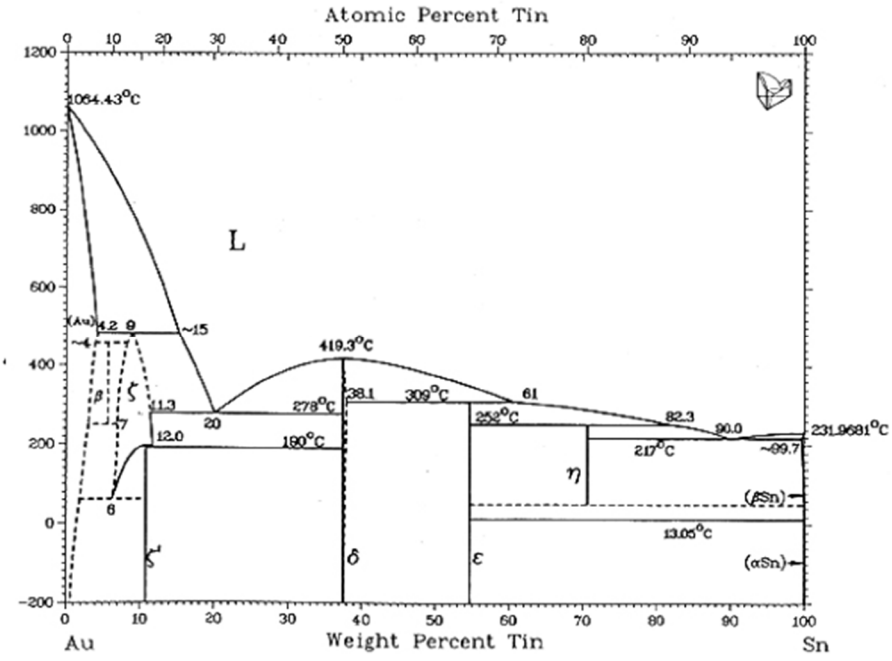

Figure 1.4 Au-Sn binary phase diagram [19]

temperatures have made gold-tin eutectic bonding a compelling choice for the high temperature electronics as well.

All of the intermetallic compounds on the Sn-rich side of the diagram are compounds with very limited solubility ranges. These compounds usually have high strength and creep resistance while suffering from low ductility. On the other hand, the eutectic phases exhibits moderate ductility while having excellent creep resistance, making it a very good choice as a die attach material [18][19]. Figure 1.6 shows the eutectic microstructure composed of lamella of Au_5Sn and AuSn.

Moreover gold-tin eutectic joints provide high thermal conductivity which is advantageous in packages with high heat dissipation needs. A major drawback with this bonding technique is the rather high processing temperatures needed. The bonding usually takes place at temperatures between 300°C and 350°C. This high processing temperature can induce thermomechanical stresses within the die and the substrate. If these stresses are high enough, die cracking and delamination in between epitaxial layers of the VECSEL chip can occur.

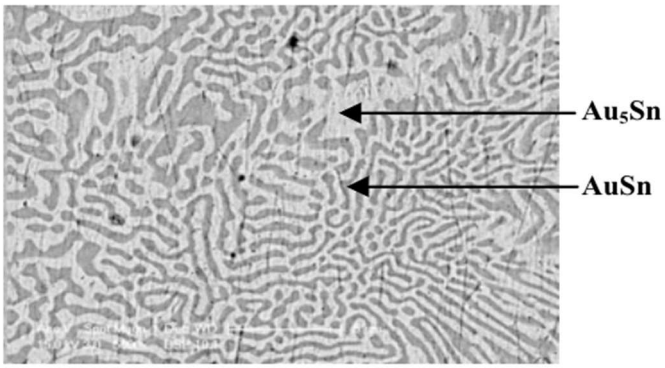

Figure 1.5 SEM image of the Au-Sn solder showing the eutectic microstructure [18].

1.5.3 Role of metallization layer

Metallization layer acts as an intermediate layer between the components and the bonding material/layer. Metallization plays a key role in ensuring adequate adhesion between the die and the substrate. The adhesion layer is particularly necessary when bonding semiconductors and ceramics using metallic systems, since most metals do not adhere directly with these covalent materials. Contact and adhesion layers can be avoided while bonding metal substrates due to the inherently good adhesion between metallic layers. In addition to adhesion layers, a diffusion barrier can also be incorporated, these layers must bond well to the contact layer and be either non-reactive to the solder material or thick enough so that they are not fully consumed during reflow and subsequent aging processes. A final cap layer can also be added to prevents oxidation of the surface prior to bonding. For AuSn solders, this layer is always Au.

[Ti/Pt/Au], [Cr/Pt/Au] and [Ti/W(N)/Au] are most common metallization layers that are being used for GaAs substrates while utilizing Au-Sn bonding systems. Figure 1.6 shows a representative design for metallization lasers that are commonly used for integration of GaAs and submount [20] [21] [22].

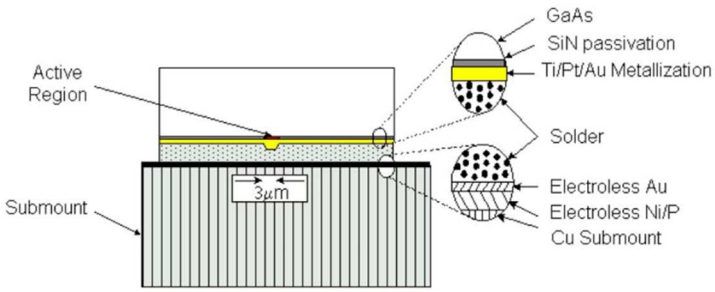

Figure 1.6 Cross-section of solder and metallization layers in an edge-emitting GaAs laser diode [20].

1.6 Ag-In bonding

Silver-based die-attachment is an excellent candidate for high-power and high temperature electronics packaging applications, due to the fact that silver has the highest electrical and thermal conductivity among all metallic materials. In this dissertation the main focus is on Ag-In bonding technology. However, nano-silver sintering will also be discussed in chapter 5.

Our research group has been actively engaged on the study of Ag-In binary system for bonding applications for the past two decades [23]. The principle of transient liquid phase (TLP) bonding can be applied to the Ag-In bonding system and thus joints made at low temperature while capable of surviving high operating temperatures can be achieved. This characteristic of Ag-In system has led our research group to develop a variety of Ag-In based bonding techniques for high temperature and high-power applications. In the following a brief overview of Ag-In binary system, its characteristics and applications in electronics packaging is provided.

Generally, based on the ratio of Ag and In in the system, bonding temperature and time, different phases can be attained in the joint microstructure. There are two major types of intermetallic compounds in this system, Ag_2In and $AgIn_2$, which are brittle in nature and can be detrimental to the overall mechanical integrity of the bonding structure [23][24]. In addition to the intermetallic compounds, solid solutions of (Ag) and (In) can also be formed. Earlier research by our group has indicated that the mechanical properties of silver rich solid solution phase, designated as (Ag), are superb, due to the fact that this solid solution phase exhibits lower yield strength and much higher values of elongation and ultimate tensile

strength (UTS), compared with pure silver [25]. This characteristic can be of great advantage in electronics packaging applications since such a tough joint can provide significant energy absorption capability and subsequent resistance to fracture and shock. Moreover, it has been shown that silver-indium solid solution phase exhibits superior anti-tarnishing properties [26], which can resolve the tarnishing issues associated with incorporation of pure silver. Therefore, Ag-In bonding technology and specially the solid solution phase can be a suitable material candidate for die attachment in high-power devices. Improved joint shear strength through conversion of intermetallic compounds into solid solution phase in the Ag-In system has been demonstrated in earlier publication by our research group [27].

Ag-In phase diagram is shown in figure 1.7 and a brief overview of different compounds within this binary system is provide. (Ag) and (In) are two solid solution phases. (Ag) can take up to 20 at. % indium. The solidus temperature varies from 962°C for pure silver to

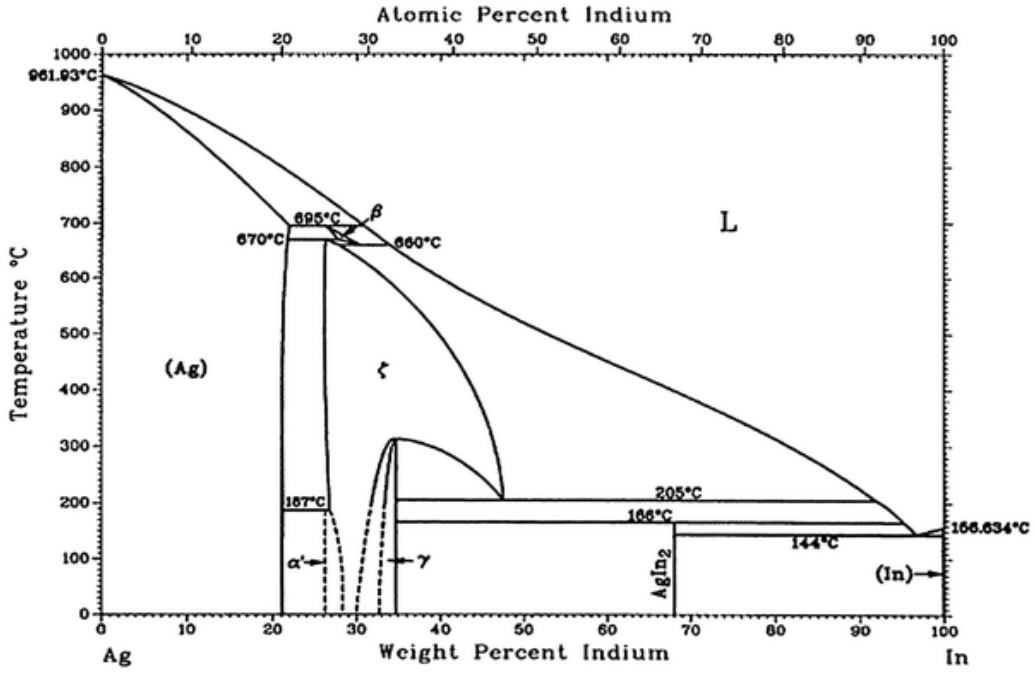

Figure 1.7 Ag-In binary phase diagram [28]

695°C for (Ag) with 20% In. The (In) phase contains less than 1% Ag. A eutectic reaction occurs at 144°C with 96.8 at. % In. Under the 144°C solidus line, the alloys with In compositions above 66.7 at. % are a mixture of $AgIn_2$ IMC and In. As the temperature rises above 144°C, the molten phase becomes a mixture of $AgIn_2$ grains and the molten phase.

At 166 °C, the $AgIn_2$ begins to decompose into (L) and Ag_2In, also designated as γ phase, until 205°C. Above 205 °C, the alloy with In composition ranging from 46 to 92.2 at. % converts to a mixture of (L) phase with ζ grains. At 205 °C, ζ phase decomposes into Ag_2In and (L) due to metatectic reaction. Relevant compositional data for the Ag-In system is also shown in table 1.3 [24] [28].

Findings of current study has resulted in a better understanding of the Ag rich side of the phase diagram. Specifically, spinodal decomposition was observed at Ag 70 at. % composition range. This observation changes the Ag-In phase diagram as published in the literature. A more detailed analysis of the spinodal decomposition within the Ag-In system will be provided in chapter 3.

Table 1.3 Summary of phases within Ag-In binary system [28]

Phase	Composition, wt% In
α(Ag)	0 to 22.1
β	26.2 to 31.3
α′ (Ag_3In)	26
ζ	26.2 to 47.4
γ(Ag_2In)	32.5 to 35.0
φ($AgIn_2$)	68.1
(In)	100

At different points within this dissertation, the Ag-In bonding will be referred to as a transient liquid phase (TLP) bonding technique. In the Transient liquid phase (TLP) bonding

process the molten phase at the bond interface solidifies by diffusion and not by decreasing the temperature below the melting temperature of the molten phase, this is also called isothermal solidification. This enables low process temperatures while providing much higher remelt temperature after the bonding process. In the context of Ag-In system, the indium interlayer is a low melting point material that moves into the lattice and grain boundaries of the high melting point material, silver. The resultant phase can be either intermetallic compounds or the (Ag) solid solution phase that are both capable of withstanding temperatures higher than the initial bonding temperature.

References

[1] R. Agarwal, P. McCluskey, D. Dishongh, S. Javadpour, and R. Mahajan, "Electronic Packaging Materials and their Properties," *IEEE Electrical Insulation Magazine*, vol. 17, no. 5. p. 60, 2001.

[2] K. Snowdon, … C. T.-2000 P. 50th, and undefined 2000, "Lead free soldering electronic interconnect: Current status and future developments," *ieeexplore.ieee.org*.

[3] J. Lau, *Low cost flip chip technologies : for DCA, WLCSP, and PBGA assemblies*. New York: McGraw-Hill, 2000.

[4] D. Frear, "Packaging materials," in *Springer Handbooks*, Springer, 2017, p. 1.

[5] H. M. Tong, Y. S. Lai, and C. P. Wong, *Advanced flip chip packaging*, vol. 9781441957. Springer US, 2013.

[6] J. L. Jewell, Y. H. Lee, J. P. Harbison, A. Scherer, and L. T. Florez, "Vertical-Cavity Surface-Emitting Lasers: Design, Growth, Fabrication, Characterization," *IEEE J. Quantum Electron.*, vol. 27, no. 6, pp. 1332–1346, 1991.

[7] J. V. Moloney, J. Hader, and S. W. Koch, "Quantum design of semiconductor active materials: Laser and amplifier applications," *Laser and Photonics Reviews*, vol. 1, no. 1. pp. 24–43, 2007.

[8] Y. Barbarin *et al.*, "Electrically pumped vertical external cavity surface emitting lasers suitable for passive modelocking," *IEEE J. Sel. Top. Quantum Electron.*, vol. 17, no. 6, pp. 1779–1786, 2011.

[9] D. T. D. Childs *et al.*, "Trade-offs in the realization of electrically pumped vertical external cavity surface emitting lasers," in *Conference Digest - IEEE International*

Semiconductor Laser Conference, 2010, pp. 87–88.

[10] M. Guina, A. Rantamäki, and A. Härkönen, "Optically pumped VECSELs: Review of technology and progress," *Journal of Physics D: Applied Physics*, vol. 50, no. 38. Institute of Physics Publishing, p. 383001, 23-Aug-2017.

[11] J. G. Cederberg, A. R. Albrecht, M. Ghasemkhani, S. D. Melgaard, and M. Sheik-Bahae, "Growth and testing of vertical external cavity surface emitting lasers (VECSELs) for intracavity cooling of Yb:YLF," *J. Cryst. Growth*, vol. 393, pp. 28–31, May 2014.

[12] R. Sheikhi, Y. Huo, F. G. Shi, and C. C. Lee, "Low Temperature VECSEL-to-Diamond Heterogeneous Integration with Ag-In Spinodal Nanostructured Layer," *Scr. Mater.*, vol. 194, Mar. 2021.

[13] M. Kuznetsov, F. Hakimi, R. Sprague, and A. Mooradian, "High-power (>0.5-W CW) diode-pumped vertical-external-cavity surface-emitting semiconductor lasers with circular TEM 00 beams," *IEEE Photonics Technol. Lett.*, vol. 9, no. 8, pp. 1063–1065, Aug. 1997.

[14] Y. Huo, C. Y. Cho, K. F. Huang, Y. F. Chen, and C. C. Lee, "Exploring the DBR superlattice effect on the thermal performance of a VECSEL with the finite element method," *Opt. Lett.*, vol. 44, no. 2, p. 327, Jan. 2019.

[15] S. Weiß, E. Zakel, and H. Reichl, "Mounting of high power laser diodes on diamond heatsinks," *IEEE Trans. Components Packag. Manuf. Technol. Part A*, vol. 19, no. 1, pp. 46–53, Mar. 1996.

[16] B. G. Yacobi, S. Zemon, P. Norris, C. Jagannath, and P. Sheldon, "Stress variations due to microcracks in GaAs grown on Si," *Appl. Phys. Lett.*, vol. 51, no. 26, pp. 2236–2238,

1987.

[17] X. Liu *et al.*, "A study on the reliability of indium solder die bonding of high power semiconductor lasers," *J. Appl. Phys.*, vol. 100, no. 1, 2006.

[18] J.-W. Yoon, H.-S. Chun, J.-M. Koo, and S.-B. Jung, "AU-SN FLIP-CHIP SOLDER BUMP FOR MICROELECTRONIC AND OPTOELECTRONIC APPLICATIONS."

[19] G. S. Matijasevic, C. C. Lee, and C. Y. Wang, "AuSn alloy phase diagram and properties related to its use as a bonding medium," *Thin Solid Films*, vol. 223, no. 2, pp. 276–287, Feb. 1993.

[20] J. W. R. Teo, X. Q. Shi, S. Yuan, G. Y. Li, and Z. F. Wang, "Modified face-down bonding of ridge-waveguide lasers using hard solder," *IEEE Trans. Electron. Packag. Manuf.*, vol. 31, no. 2, pp. 159–167, Apr. 2008.

[21] W. Pittroff *et al.*, "Flip chip mounting of laser diodes with Au/Sn solder bumps: Bumping, self-alignment and laser behavior," in *Proceedings - Electronic Components and Technology Conference*, 1997, pp. 1235–1241.

[22] M. Hutter, F. Hohnke, H. Oppermann, M. Klein, and G. Engelmann, "Assembly and reliability of flip chip solder joints using miniaturized Au/Sn bumps," in *Proceedings - Electronic Components and Technology Conference*, 2004, vol. 1, pp. 49–57.

[23] R. W. Chuang and C. C. Lee, "Silver-indium joints produced at low temperature for high temperature devices," in *IEEE Transactions on Components and Packaging Technologies*, 2002, vol. 25, no. 3, pp. 453–458.

[24] Y. Y. Wu, W. P. Lin, and C. C. Lee, "A study of chemical reactions of silver and indium at 180 °c," *J. Mater. Sci. Mater. Electron.*, vol. 23, no. 12, pp. 2235–2244, Dec. 2012.

[25] Y. Huo and C. C. Lee, “The growth and stress vs. strain characterization of the silver solid solution phase with indium,” *J. Alloys Compd.*, vol. 661, pp. 372–379, Mar. 2016.

[26] Y. Huo, J. Wu, and C. C. Lee, “Study of Anti-Tarnishing Mechanism in Ag-In Binary System by Using Semi-Quantum-Mechanical Approach,” *J. Electrochem. Soc.*, vol. 164, no. 7, pp. C418–C427, 2017.

[27] Y. Y. Wu and C. C. Lee, “The strength of high-temperature ag-in joints produced between copper by fluxless low-temperature processes,” *J. Electron. Packag. Trans. ASME*, vol. 136, no. 1, 2014.

[28] H. Okamoto, “Ag-In (silver-indium),” *Journal of Phase Equilibria and Diffusion*, vol. 27, no. 5. pp. 536–537, Oct-2006.

Chapter 2

Experimental Procedures and Characterization Techniques

2.1 Material deposition techniques

Two techniques were used in this study to deposit multi-layer structures of materials on different substrates. First is Electron beam evaporation and the second is electroplating technique. Electron beam evaporation techniques is carried out in vacuum environment and provides excellent uniformity, cleanness, and control over film thickness. However, it can be very time consuming and expensive. Electroplating has higher deposition rates, is more economical, and can be performed in ambient environment. Here a brief review of both techniques is presented.

2.1.1 Electron beam evaporation

Electron beam (e-beam) evaporation is classified as a type of physical vapor deposition (PVD) technique. Metallic films are typically deposited by PVD processes as they are less expensive than chemical deposition techniques. E-beam evaporation can be used to deposit materials with high melting temperatures such as Ta, W, Ti, SiO_2, Al_2O_3, etc. Thus, it is possible to deposit materials that cannot be evaporated with standard resistive thermal evaporation. In addition, e-beam evaporation can provide higher deposition rates than possible with either sputtering or resistive evaporation.

This technique a tungsten filament is heated that results in electron emission. High voltage is used to accelerate electrons towards the crucible containing the material to be deposited. An applied electromagnetic field focuses the electrons into a uniform beam of energy that evaporates the material. The result is deposition of target materials onto the substrate. The entire process takes place inside of a vacuum chamber and multi-layer coatings can be deposited in one duty cycle [1].

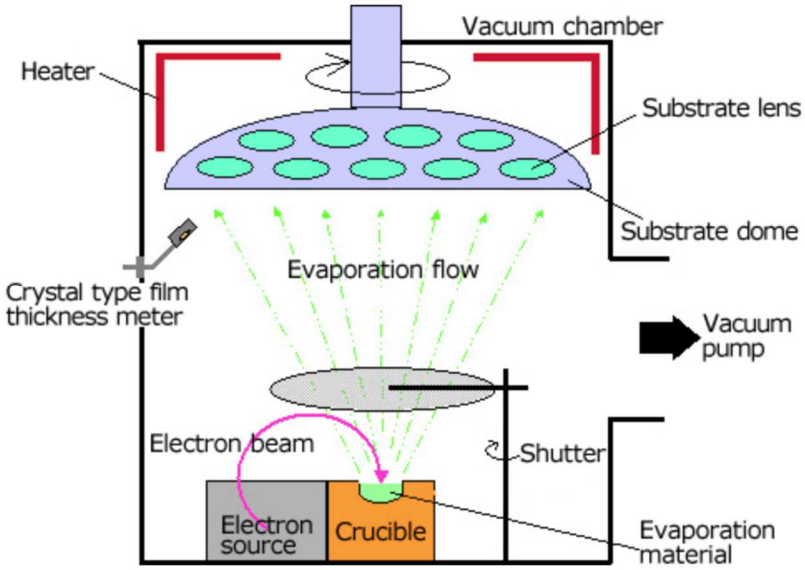

Figure 2.1 Schematic illustration of electron beam evaporation deposition technique, source: JEOL

As mentioned earlier, this vacuum deposition technique provides clean, uniform, and well thickness controlled metallic layers. The system used is equipped with a mechanical pump and a cryo- pump that can evacuate the chamber down to 2×10^{-8} torr range in two hours. This system allows deposition of up to four different materials in one vacuum cycle. The deposition thickness is measured in real-time using a quartz crystal.

However, during deposition, the substrates undergo high temperature, which may incur unwanted interdiffusion and reaction between deposited metal layers and also cause breakage when bonding CTE mismatched materials. In addition, it is difficult to produce metal layers thicker than 10μm using vacuum deposition methods. In our experiments, e-beam deposition is used to produce thin metallic films, serving as adhesion layers and multi-layer bonding layers.

Figure 2.1 Angstrom Engineering EvoVac Glovebox Evaporator

2.1.2 Electroplating

Electroplating is fundamentally a method of applying surface finishing. In general, surface electroplating can be performed for several reasons: (1) to improve appearance, (2) to slow or prevent corrosion and (3) to enhance strength and resistance to wear or (4) to deposit layers of material for bonding applications. The latter was the goal for utilizing electroplating in this study.

The term electroplating refers to the coating of an object with a thin layer of metal by use of electricity. The metals commonly used for coating are gold, silver, chromium, copper, nickel, tin, and zinc [1]. In general, any electrically conductive surface can be electroplated. The electroplating process uses an electric current to dissolve metal on the anode side and deposit it onto a substrate (the cathode).

The anode is the positively charged electrode in the circuit and is the metal that will form the plating. Cathode is the part that needs to be plated (substrate). This part acts as the negatively charged electrode in the circuit attracting the positive ions within the solution. The electrodepositing reaction takes place in an electrolytic solution. This solution contains one or more metal salts to facilitate the flow of electricity.

As the anode and cathode are placed in the solution and connected through wiring, the power supply provides a direct current (DC) to the anode. The current causes the metal to oxidize, allowing metal atoms to dissolve into the electrolyte solution as positive ions. The current also causes the metal ions to move to the negatively charged substrate and deposit onto the substrate as a thin layer of metal.

Many factors can impact the deposition rate and quality of the plated layer. The temperature and the chemical composition of the bath effect how effective the electroplating process is.

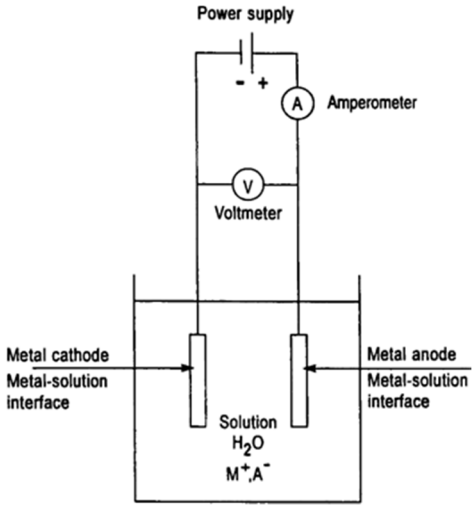

Figure 2.2 Schematics of an electrolytic cell for plating metal "M" from a solution of the metal salt "MA" [2].

The distance between anode and cathode can also affect how effectively the substrate is plated, so the placement of the anode relative to the cathode is of great importance. Both the voltage level and the electroplating time will affect the thickness and quality of the electroplated layer.

2.1 Materials characterization techniques

2.2.1 Scanning Electron Microscopy

Scanning Electron Microscopy (SEM) is one of the most commonly used experimental techniques that allows direct observation and characterization of micrometer and nanometer scale features in a wide range of materials. There is no particular requirement for preparing the SEM specimens as long as the sample surface is inherently conductive or

coated with thin layer of conductive materials. An SEM is comprised of: Electron gun, electromagnetic lenses, vacuum chamber and detectors. In the SEM, an electron beam is emitted from an electron gun, then narrowed to a size of approximately 0.4-5 nm in diameter through the use of one or two condenser lenses. The beam then passes through a pair of deflection coils in the electron column that deflect the beam in the x and y axes before interacting with the sample.

When The electron beam hits the sample, it will result in creation of an interaction volume and various signals are generated as a result, including auger electrons (AE), secondary electrons (SE), backscattered electrons (BSE), characteristic X-ray, continuum X-ray, secondary fluorescence and etc. (see figure 2.4). Signals generated can be collected using different detectors to form the final image. In the content of this dissertation, the mostly used signals are secondary and backscatter electrons. Secondary electrons are low energy electrons that are ejected from the valence or conduction bands of atoms in the sample through inelastic scattering from the incident electron beam. These electrons provide surface and morphological information. The back-scattered electrons are electrons from the beam that are reflected as a result of elastic scattering interactions with the atoms in the sample. The intensity of the back-scattered electron signal is dependent upon the atomic number so it can provide information about the distribution of different elements in a sample. In order to emit characteristic X-rays, the electron beam must interact with the sample and remove an inner shell electron, causing a higher-energy electron to fill the inner shell and release energy. The energy or wavelength of these X-rays is characteristic for each element and can be measured by Energy-dispersive X-Ray Spectroscopy (EDX) to identify

and measure the abundance and distribution of elements within the sample. In this study EDX has also been used along with SEM to provide a better understanding of distribution of elements in different regions within the sample [3].

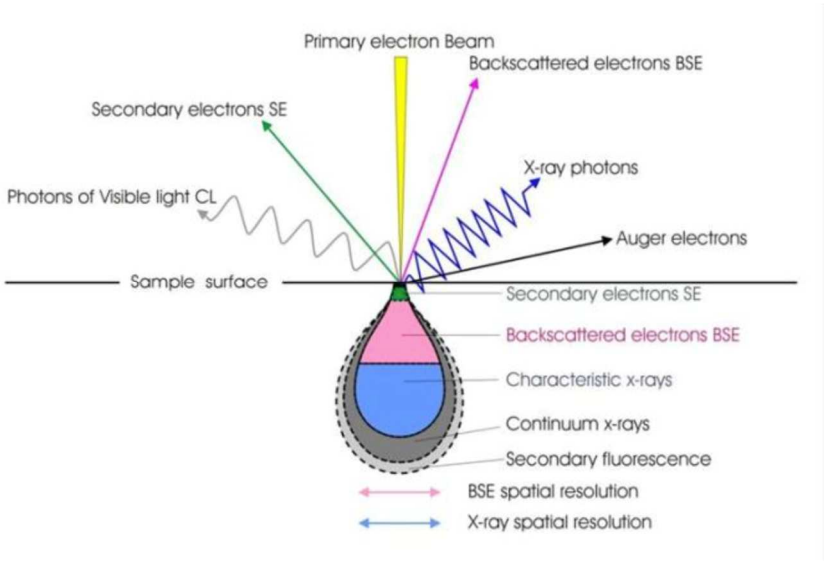

Figure 2.4 Schematic illustration of interaction volume of incident electron beam along with generated signals, source: University of Glasgow

2.2.2 Dual beam SEM-FIB

Focused Ion Beam (FIB) is being used in a variety of industries nowadays. Semiconductor industry, materials science and biology are among the areas in which FIB has been used significantly. FIB can be used for material removal, deposition and particle manipulation.

FIB is very helpful in creating clean cross-sections, by avoiding the smear effects that are typically induced when using conventional mechanical polishing. Also, in unique material systems that possess high hardness, FIB can be used as an alternate to mechanical polishing techniques.

FIB systems operate in an identical fashion to a SEM except, instead of a beam of electrons, FIB uses a finely focused beam of gallium ions that can be operated at low beam currents for imaging or high beam currents for site specific sputtering or milling.

The gallium (Ga+) primary ion beam hits the sample surface and sputters a small volume of material, which leaves the surface as either secondary ions or neutral atoms. The primary beam can also produce secondary electrons. As the primary beam rasters on the sample surface, the signal from the sputtered ions or secondary electrons is gathered to create an image. Using high ion beam currents, a great amount of material can be removed by sputtering, allowing accurate milling of the specimen down to a submicron scale.

In addition to primary ion beam sputtering, the sample can be flooded with an incoming gases species. These gases can interact with the primary gallium beam to provide selective gas assisted chemical etching, or selective deposition of conductive or insulating material, enabled by the primary ion beam decomposing the deposition gas [4].

It should be noted that FIB with high voltage can damage and etch the surfaces of various materials. Therefore, usually single frame or integrated frames of FIB images are captured instead of capturing live videos using FIB.

In this study all the SEM-FIB studies were carried out using a Tescan GAIA3 SEM-FIB instrument. Focus Ion Beam resolution of 2.5 nm with gallium at 1pA, can be attained using this instrument.

Figure 2.5 Tescan GAIA3 SEM-FIB instrument

In the context of this dissertation, FIB was used for two purposes. First was milling and to cut trenches into multi-layer structures and subsequent observation of the structure using SEM. Second application of FIB in this study was to prepare TEM specimens. The first application is essentially a portion of the TEM sample preparation process. In the following, an overview of the steps performed for TEM sample preparation using FIB is presented.

As mentioned, FIB systems usually have the capability to deposit materials on the sample surface. In the Tescan GAIA3 instrument used in this study, a gas injection source (GIS) probe can be used inside the chamber during SEM/FIB operation, so that FIB-assisted chemical vapor deposition (CVD) can be implemented to deposit Pt onto the sample surface. This deposition step is comprised of three steps: (1) Adsorption of the organic-metallic precursor molecules on the sample surface, (2) Focus ion beam induced dissociation of the gas molecules and (3) Deposition on the sample surface and removal of organic ligands. As shown in figure 2.6 (left), a strip of Pt layer can be deposited by FIB deposition. The deposition of this layer is the first step in TEM sample preparation process. The Pt protective layer will mitigate damage to the sample being prepared throughout the process.

After deposition of the protective layer, trenches are cut on both sides of the Pt layer and then a cut is made beneath the sample to loosen it from the initial specimen surface. At this time the TEM sample can be welded to the Omniprobe.

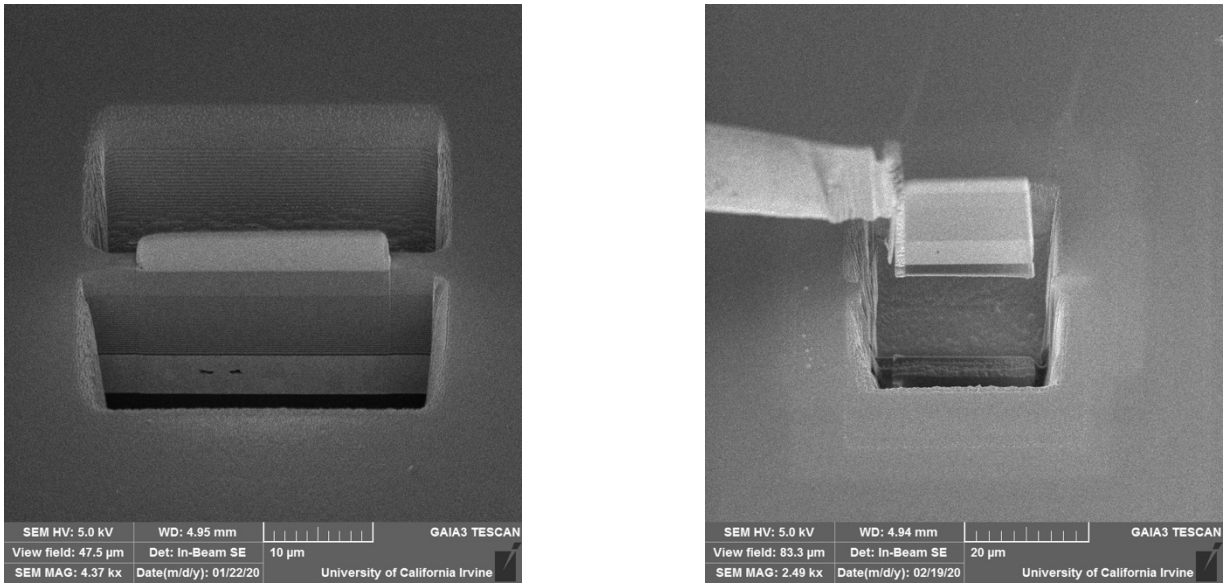

Figure 2.6 SEM image (at 55° tilt) of (left) Pt layer deposited, and trenches cut on both sides of specimen (right) Attachment and lift off of specimen

By using the combination of FIB deposition, FIB cutting and Omniprobe, a start-of-art method to prepare transmission electron microscopy (TEM) samples can be achieved. As shown in figure 2.7, after a number of sequences of FIB deposition and FIB cutting, after picking up, the sample can be attached to the copper TEM grid where further thinning using FIB is carried out. In all steps, significant caution is exercised to ensure minimal damage to the TEM sample.

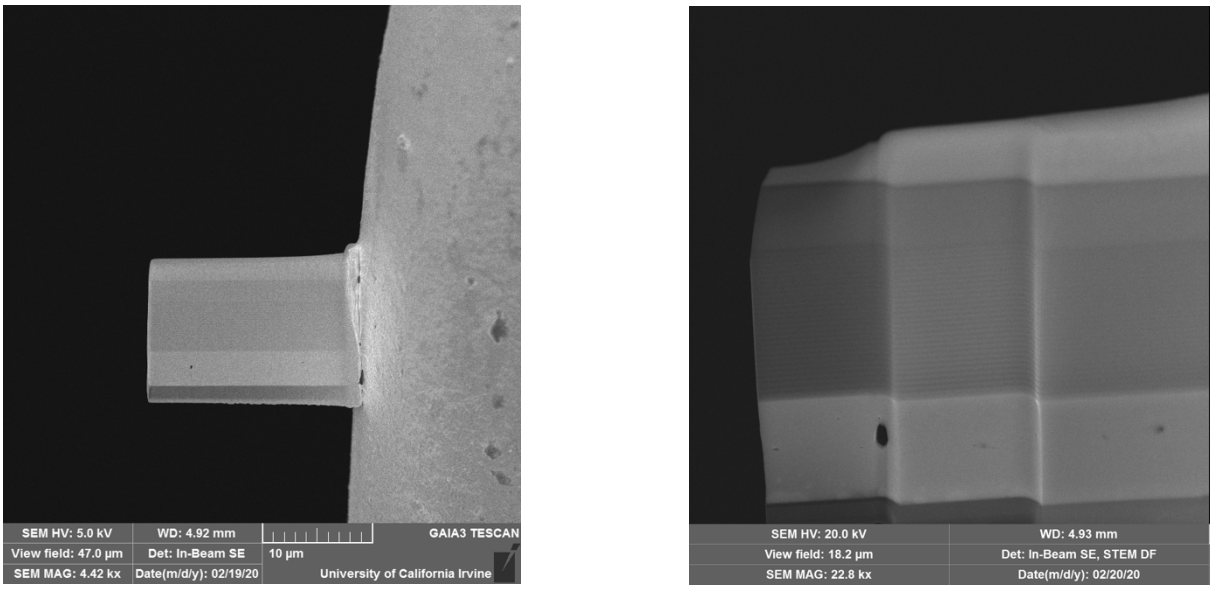

Figure 2.7 SEM image of (left) specimen attached to the TEM grid (right) Specimen after thinning process

2.2.3 Transmission Electron Microscope

In transmission electron microscopy (TEM), an accelerated beam of electrons generated from a field emission gun (FEG) is condensed using condenser electromagnetic lenses and apertures down a column where it eventually transmits a very thin specimen. All of electromagnetic lenses that are located before the specimen demagnify the electron beam to acquire a parallel beam. Then the transmitted electrons are projected onto a fluorescence screen (ZnS) or a charged couple device (CCD) camera to acquire the resulting image after passing through a series of electromagnetic lenses and apertures. These electromagnetic lenses (the imaging system) are all magnifying the electron beam to increase the resolution of the image. The resulting interaction of the electrons with the specimen can be utilized to image and characterize many aspects of the specimen including mass contrast, phase

contrast, defects, interfaces, density variations, atomic composition, crystal structure and orientation, and lattice parameter. Figure 2.8 illustrates the schematic configuration of a TEM.

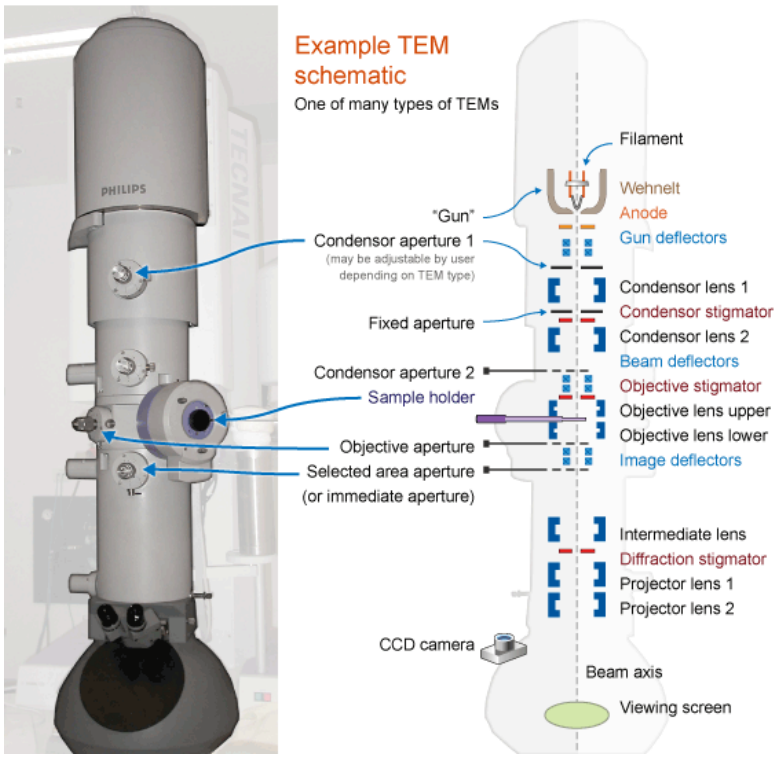

Figure 2.8 schematic illustration of components within the TEM chamber, source: MYScope

Nowadays, TEM related techniques are very mature and have various modes such as bright field (BF), dark field (DF), selected area diffraction (SAD), convergent-beam electron diffraction (CBED), electron energy-loss spectrometry (EELS), high-resolution TEM (HRTEM), high-angle annular dark-field (HAADF) imaging, and more [5].

In the context of this research, the HAADF-STEM mode in JEM-ARM300F Grand ARM TEM was used. HAADF stands for high-angle annular dark field imaging. Annular dark-field imaging is a method of mapping samples in a scanning transmission electron

microscope (STEM). These images are formed by collecting scattered electrons with an annular dark-field detector.

High-angle annular dark-field imaging (HAADF) is a STEM technique that produces an annular dark field image formed by very high angle, incoherently scattered electrons. This scattering is a result of interaction of incoming electron beam and nucleus of atoms. This technique is highly sensitive to variations in the atomic number of atoms in the sample.

For elements with a higher atomic number more electrons are scattered at higher angles due to greater electrostatic interactions between the nucleus and electron beam. Because of this, the HAADF detector senses a greater signal from higher atomic number atoms, depicting them brighter in the final image.

This compositional dependence makes HAADF a useful way to easily identify small areas of an element with a high atomic number in a matrix of material with a lower atomic number. This characteristic of HAADF STEM was utilized extensively in the current study. Image resolution in HAADF STEM is very high and predominately determined by the size of the electron probe, which in turn depends on the ability to correct the aberrations of the objective lens, in particular the spherical aberration [5].

The JEOL Grand ARM S/TEM used in this study is a double-corrected STEM that offers 0.63 nm spatial resolution at 300 kV. The instrument is Equipped with a cold field emission gun and configured with a wide gap pole piece (>6 mm), the Grand ARM is an ideal instrument for a variety of in situ experiments to study the structure, properties, and dynamic behavior of nanostructured materials under applied fields, stress, and reactive environments.

The Grand ARM uses a unique hybrid high-angle annular dark-field (HAADF) STEM detector. In addition, the Grand ARM is equipped with EDS for chemical analysis.

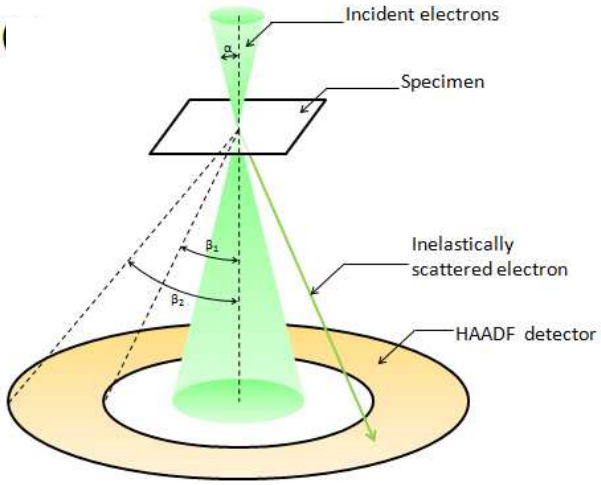

Figure 2.9 Configuration of electron beam distribution used for HAADF imaging, source: JEOL

2.2.4 Xray photoelectron spectroscopy

X-ray photoelectron spectroscopy (XPS) is a quantitative technique for quantifying the elemental composition of the surface of a material, and it also determines the binding states of the elements. XPS normally probes to a depth of 10 nm, thus it is very sensitive to compositional fluctuations in the surface. XPS also needs an ultra-high vacuum chamber.

In XPS, the sample is irradiated with a beam of x-rays and the kinetic energy of the emitted electrons also known as photoelectrons is analyzed. The emitted photoelectron is the product of complete transfer of the x-ray energy to a core level electron. This is described mathematically in Eq. (2.1). This equation states that the energy of the x-ray (hv) is equal to the binding energy (BE) of the electron, plus the kinetic energy (KE) of the electron that is emitted, plus the spectrometer work function (Φ_{spec}), a constant value.

$$h\nu = BE + KE + \Phi_{spec} \quad (2.1)$$

Hence, binding energy of an electron can be determined, by knowing the terms hν and Φ_{spec} and measuring KE through the XPS experiment. Any electron with a binding energy less than the x-ray source energy should be emitted from the sample and observed with the XPS technique. The binding energy of an electron is a characteristic material property.

The loss of the XPS core electron results in a core hole. This excited ionized state will relax by filling the hole with an electron from a valence orbital. In this process, energy is released in one of two processes: the emission of an Auger electron or x-ray fluorescence. Auger electrons generated by the process can be detected and are often used in XPS for qualitative analysis [6].

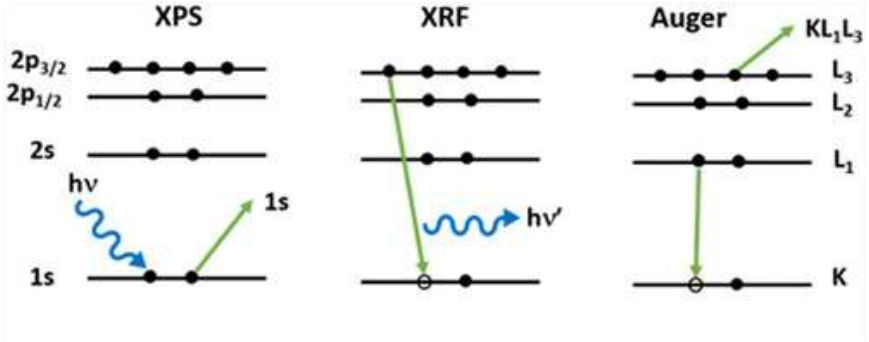

Figure 2.10 Mechanisms responsible for signal generation in XPS, XRF and AES [6]

In the current study, AXIS Supra by Kratos Analytical was used for the XPS study. This instrument uses an Al monochromatic X-ray source and is capable of high-resolution scanning field emission Auger electron spectroscopy and microscopy (AES, SAM), ultraviolet photoelectron spectroscopy (UPS), ion scattering spectroscopy (ISS) and reflection electron energy loss spectroscopy (REELS).

In this dissertation, the X-ray photoelectron spectroscopy (XPS) studies were performed with a monochromatized Al Kα radiation source (hν=1486.6 eV). All data were collected with an analyzer pass energy of 20 eV with the spot size of 300 μm × 700 μm. The scanning energy resolution was 0.05 eV with a dwell time of 100 ms. The XPS survey and region spectra reported were measured with an average of 7 and 11 scans, respectively.

Figure 2.11 AXIS Supra by Kratos Analytical

2.2.5 Die shear test

Die shear tests are used as a method to determine the adhesion of semiconductor die or microelectronic devices to different substrates. Most important parameters affecting the test results are test speed and tool height. The principle behind die shear bond testing is to apply a wedge-shaped shear tool perpendicular to the materials top surface and parallel to the longest edge of the die. Self-aligning shear tools ensure the die is kept parallel and thus the load is spread as evenly as possible during the shearing process. Shear tools should be at least as wide as the object being tested. The test object is then moved against the shear tool until the bond interface or

semiconductor die fails, or a pre-defined amount of force is reached. In this study, die shear tests were carried out using a STR-1000, Rhesca bonding tester machine. The tip velocity was set at 21 mm/min and the fly height from the substrate was 50 µm.

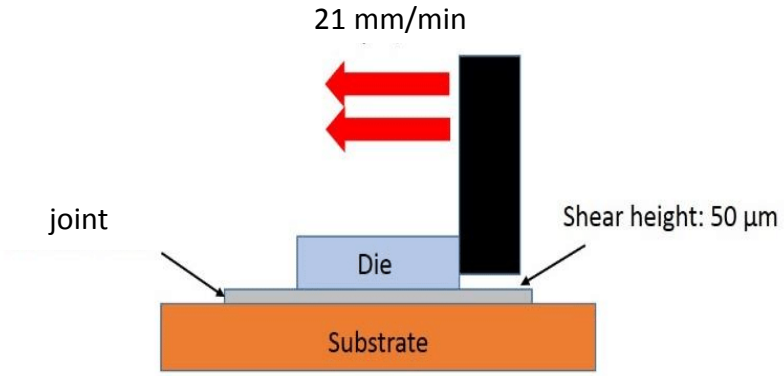

Figure 2.12 Schematic representation of die shear test and the parameters used in this study

References

[1] K. S. Sree Harsha, *Principles of Vapor Deposition of Thin Films*. Elsevier Ltd, 2006.

[2] M. Schlesinger, "Electroplating," in *Kirk-Othmer Encyclopedia of Chemical Technology*, Hoboken, NJ, USA: John Wiley & Sons, Inc., 2004.

[3] J. I. Goldstein, D. E. Newbury, J. R. Michael, N. W. M. Ritchie, J. H. J. Scott, and D. C. Joy, *Scanning electron microscopy and x-ray microanalysis*. Springer New York, 2017.

[4] C. A. Volkert and A. M. Minor, "Focused ion beam microscopy and micromachining," *MRS Bulletin*, vol. 32, no. 5. Materials Research Society, pp. 389–395, 2007.

[5] D. B. Williams and C. B. Carter, *Transmission electron microscopy: A textbook for materials science*. Springer US, 2009.

[6] F. A. Stevie and C. L. Donley, "Introduction to x-ray photoelectron spectroscopy," *J. Vac. Sci. Technol. A*, vol. 38, no. 6, p. 063204, Dec. 2020.

Chapter 3

Low Temperature VECSEL-to-Diamond Heterogeneous Integration with Ag-In Spinodal Nanostructured Layer

3.1 Introduction

Chapters 3 and 4 of this the VECSEL was discussed. Here, before further discussing the VECSEL dissertation are focused on packaging of VECSELs using Ag-In bonding technology. In chapter 1, an overview of package design features necessary for effective heat dissipation away from to diamond integration, a brief overview of the whole package structure is presented.

The overall package is shown in figure 3.1. The package is built by first bonding the VECSEL to the CVD diamond using Ag-In bonding system and subsequently bonding the backside of the CVD diamond to the copper heat sink forming the second join. Chapter 3 is a detailed study on the first joint and chapter 4 provides a deep dive into the second joint.

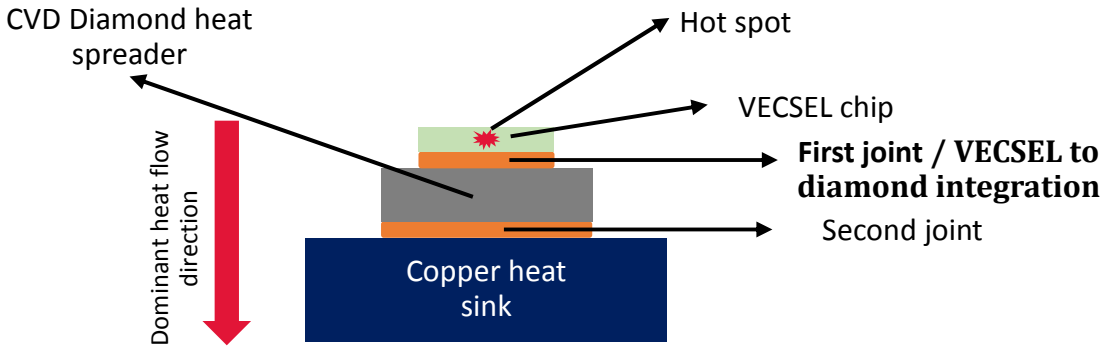

Figure 3.1 Schematic illustration of the VECSEL package

Details of the VECSEL chip epitaxial layer and the flip-chip bonding of VECSEL was discussed in detail in chapter 1. In the flip-chip configuration, a reversely-grown epitaxial chip is bonded onto a diamond heat spreader, followed by the complete removal of the epitaxial substrate [1]. After the substrate removal, the remained active epitaxial membrane (<10 μm) is extremely fragile. Therefore, the heterogeneous bonding joint is essential to the performance and long-term reliability of the VECSEL device, whose thickness is a crucial parameter to consider in the VECSEL design. Specifically, a thinner joint is highly preferred for enhancing the heat transportation, whereas a thicker joint facilitates the management of thermomechanical stress induced by the coefficient of thermal expansion (CTE) mismatch between the compound semiconductor and diamond [2]. A low temperature bonding process would mitigate the thermomechanical stress level to allow a thinner joint without causing further issues, such as micro-cracks generation [3] or stress induced peak-shift [4]. Thus, a low temperature bonding process is inherently beneficial to the VECSEL-to-diamond heterogeneous integration, whereby pushing the thermal dissipation limits with an ultra-thin bonding joint.

Traditionally, indium has been the most commonly used bonding material for laser diode packaging, but it severely suffers from the creep and thermal fatigue issues due to the low yield strength [5]. Rather than indium, commercially available VECSELs have adopted Au-Sn eutectic as the bonding medium [6], owing to its high strength and high thermal stability. However, Au-Sn eutectic is still not an ideal method, mainly due to its high bonding temperature (320°C) and associated high thermo-mechanical stress level. Other gold-based bonding methods, such as Au-Au [7] and Au-In [8], have also been investigated to reduce the

bonding temperature for the VECSEL applications, albeit with high raw materials cost. In this chapter, we propose to utilize silver-indium (Ag-In) transient liquid phase (TLP) bonding method for the low temperature VECSEL-to-diamond heterogeneous integration. It is demonstrated that the Ag-In bonding system can achieve a mechanically strong [9] and thermally stable joint [10], with the superior anti-tarnishing [11] and anti-electrochemical-migration properties[12]. Aiming at VECSEL applications, we have successfully overcome previous technical difficulties and made a substantial

progress in scaling down the critical dimension of the Ag-In joint. To the best of the authors knowledge, this is the first reported work of functional VECSEL-to-diamond heterogeneous integration with an Ag-In bonding layer, in which a unique nanostructure, originated from spinodal decomposition, was discovered for the first time.

3.2 Flip-chip bonding process of VECSEL to diamond

The VECSEL gain chips (2mm x 2mm) were diced from molecular beam epitaxial (MBE) grown GaAs wafer. Prior to dicing, Cr (30 nm)/Au (50 nm)/Ag (1000 nm) metallization layers were sequentially deposited on the epitaxial side of GaAs wafer with E-beam evaporation under high vacuum ($\sim 10^{-7}$ torr), followed with a vacuum annealing process to improve adhesion. Commercially available chemical vapor deposition (CVD) grown polycrystalline diamonds (3mm x 3mm) were cleaned with acetone, isopropanol and Ar plasma. Then the diamonds were divided into two study Groups. Group A diamonds were E-beam evaporated with Cr (30 nm)/Au (50 nm)/Ag (1000 nm)/In (1200 nm)/Ag (20 nm) within one vacuum cycle, whereas group B diamonds with Cr (30 nm)/Au (50 nm)/Ag (1000

nm) were annealed at 300°C for one hour, before further depositing the indium and capping Ag layers. Dividing the diamond into two study groups was carried out in order to study the effect of Ag grain size on diffusion of In into Ag and subsequent void formation. A more detailed discussion on the reasoning for choosing these two study groups will provided in the subsequent discussion section. Within a vacuum furnace (~60 mtorr), the VECSEL gain chips were, respectively, bonded to the metallized sides of group A and B diamonds under 1.37 MPa static pressure. During bonding, the samples in both groups dwelled at 190°C for 10 mins, and then slowly cooled down to room temperature in one hour. Followed by a mechanical lapping and a selective chemical wet-etching process ($NH_4OH:H_2O_2:H_2O$) [7.5ml : 15ml : 80ml], The initial mechanical lapping brings the VECSEL thickness down to approximately 150 μm and the final wet etch step removes the remainder of the GaAs substrate. At this point the thickness of remaining die is approximately 12 μm. Intermediate annealing steps throughout the wet etching were used to release the internal stresses within the thin and fragile GaAs die. It is necessary that formation of cracks within the die are avoided throughout the bonding and post-bond substrate removal process. Eventually, the 600 μm thick GaAs substrate was completely removed, leaving the epitaxial layers fully intact on the diamond.

Figure 3.2 shows an overview of all these steps. Scanning electron microscopy coupled with focus ion beam (SEM-FIB) dual beam system was used to trench a cross-section of the VECSEL-to-diamond interfaces, followed by a FIB lift-out process for the transmission electron microscopy (TEM) sample preparation. To investigate the nanostructures within the epitaxial layer and the Ag-In bonding layer, this study utilized an atomic resolution high-

angle annular dark-field scanning transmission electron microscopy (HAADF-STEM), equipped with double spherical aberration correctors. The chemical compositional information was gathered with the STEM coupled energy dispersive X-Ray spectroscopy (EDX) at high spatial resolution.

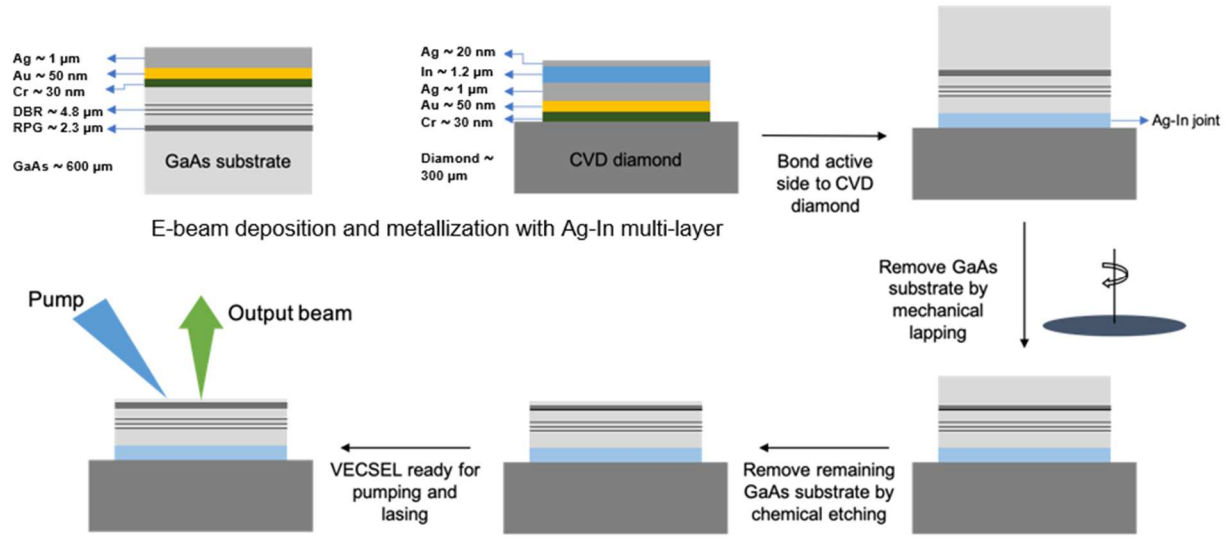

Figure 3.2 The schematic representation of major steps in the flip-chip bonding of VECSEL to CVD diamond heat spreader using Ag-In TLP bonding method:
1. Metallization of the GaAs-based VECSEL epitaxial wafer with E-beam deposition process.
2. Metallization of CVD diamond heat spreader with E-beam deposition process.
3. Heterogenous integration process between the GaAs-based VECSEL epitaxial chip to the CVD diamond heat spreader with the Ag-In transient liquid phase bonding method.
4. Partial removal of the GaAs substrate with mechanical lapping method.
5. Complete removal of the GaAs substrate with chemical wet-etching process ($NH_4OH:H_2O_2:H_2O$).
6. The following optical and microscopic characterizations of the VECSEL-to-Diamond module in the flip-chip configuration

3.2.1 Deposition of multi-layer bonding structure on GaAs and diamond

Figure 3.3 shows the schematic representation of the deposited the structure on VECSEL chip and the diamond. These multi-layer structures were deposited using electron beam evaporation technique. Designed Ag-In multi-layer structure results in a joint of Ag 70 at% and In 30 at% composition. Cr is a carbide forming element that exhibits good adhesion to diamond. The top Ag layer (20nm) acts as protective layer against oxidation of In. In is prone to oxidation and forms several nanometers-thick In_2O_3 layer even at room temperature.[13] Indium oxide compound can potentially degrade the mechanical and thermal properties of the joint, thus protective Ag layer is necessary in order to obtain the oxide free microstructure. After the deposition stage, SEM-FIB was used to cut trenches perpendicular to the interface of deposited layers to evaluate the quality and thickness of the applied layers (see figure 3.4). An observation that was made after the deposition of In, was the very high

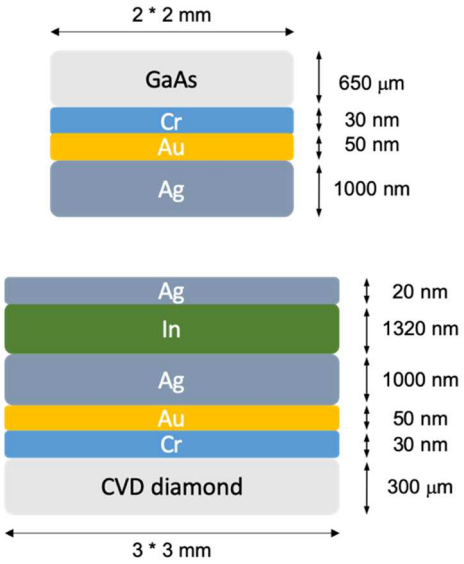

Figure 3.3 Schematic representation of the deposited layers on

value of surface roughness and hillock type morphology of the In film, see figure 3.5. Effects of this morphology on the joint layer will be further discussed in the following sections.

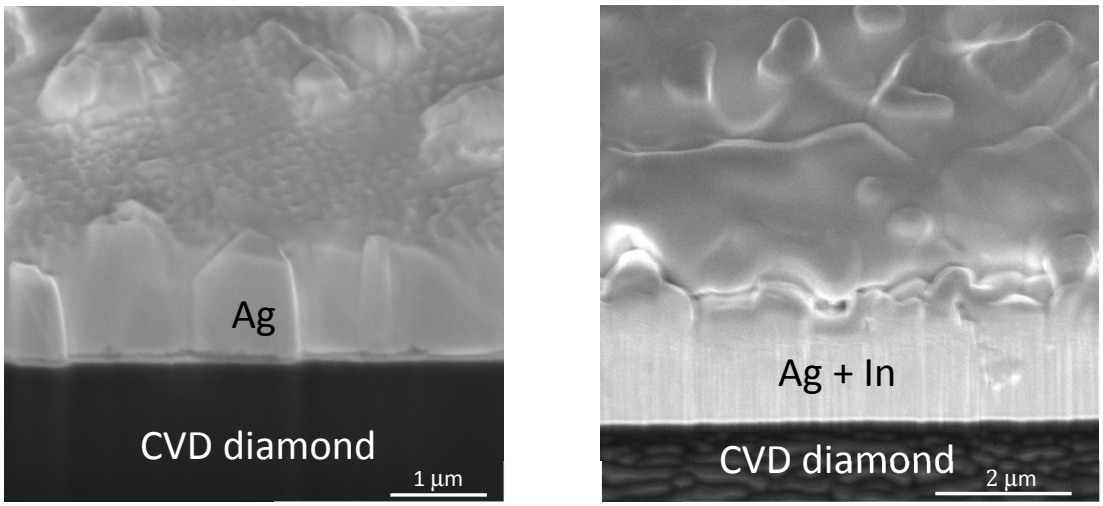

Figure3.4 SEM image of deposited Ag and Ag+In layer on CVD diamond, cross sections prepared by FIB

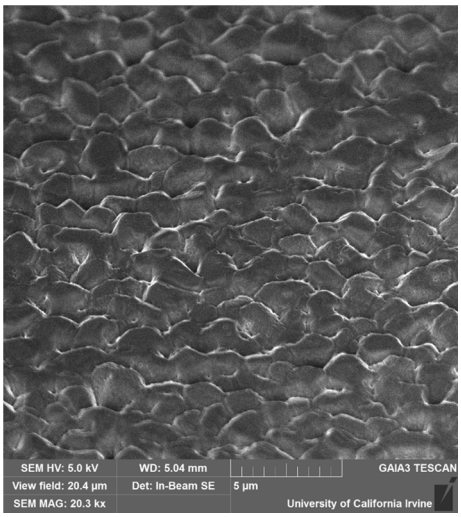

Figure3.5 The SEM image of the hillock-type morphology on the surface of E-beam evaporated indium, which is partially responsible for the first-type interfacial voids in the SCA

3.3 Microstructure of the Ag-In joint

Figure 3.6 shows the representative bonding layer of the VECSEL-to-diamond heterogeneous interfaces for the group A and B diamonds. Clearly, the sample with group B diamond (SGB) has a better bonding quality than the sample with group A diamond (SGA). Specifically, two types of interfacial voids were found in SGA. The first-type interfacial voids, with either a triangular or a horizontal elongated shape, were distributed along the original bonding interface between VECSEL and diamond. This was originated from the undersupply of molten phase issue in the Ag-In TLP bonding [18]. In addition, E-beam evaporated indium formed a hillock-type surface morphology when depositing on the top of Ag layer, which further exaggerated the formation of first-type voids during bonding, see figure6. The second-type interfacial voids (scallop-type) were located at the metallization site on diamond, which were induced by the indium over-diffusion through the Ag grain boundaries and the weak interfacial strength of as-deposited E-beam layer. In SGB, by using the prior-to-bond annealing process, the grain boundary density in Ag layer has been reduced, resulting in preserving enough molten phase during Ag-In TLP process. It has also improved the interfacial strength between the metallization layers and diamond.

In a previous study, our research group exhibited that undersupply of molten In during bonding using Ag-In system can result in voiding at the initial bonding interface. In the early stages of interdiffusion in the Ag-In system, the diffusion of In into Ag is dominated by grain boundary diffusion. According to prior studies, at low temperatures, In can be consumed by Ag, forming $AgIn_2$, resulting in lack of molten phase (In) at the bonding temperature. Controlling the Ag grain size has shown to be an effective mean to mitigate the prior-to-bond

consumption of In by Ag. The concept of manipulating the Ag grain size for the purpose of slowing down the diffusion of In into Ag will be discussed in more detail in the context of second joint/chapter 4.

Consequently, the two types of interfacial voids in SGA have been simultaneously eliminated in SGB, thereby achieving a nearly perfect Ag-In ultra-thin joint (~3μm) for the VECSEL-to-diamond heterogeneous integration.

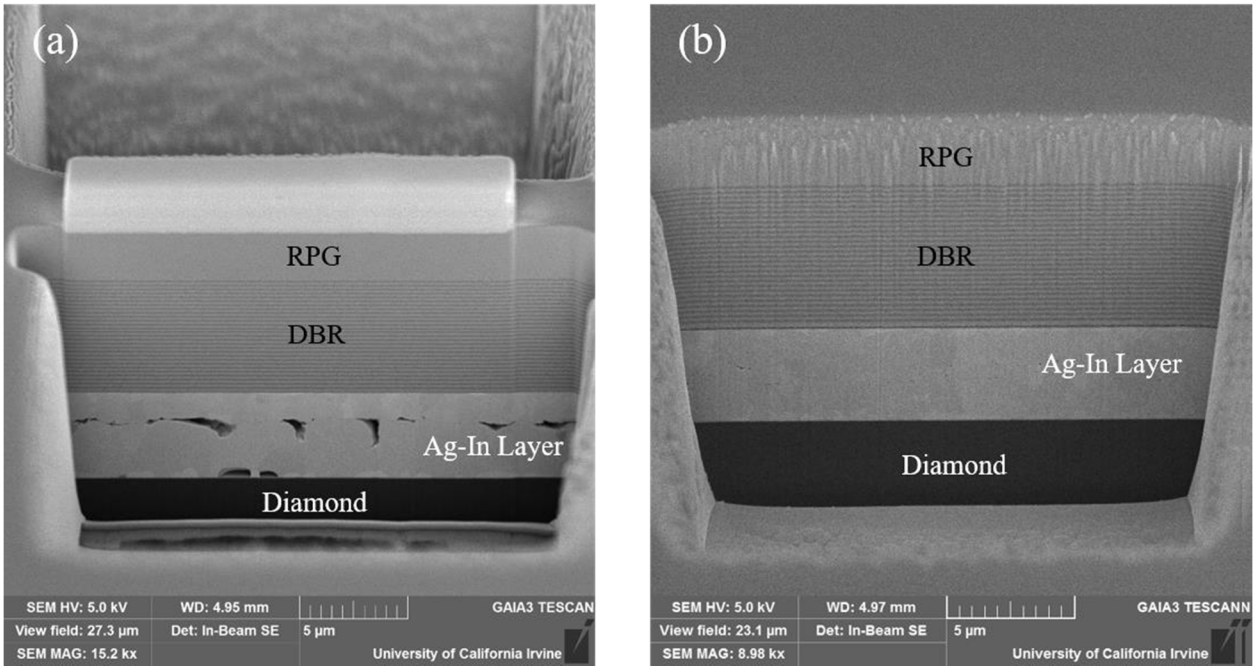

Figure 3.6 Cross-sectional SEM images of VECSEL-to-diamond heterogeneous interfaces: (a) SGA, and (b) SGB.

3.4 Effects of bonding on the VECSEL epitaxial layer

As mentioned in the introduction, it is critical for the bonding process to be carried out at lowest temperature possible. A low temperature bonding process would mitigate the thermo-mechanical stress level to allow a thinner joint without causing further issues, such as micro-cracks generation [3] or stress induced peak-shift [4]. Thus, a low temperature

bonding process is inherently beneficial to the VECSEL-to-diamond heterogeneous integration, whereby pushing the thermal dissipation limits with an ultra-thin bonding joint. The post-bonding quality of the VECSEL epitaxial layer is demonstrated in figure 3.7, illuminating its resonant periodic gain (RPG) structure and distributed Bragg reflector (DBR) with high resolution STEM. Within the RPG structure, the InGaAs multiple quantum wells (MQWs) were periodically grown at the antinode positions of the optical standing wave, equally spaced by GaAs stress compensation layers. The DBR consists of 28.5 pairs of GaAs/AlAs quarter-wavelength superlattice structure, whose post-bonding epitaxial interfaces have remained sharp to obtain a high reflectivity (R > 99.95%) value for the optimal lasing condition. Most importantly, a well-defined boundary of the QW is crucial to the quantum efficiency, lasing spectrum and output lasing power of a VECSEL.

Due to the intrinsic advantages of the low temperature Ag-In TLP bonding process, the thermal-induced diffusion and its residue thermo-mechanical stress level have been minimized in the active epitaxial layers. Therefore, the InGaAs/GaAs epitaxial interfaces of QWs showed the atomic abrupt transition in figure 3.7(d), where no traces of extensive thermal diffusion or residue stress induced dislocation structures were found.

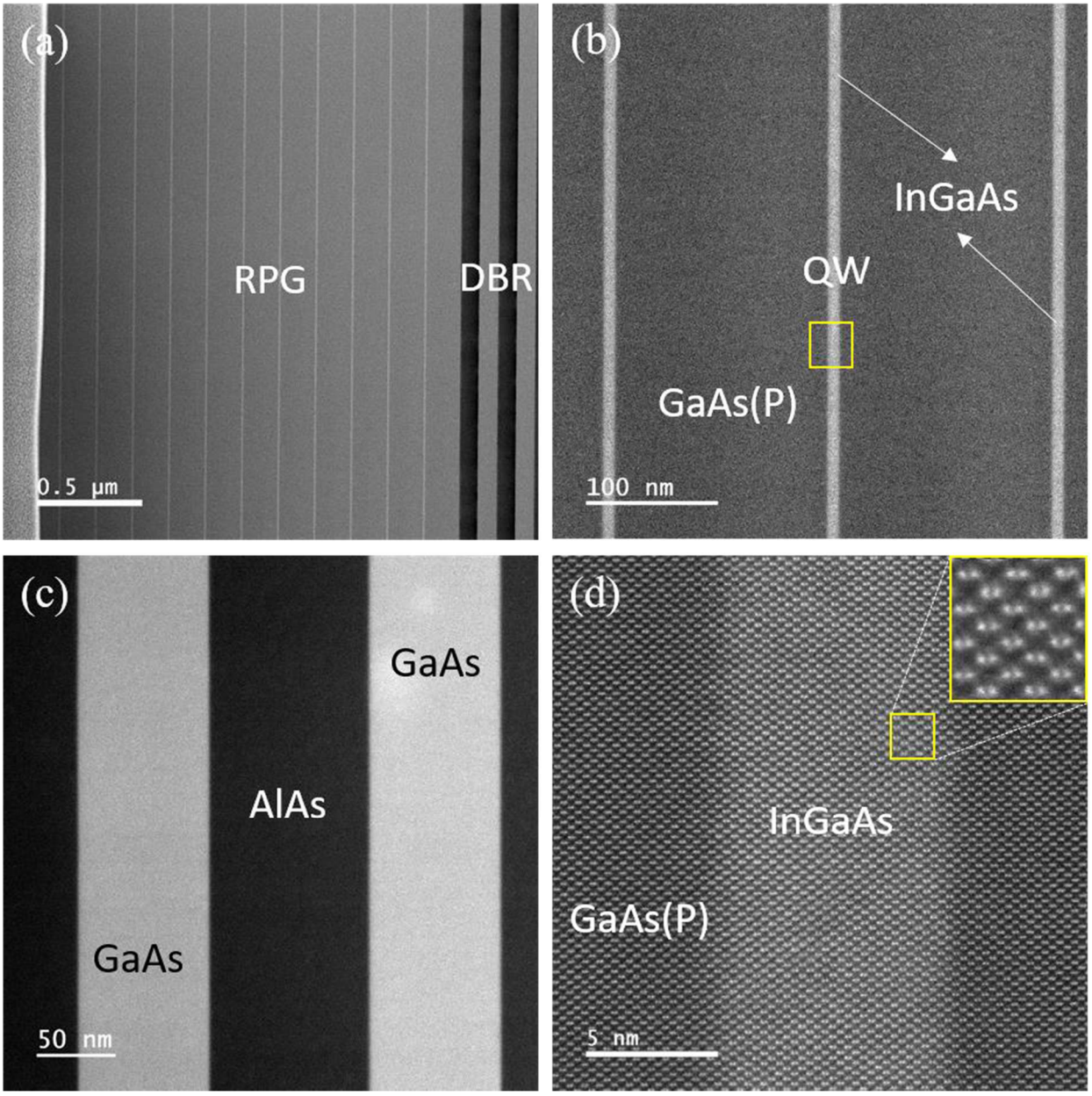

Figure 3.7 High-resolution HAADF-STEM images of a post-bonding VECSEL epitaxial layer: (a) a global view, (b) the multiple QWs in RPG, (c) the DBR superlattice, and (d) a single QW viewing from [1 1 0] zone axis at atomic resolution.

3.5 Nanostructure of the Ag-In joint

Intriguingly, as further examining the Ag-In bonding layer with HAADF-STEM in Figure 3.8, a nano-scale structural feature was discovered in both SGA and SGB, with a characteristic scale ranging from 30 nm to 50 nm, showing a two-phase separation morphology with Z-contrast. According to the STEM-EDX elemental mapping results in Figure 3.8, the embedded phase with bright contrast could be identified as Ag_3In α' phase (Ag~75.0 at.%, cP4, $Pm\bar{3}m$), whereas the matrix phase with dark contrast could be characterized as Ag_2In γ phase (Ag~66.7 at.%, cP52, P43m) [9]. Recalled that the VECSEL-to-diamond coupons were slowly cooled down after bonding, without a high quenching rate, the observed nanostructure was not likely to form through the nucleation-growth mechanism, but indeed existed in the Ag-In bonding layer. Nevertheless, the originality of such two-phase nanostructure can be rationalized from spinodal decomposition[14].

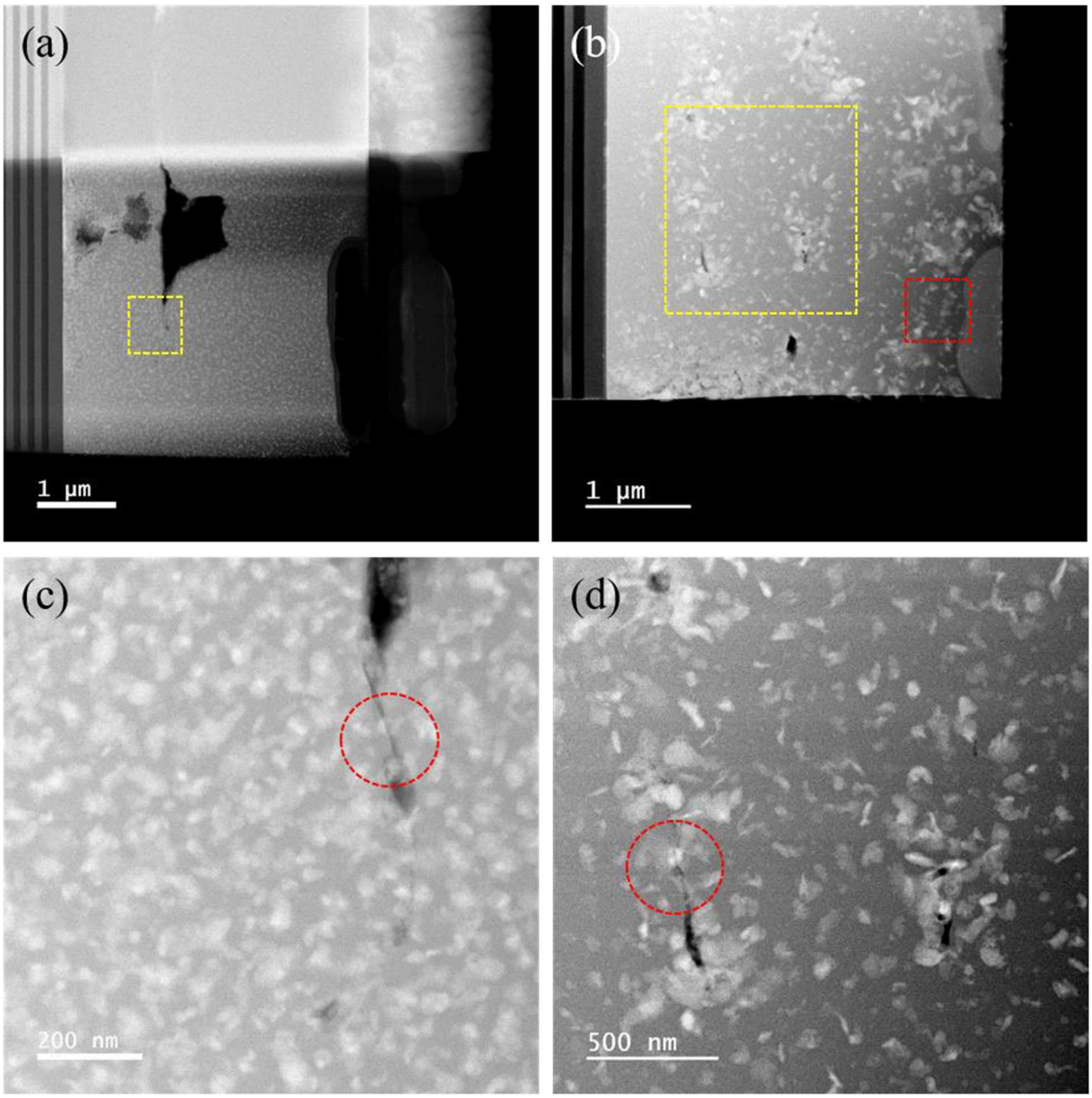

Figure 3.8 HAADF-STEM images of the Ag-In spinodal nanostructured layer: (a) a low-magnification view of SGA, (b) of SGB, (c) a high-magnification view at the enclosed box in (a), and (d) at the enclosed box with yellow-dash-line in (b).

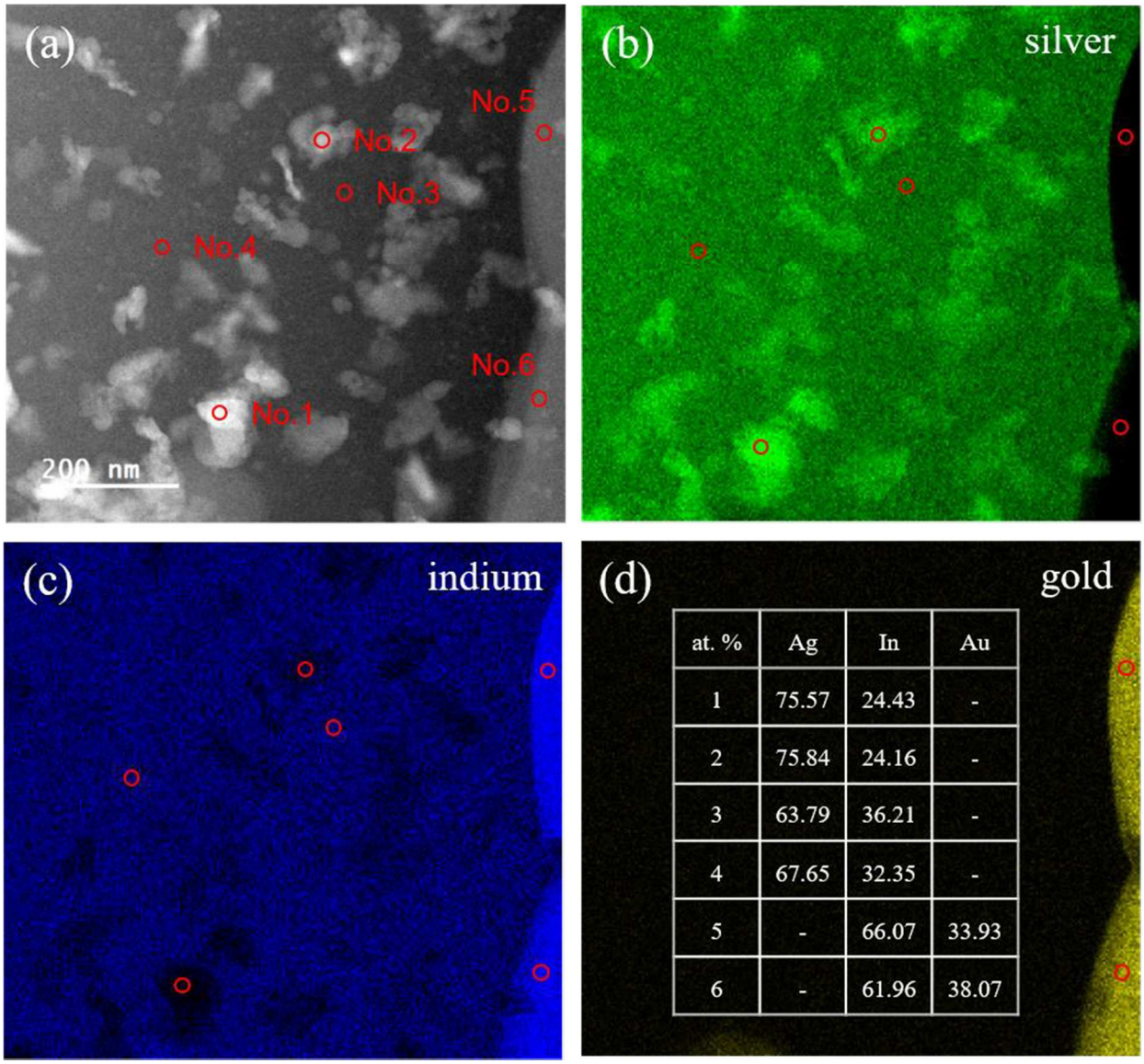

at. %	Ag	In	Au
1	75.57	24.43	-
2	75.84	24.16	-
3	63.79	36.21	-
4	67.65	32.35	-
5	-	66.07	33.93
6	-	61.96	38.07

Figure 3.9 (a) HAADF-STEM image at the enclosed box with red-dash-line in Figure 3.8 (b), (b) the high-resolution EDX mapping of Ag element, (c) of In element, (d) of Au element with quantitative data at the marked points.

Another observation in regard to the phases observed with STEM is the formation of $AuIn_2$ intermetallic compound at areas close to the Cr/Au interface. Ag and Au are completely miscible in the whole span of their composition. Thus prior to bond annealing and the bonding step results in dissolution of Au metallization layer into the Ag and formation of

$AuIn_2$. It should be noted that after the bonding the Cr adhesion layer remains completely intact. The remained Cr adhesion layer is depicted in figure.

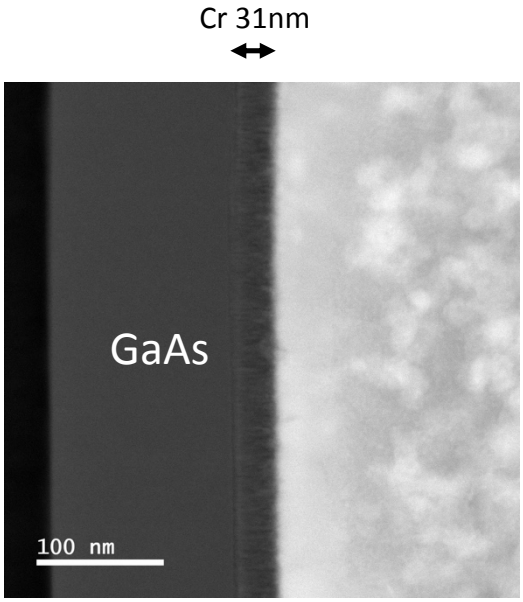

Figure 3.10 GaAs interface after the bonding process

3.6 Spinodal decomposition

During spinodal decomposition, one phase separates spontaneously into two phases because small compositional fluctuations can decrease the free energy of the system. As a result, phase transition occurs immediately and without any delay, contrary to when there is a nucleation barrier.

Consider a phase diagram with a miscibility gap, as shown in Figure 3.11 (a). If an alloy with composition X_0 is solution treated at a high temperature T_1 and then quenched to a lower temperature T_2 the composition will initially be the same everywhere and its free energy will be G_0 on the G curve in figure 3.11 (b). However, the alloy will be instantly unstable because small fluctuations in composition that produce A-rich and B-rich regions will cause the total

free energy to decrease. Hence up-hill diffusion takes place as shown in Figure 3.12 until the equilibrium compositions X_1 and X_2 are reached.

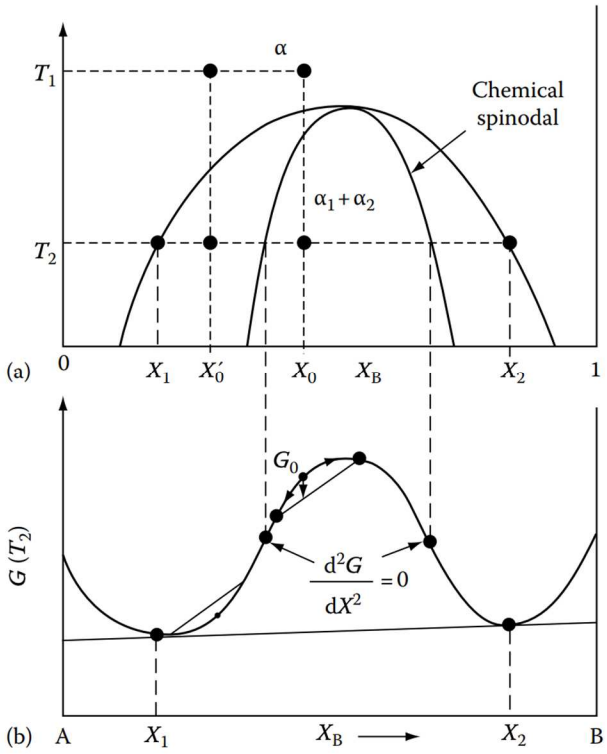

Figure 3.11 Alloys between spinodal points are unstable and can decompose into two phases without overcoming an activation energy barrier. Alloys between miscibility gap and the spinodal are metastable and can decompose only after nucleation of the other phase [15].

This process can occur for any composition where the free energy curve has a negative curvature, in other words whenever:

$$\frac{d^2G}{dX^2} < 0 \qquad (3.1)$$

Thus, the alloy must lie between the two points of infection on the free energy curve. The locus of these points on the phase diagram is known as the chemical spinodal. If the alloy lies outside the spinodal, small variations in composition will lead to an increase in free energy and the alloy is therefore metastable. The free energy of the system can only be decreased in

this case if nuclei are formed with a composition very different from the matrix. Therefore, outside the spinodal, the transformation must proceed by a process of nucleation and growth. Normal down-hill diffusion occurs in this case. The changes in composition profile for both types of transformation are shown in figure 3.12.

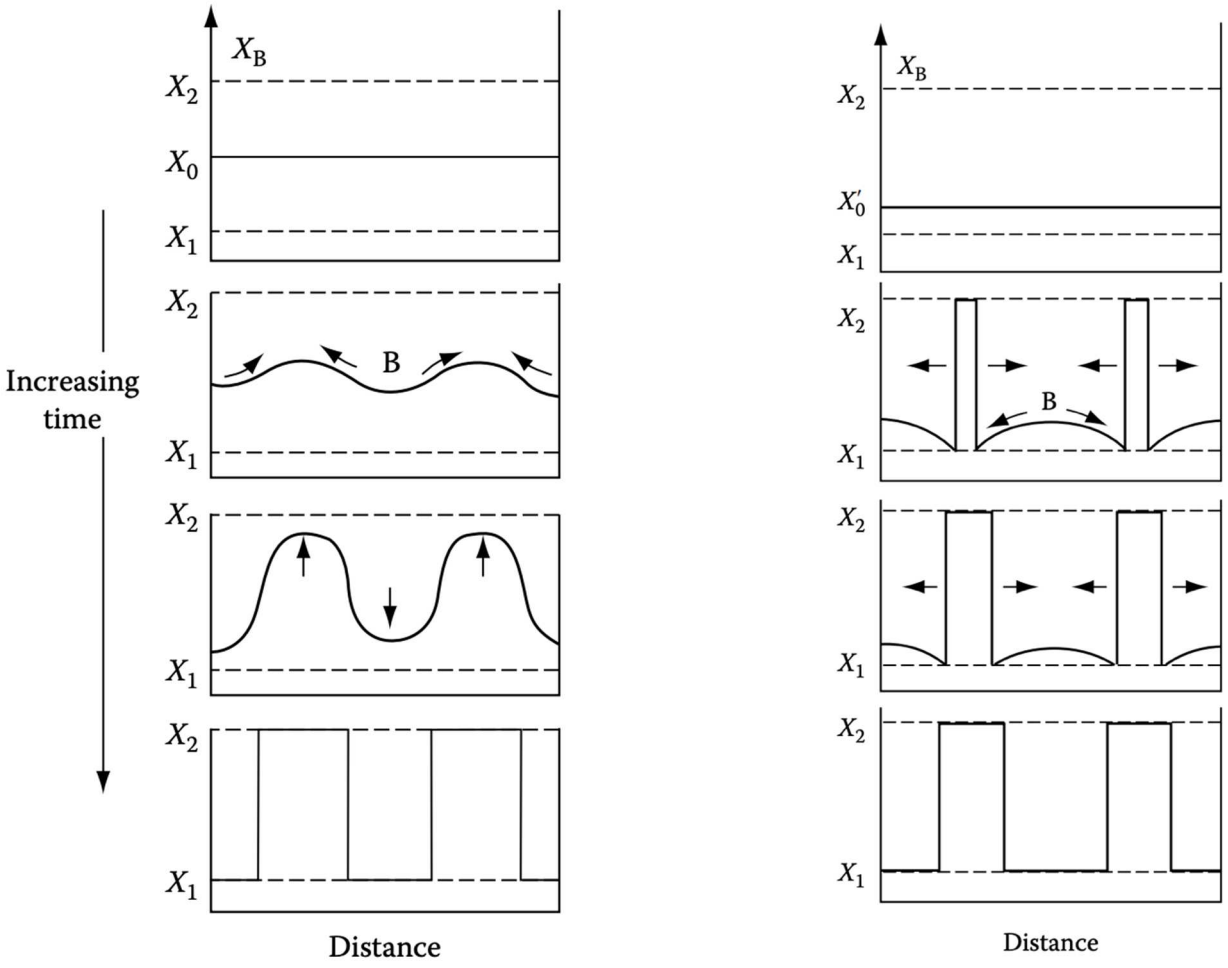

Figure 3.12 Schematic composition profiles at increasing times in (a) an alloy quenched into the spinodal region (X_0 in Figure 3.11) (b) alloy outside the spinodal points (X'_0 in Figure 3.11) [15].

The rate in which spinodal transformation occurs is controlled by the interdiffusion coefficient, D. Within the spinodal region $D < 0$ due to up-hill diffusion and the compositional

fluctuation will increase exponentially with time, with a characteristic time constant $\tau = -\lambda^2/4\pi^2$, where λ is the wavelength of the composition modulations. The rate of transformation can therefore become very high by making λ as small as possible. However, there is a minimum value of λ below which spinodal decomposition cannot occur. Parameters affecting λ are interfacial energy effects, and coherency strain energy effects.

The magnitude of interfacial energy effects depends on the composition gradient across the interface, also known as gradient energy. In solid solutions which tend to cluster, the energy of like atom-pairs is less than that of unlike pairs. Thus, the origin of the gradient energy is the increased number of unlike nearest neighbors in a solution containing composition gradients compared to a homogeneous solution. Additionally, coherency strain energy effects can arise If the size of the atoms making up the solid solution are different [15][16].

An important question to be answered is how to diffrentiate between nucleation induced transformations and spinodal decomposed nanostructures. Table 3.1 provides a comparison between the two phenomena [17].

Table 3.1 Comparison between nucleation and growth transformations and spinodal decomposition [17].

Nucleation and growth	Spinodal decomposition
Invariance of second phase composition to time at constant temperature	Continuous variation of both extremes in composition with time until equilibrium compositions are reached
Interface between phases always has the same degree of sharpness during growth	Interface between phases initially is very diffuse, eventually sharpens
Tendency for random distributions of particle sizes and positions in matrix	Regularity of second phase distribution in size and position characterized by a geometric spacing
Tendency for separation of second phase spherical particles with low connectivity	Tendency for separation of second phase, no spherical articles with high connectivity

3.7 Spinodal decomposition in Ag-In system

In the context of studied Ag-In system, the metastable phase ζ firstly is formed during the homogenization stage of the Ag-In TLP bonding. Not affected by the cooling rate, the metastable phase ζ could transform into this two-phase nanostructure through spinodal decomposition mechanism. As mentioned, spinodal decomposition would occur when the second derivative of Gibbs free energy to composition is negative. Upon infinitesimal composition fluctuation, a metastable phase would continuously transform into two stable phases, not hindered by any thermodynamic barrier, thereby forming a distinctive spinodal morphology in nano-scale. The metastable phase ζ firstly is formed during the homogenization stage of the Ag-In TLP bonding. Not affected by the cooling rate, the metastable phase ζ could transform into this two-phase nanostructure through spinodal decomposition mechanism. Since the context of Ag-In spinodal decomposition has never been discussed before, we hereby performed a thermodynamic calculation to prove its conceptual validity.

According to Ag-In binary phase diagram (see figure 1.7), the responsible metastable phase for the spinodal decomposition would be at the ζ phase range. Adopting the sub-regular solid solution model, the Gibbs energies for the binary solution phase can be calculated from the eq. 3.2:

$$G = \sum_{i=1}^{2} x_i G_i^0 + RT \sum_{i=1}^{2} x_i \ln(x_i) + \Delta G_{ex} \qquad (3.2)$$

Where the first term represents the Gibbs energies of the pure components, the second term is the ideal Gibbs energy of mixing, and the excess Gibbs energy of mixing ΔG_{ex} is usually expressed in the Redlich-Kister polynomial form [18], as shown in eq. 3.3:

$$\Delta G_{ex} = x_1 x_2 \sum_{n=0}^{2} L_{12}^{n}(x_1 - x_2)^n \quad (3.3)$$

In the Ag-In binary system case, we let x_1=x_{In}, x_2= x_{Ag}, if adopting the first-two terms in the Redlich-Kister polynomial form, then the molar free energy of the ζ phase, G_m^{ζ}, is expressed with eq. 3.4:

$$G_m = x_{Ag}G_{Ag}^{0} + x_{In}G_{In}^{0} + RT\,[x_{Ag}\ln(x_{Ag}) + x_{In}\ln(x_{In})] + x_{Ag}x_{In}[L_0 + L_1(x_{In} - x_{Ag})] \quad (3.4)$$

Let x_{In} = c, x_{Ag}= 1-c, then we have the eq. 3.5:

$$G_m = (1-c)G_{Ag}^{0} + cG_{In}^{0} + RT\,[(1-c)\ln(1-c) + c\ln(c)] + c(1-c)[L_0 + L_1(2c-1)] \quad (3.5)$$

The first derivative of the molar free energy of the ζ phase is given by the eq. 3.6:

$$\frac{\partial G_m}{\partial c} = -G_{Ag}^{0} + G_{In}^{0} - RT\ln(1-c) + RT\ln c + L_0(1-2c) - L_1(1 - 6c + 6c^2) \quad (3.6)$$

Upon the occurrence of spinodal decomposition, the second derivation of molar free energy is less than zero, as shown in the eq. 3.7:

$$\frac{\partial^2 G_m^{\zeta}}{\partial c^2} = \frac{RT}{c(1-c)} - 2L_0 + 6L_1(1-2c) < 0 \quad (3.7)$$

For the ζ phase in the Ag-In system, the thermodynamics parameters can be found in the literature [19]:

G_{Ag}^{0} = 300 + 0.3T; G_{In}^{0} = 533 - 0.6868T; R = 8.314 J/mol.K;

L_0 = -13625.3 + 0.13T; L_1 = -42727.0 + 24.89T; (in units of J/mol)

Using the numerical values of the thermodynamics parameter above, the molar Gibbs free energy and the second derivation of molar free energy can be calculated at the room temperature (298K) and the bonding temperature (463K). As a result, the G_m and G''_m thermodynamic calculation graphs are plotted and shown below.

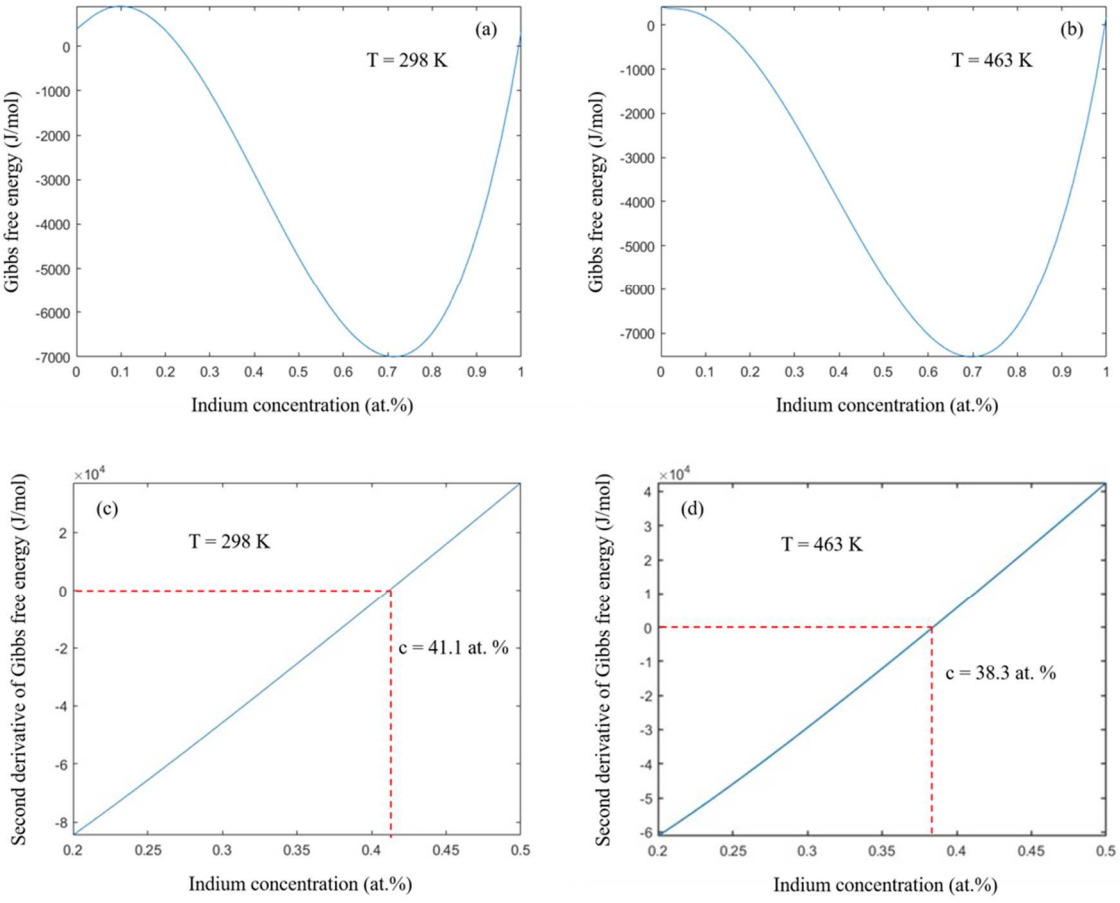

Figure 3.13. The thermodynamic calculation results for the ζ phase in Ag-In system, (a) the molar Gibbs free energy Gm at 298 K; (b) the Gm at 463 K; (c) the second derivation of Gm at 298K; (d) the second derivation of Gm at 463K.

According to the Ag-In phase diagram (see figure 1.7), the metastable ζ phase exists over the indium concentration range from 20 at.% to 45.9 at.% under thermal equilibrium. Therefore, we only consider this range as the possible Ag-In spinodal decomposition range for the ζ phase. According to the thermodynamic calculation results, the second derivative of G_m has a negative value over the compositional range from 20 at.% to 41.1 at.% at 298 K, and has a negative value over the compositional range from 20 at.% to 38.3 at.% at 463 K. According to the Ag-In phase diagram, the ζ phase is not the stable phase under thermal equilibrium if c is less than 25 at.%. At 463 K, the ζ phase can co-exist with Ag-In solid solution phase in the compositional range between 20 at. % to 25 at.% (indium concentration). Therefore, considering both criterion with the ζ phase stability and the second derivative of the Gibbs free energy, the compositional range (indium concentration) of the Ag-In spinodal decomposition can be estimated as [0.25, 0.411] at 298K and [0.2, 0.383] at 463 K. It should be noted that the internal stress/strain might also affect the spinodal decomposition conditions, but we did not include this factor in the thermodynamic calculations at this study. Contrary to second-phase precipitation, the spinodal nanostructure is homogeneous throughout the whole material cross-section with a relatively uniform size distribution. The matrix phase γ, an intermetallic compound (IMC), provides rigidity for the entire VECSEL-to-diamond integrated structure, but suffers from the brittleness in its nature. Notably, a high-load shear stress has been exerted on the VECSEL-to-diamond structure during the GaAs mechanical lapping, which possibly initiated a few nano-cracks within the IMC phase, as circled in Figure 3.8 (c) and (d). Fortunately, the embedded phase α', a highly ductile ordered solid solution, can compensate the brittleness of the matrix phase, whereby

stopping the nano-cracks from further long-range propagation. Therefore, the Ag-In spinodal nanostructure effectively acts as a nanocomposite with two complementary phases, mechanically benefiting from the spinodal strengthening mechanism at the same time.

3.8 Conclusion

In summary, the feasibility of VECSEL-to-diamond heterogeneous integration with the low-temperature Ag-In spinodal bonding is demonstrated. Proven with lasing experiments, the SGA and SGB VECSEL devices were both functional at the high-power lasing regime, demonstrating an excellent thermal dissipation capability with the Ag-In spinodal bonding layer. With economic considerations, the Ag-In spinodal bonding would be a cost-effectively alternative choice for the VECSEL and other high-power photonics packaging. Studying the discovered Ag-In spinodal nanostructure within the Cahn-Hilliard framework in the future is strongly suggested.

References

[1] M. Kuznetsov, F. Hakimi, R. Sprague, and A. Mooradian, "High-power (>0.5-W CW) diode-pumped vertical-external-cavity surface-emitting semiconductor lasers with circular TEM 00 beams," *IEEE Photonics Technol. Lett.*, vol. 9, no. 8, pp. 1063–1065, Aug. 1997.

[2] Y. Huo, C. Y. Cho, K. F. Huang, Y. F. Chen, and C. C. Lee, "Exploring the DBR superlattice effect on the thermal performance of a VECSEL with the finite element method," *Opt. Lett.*, vol. 44, no. 2, p. 327, Jan. 2019.

[3] B. G. Yacobi, S. Zemon, P. Norris, C. Jagannath, and P. Sheldon, "Stress variations due to microcracks in GaAs grown on Si," *Appl. Phys. Lett.*, vol. 51, no. 26, pp. 2236–2238, 1987.

[4] S. Weiß, E. Zakel, and H. Reichl, "Mounting of high power laser diodes on diamond heatsinks," *IEEE Trans. Components Packag. Manuf. Technol. Part A*, vol. 19, no. 1, pp. 46–53, Mar. 1996.

[5] X. Liu *et al.*, "A study on the reliability of indium solder die bonding of high power semiconductor lasers," *J. Appl. Phys.*, vol. 100, no. 1, 2006.

[6] C. C. Lee, C. Y. Wang, and G. S. Matijasevic, "A New Bonding Technology Using Gold and Tin Multilayer Composite Structures," *IEEE Trans. Components, Hybrids, Manuf. Technol.*, vol. 14, no. 2, pp. 407–412, 1991.

[7] A. Rantamäki *et al.*, "High-power flip-chip semiconductor disk laser in the 13 μm wavelength band," *Opt. Lett.*, vol. 39, no. 16, p. 4855, Aug. 2014.

[8] B. Heinen *et al.*, "106 W continuous-wave output power from vertical-external-cavity

surface-emitting laser," *Electron. Lett.*, vol. 48, no. 9, pp. 516–517, Apr. 2012.

[9] Y. Huo and C. C. Lee, "The growth and stress vs. strain characterization of the silver solid solution phase with indium," *J. Alloys Compd.*, vol. 661, pp. 372–379, Mar. 2016.

[10] Y. Y. Wu, D. Nwoke, F. D. Barlow, and C. C. Lee, "Thermal Cycling Reliability Study of Ag-In Joints between Si Chips and Cu Substrates Made by Fluxless Processes," *IEEE Trans. Components, Packag. Manuf. Technol.*, vol. 4, no. 9, pp. 1420–1426, Sep. 2014.

[11] Y. Huo, J. Wu, and C. C. Lee, "Study of Anti-Tarnishing Mechanism in Ag-In Binary System by Using Semi-Quantum-Mechanical Approach," *J. Electrochem. Soc.*, vol. 164, no. 7, pp. C418–C427, 2017.

[12] C. A. Yang, J. Wu, C. C. Lee, and C. R. Kao, "Analyses and design for electrochemical migration suppression by alloying indium into silver," *J. Mater. Sci. Mater. Electron.*, vol. 29, no. 16, pp. 13878–13888, Aug. 2018.

[13] H. Schoeller and J. Cho, "Oxidation and reduction behavior of pure indium," *J. Mater. Res.*, vol. 24, no. 2, pp. 386–393, Feb. 2009.

[14] J. W. Cahn, "On spinodal decomposition," *Acta Metall.*, vol. 9, no. 9, pp. 795–801, Sep. 1961.

[15] D. A. Porter, K. E. Easterling, and K. E. Easterling, *Phase Transformations in Metals and Alloys (Revised Reprint)*. CRC Press, 2009.

[16] F. Findik, "Improvements in spinodal alloys from past to present," *Materials and Design*, vol. 42. Elsevier, pp. 131–146, 01-Dec-2012.

[17] M. Hillert, M. Cohen, and B. L. Averbach, "Formation of modulated structures in copper-nickel-iron alloys," *Acta Metall.*, vol. 9, no. 6, pp. 536–546, Jun. 1961.

[18] O. Redlich and A. T. Kister, “Algebraic Representation of Thermodynamic Properties and the Classification of Solutions,” *Ind. Eng. Chem.*, vol. 40, no. 2, pp. 345–348, Feb. 1948.

[19] T. M. Korhonen and J. K. Kivilahti, “Thermodynamics of the Sn-In-Ag solder system,” *J. Electron. Mater.*, vol. 27, no. 3, pp. 149–158, 1998.

Chapter 4

Prior-to-Bond Annealing Effects on the Diamond to Copper Heterogeneous Integration using Silver-Indium Multilayer Structure

4.1 Introduction

The development of electronics and optoelectronics is moving towards downscaling into smaller size and upholding higher power densities. These trends have raised the operating temperature of devices, thereby creating hotspots on the active chip. It is necessary to effectively remove the heat from hotspots in order for these devices to maintain their function with high efficiency and reliability [1]. The utility of diamond as a heat spreader has gained extensive attention over the past decade [2], because it has the highest thermal conductivity among any known bulk material. The cost of the artificial diamond synthesis, using chemical vapor deposition (CVD) method, has been significantly lowered due to the key technological advancements over the last decade.

In the context of OP-VECSEL packaging there is need for void free and mechanically robust bonding technologies in order to fully exploit the heat removal capability of the CVD diamond. Therefore, the diamond bonding technology become the bottleneck for the utility of the CVD diamond in the electronics and optoelectronics packaging and in the case of this study, the VECSEL flip-chip packaging. This chapter focuses on the Ag-In joints made between CVD diamond and copper submount in the flip chip package discussed earlier. This bond is made after the first bond is formed. Figure 4.1 shows the overall package, and the second/diamond-Cu joint is highlighted in the figure.

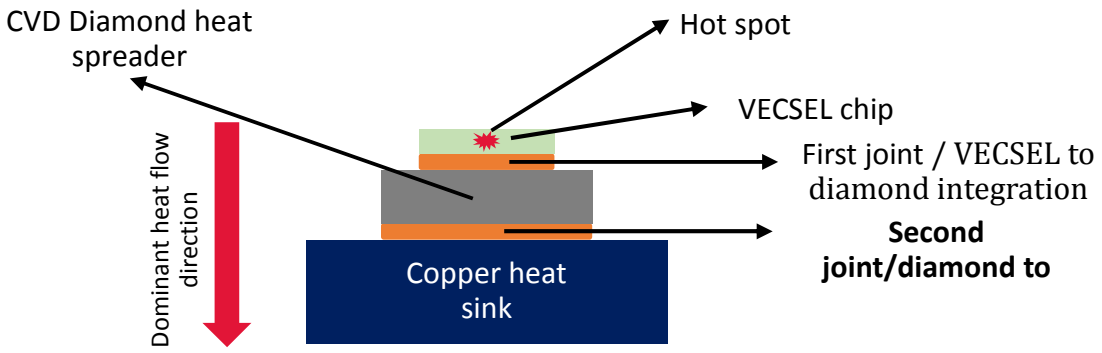

Figure 4.1. Schematic illustration of the VECSEL package

In the electronic manufacturing industry, Cu substrates have been commonly used as the structural component for the mechanical support and heat dissipation. Therefore, there is a practical need in finding the suitable bonding materials for the heterogeneous integration of the CVD diamond and the Cu substrate. Essentially, the large coefficient of thermal expansion (CTE) mismatch between CVD diamond (~1.0 ppm/K) and Cu (~15.5 ppm/K) must be addressed while developing the bonding materials or techniques [3]. A good choice would be originated from the metallic system with a high thermal conductivity and a good mechanical integrity. In addition, the bonding pressure and temperature should be low enough so that the various components do not suffer from the severe compressive stress and thermally induced mechanical stress during the heterogeneous integration process.

Conventionally, the Au-Sn eutectic solder and the indium foils have been used as bonding/thermal interface materials (TIM) for the bonding of the CVD diamond. High processing temperature and high material cost for Au-Sn eutectic (>300°C) and the creep phenomenon at elevated temperatures for indium foils, respectively, are known as the main drawbacks in utilization of those material systems [4].

In the literature, the Ag-In binary system has been demonstrated as a promising bonding material system [5], to provide bonding joints with high strength [6], high thermal stability and fatigue resistance [7]. The Ag-In system can be used to perform the bonding process at relatively low temperatures, specifically in the range of 200°C, whereas the resulting joints can be thermally stable up to 900°C. For the specific application, the final joint microstructure can be tailored accordingly. Ag has the highest thermal conductivity (410 W/m.K) among all known metals. Moreover, it has been shown that Ag-In alloys possesses the superior mechanical properties [8] and the anti-tarnishing property [9]. Therefore, it would be an excellent choice to develop the Ag-In system as an alternative engineering solution for the CVD diamond to Cu heterogeneous integration.

In the Ag-In system, even at room temperature, if In is brought into contact with Ag, the $AgIn_2$ intermetallic compound (IMC) would be formed. The formation of $AgIn_2$ IMC is a very rapid chemical process. With only one day aging at room temperature, a 5 μm thick In layer would be fully consumed by the Ag substrate, and is completely converted into $AgIn_2$ IMC [10]. It is well documented that Ag diffuses into In mostly through interstitial sites, while In diffuses into Ag through grain boundaries. For the bonding applications, the rapid consumption of In before reaching the bonding temperature is not desirable. Undersupply of molten phase during the bonding process has been identified as a severe issue. In the earlier works, we have demonstrated that if Ag grain size is increased prior to bonding, the issue of the lack of molten In during bonding could be properly resolved in principle [11]. However, the detailed microstructural evolution analysis of the bonding joint and further quantitative study of joint strength were not carried out in the earlier works. In the current research, we have

conducted a more thorough examination the microstructure of joint and provided corresponding shear strength data in the case where the bond thickness is drastically reduced from the previous work, specifically, from 100 μm to 30 μm, for thermal dissipation purposes. Most recently, the initial successful bonding of CVD diamond to Cu has been reported in a preliminary work [12]. Here, in the case of interconnecting CVD diamond to Cu, we would further systematically elaborate the microscopic bonding mechanism with the prior-to-bond annealing effects in controlling Ag grain size.

4.2 **Experimental Procedure**

As schematically shown in Figure 4.2, the bonding structure is designed so that the final joint composition would be (Ag) with ~20 at% In. Commercially available CVD diamonds were cut with laser into 3 mm × 3 mm dies, and 10 mm × 10 mm Cu blocks were used as the substrate. The thickness of the diamond and Cu were 300 μm and 4 mm respectively. As for the choice of metallization on diamond, the use of carbide forming species, such as Cr, W and Ti is preferred as the first contact layer to diamond. Subsequently, a diffusion barrier layer, such as Ni, can be used between the first contact layer and the final metallic layer, in order

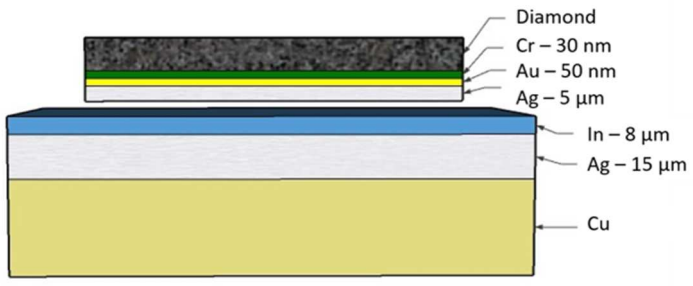

Figure 4.2 Metallization and multi-layer silver-indium structure for bonding diamond to copper

to prevent any reaction between these two layers [13]. Although the use of different layers may be necessary for good adhesion and prevention of chemical reactions between different species, increasing the number of layers will result in an increase of the overall thermal resistance due to additional interfacial thermal resistance. In this study, a Cr/Au metallization on CVD diamond was used. No metallization layer was used on the Cu substrate since Ag inherently adheres well to Cu.

The CVD diamond surface was initially cleaned with acetone and isopropanol, followed by an oxygen plasma cleaning procedure for 1 minute. Afterwards, a seed layer of Cr 30 nm/Au 50 nm/Ag 1μm was deposited on CVD diamond surface, using E-beam evaporation in a single vacuum cycle. Cr is a strong carbide forming element. By using Cr, the use of diffusion barrier layer can be avoided since it does not react with the neighboring Au layer. The Au layer prevents Cr from oxidation and provides good adhesion to Ag. The final Ag layer acts as a seed layer for the subsequent electroplating process. Since diamond is electrically insulating, such a conductive seed layer is needed for the electroplating process. Following E-beam evaporation, the diamond with the seed layer was annealed at 300 °C for 1 hour in 60 mtorr vacuum. This annealing step can improve the adhesion between Cr and diamond, through the formation of Cr carbide compound [14]. Figure 4.3 shows the effect of this annealing step on the adhesion between CVD diamond and Cr interface. If the annealing step is eliminated and the subsequent Ag layer is electroplated, internal stresses cause the coated layers to delaminate as shown in figure 2. (b). Thus, the annealing step was added and after that, a 4 μm Ag layer was electroplated on the top of seed layer, and then the diamond would be ready for the following bonding process.

The Cu substrate was fine polished using 0.5 μm suspended diamond slurries. Fine polishing of Cu substrate will result in a reduced final surface roughness after electroplating the Ag layer (see figure 4.4). Thus, it facilitates the bonding process by providing more contact area. In general the smoother the bonding surface, there will be more contact area and a better joint can be obtained. The RMS value for surface roughness for the electroplated Ag layer measured from SEM images is 3.4 μm and 0.8 μm for non-polished and polished copper substrate respectively.

Following the polishing process, 15 μm Ag and 8 μm In were respectively electroplated on the Cu in a sequence. The backside of Cu substrate was coated with lacquer to prevent Ag or In deposition during electroplating process. The Ag plating solution is a cyanide-free, mildly alkaline at pH 10.5, and the In plating solution is a sulfamate In bath at pH of 1–3.5. The bath

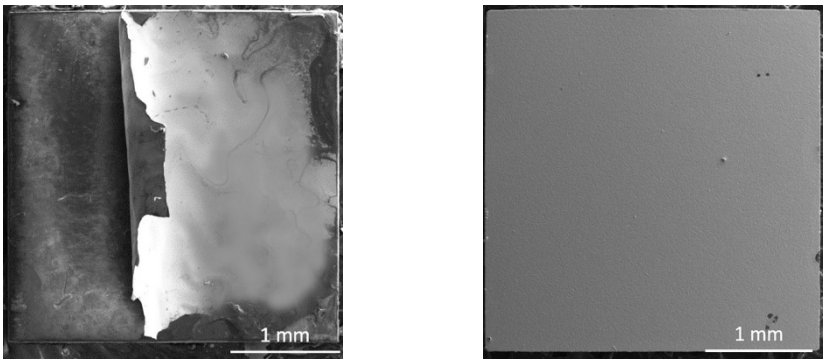

Figure 4.3 (left) Cr/diamond interface delamination after electroplating the Ag layer (b) No delamination at Cr/diamond interface due to annealing of diamond and seed layer at 300°C for 1 hr prior to Ag electroplating

was kept at room temperature for both plating solutions. The plating current density was 13 mA/cm^2 for Ag and 22 mA/cm^2 for In. Since In is prone to oxidation at room temperature, in our previous studies on Ag-In joints, a thin cap layer was used to suppress the In oxidation. However, in this study, we eliminated the cap layer, and our results showed that the

successful bonding can still be carried out even without the cap layer. It is believed that the applied pressure will rupture the native In oxide layer and further oxidation should be very limited during the vacuum bonding process.

In the bonding process, the diamond chip was placed on top of Cu substrate and held by a fixture with 200 psi (1.37 MPa) static pressure to ensure intimate contact. The assembly was mounted on a graphite platform in a vacuum furnace, which was pumped to 60 mtorr to suppress In oxidation during bonding [15]. The platform was heated, and the sample

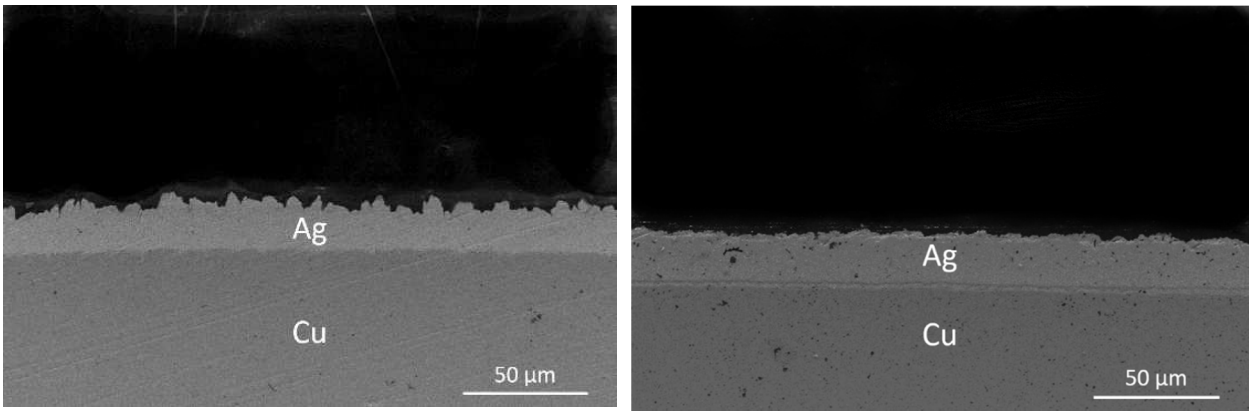

Figure 4.4 (left) As received Copper substrate used as substrate for electroplating Ag (right) Copper substrate fine polished prior to electroplating Ag

temperature was monitored by a miniature thermocouple. The bonding temperature was set at 210°C with a dwell time of 15 min. Then, the assembly was naturally cooled in 60 mtorr vacuum, taking 90 mins to reach room temperature. In order to enlarge the Ag grain size, the prior-to-bond annealing process of Ag was carried out in air and 60 mtorr vacuum,

respectively, for 3 hours at 350°C. No flux was used for all bonding processes. Figure 4.5 shows the assembled diamond-copper module.

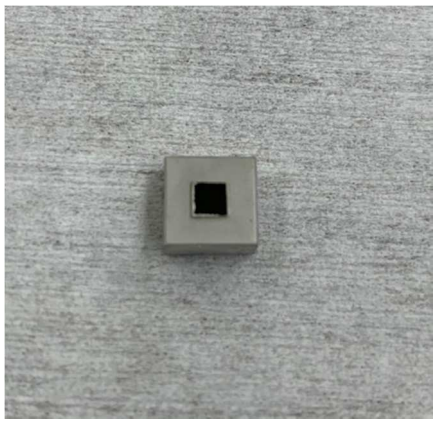

Figure 4.5 Assembled diamond-copper module

Due to the hardness of diamond, the preparation of metallographic cross-sections using the conventional polishing technique is not applicable. Therefore, the bonded samples were sheared, and the fracture surface was thoroughly studied with SEM-EDX. In addition, the Focused Ion Beam (FIB) was used to cut trenches into the fracture surface to reveal the cross-sectional microstructure of the joint. The shear tests were carried out using a STR-1000, Rhesca bonding tester machine. The tip velocity was set at 21 mm/min and the fly height from the Cu substrate was 50 μm.

The X-ray photoelectron spectroscopy (XPS) studies were performed with a monochromatized Al K_α radiation source ($h\nu$ = 1486.6 eV). All data were collected with an analyzer pass energy of 20 eV with the spot size of 300 μm × 700 μm. The scanning energy resolution was 0.05 eV with a dwell time of 100 ms. The XPS survey and region spectra reported were measured with an average of 7 and 11 scans, respectively.

4.3 Results

4.3.1 Prior-to-bond Annealing of Ag

4.3.1.1 As-plated Ag

As-electroplated Ag is considered to be the reference specimen with fine grain size. Figure 4.6 (a) and (b) show the surface morphology and internal FIB cross-sectioned microstructure of the as-plated Ag layer, where the electroplating process produces a rough and flake-like Ag microstructure. A dendritic morphology with nano-range grain size was observed for the as-plated Ag. According to X-ray diffraction findings in an earlier study by our research group, the mean grain size for this group of samples was approximately 9.3 nm [11]. Another good reference of the Ag grain size given from the electroplating solution manufacturer is ranging from 10 nm to 30 nm.

4.3.1.2 Annealed Ag

In order to increase the Ag grain size, the annealing procedure of Cu substrate with Ag electroplated on its surface, namely, the prior-to-bond annealing, was carried out in air and under vacuum respectively. It was observed that the prior-to-bond annealing process at temperatures higher than 350°C would result in formation of blisters on the Ag surface. Thus, annealing at 350℃ for 3 hours was implemented. Figures 4.6 (c-f) show the top view and the FIB cross-sectioned view of Ag layer after annealing in air and vacuum respectively. Annealing in air resulted in a porous Ag microstructure and a complete re-construction of Ag surface morphology. As for the vacuum annealing, the grain enlargement has occurred

without formation of any porosity. Based on the SEM observations, the mean diameters for Ag grains after annealing in air and vacuum were approximately 1 μm and 0.7 μm respectively. The annealing process resulted in approximately 30 to 100 times increase in the Ag grain size.

The XPS experimental studies were performed to probe the surface chemistry alternation of the prior-to-bond samples with and without annealing process. As shown in figure 4.7 (a), the distinctive Cu peaks were identified in the XPS survey spectra of both annealed specimens. Therefore, the Cu atoms from the substrate has diffused all the way through the

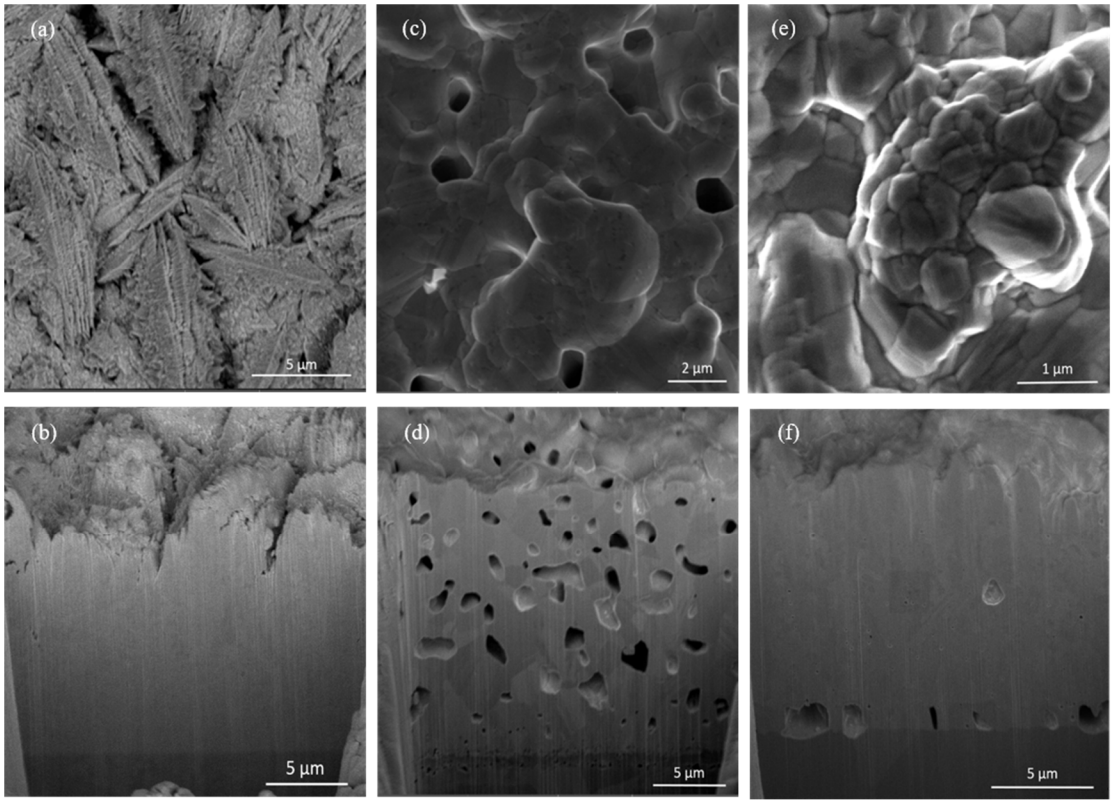

Figure 4.6 The SEM image of the Ag electroplated on Cu: (a) top view and (b) FIB trenched cross-section of as-plated Ag on Cu (Design I); (c) top view and (d) FIB trenched cross-section of Ag on Cu annealed at 350°C for 3 hours in air (Design II); (e) top view and (f) FIB trenched cross-section of plated Ag on Cu annealed at 350°C for 3 hours in 60 mtorr vacuum (Design III).

15 μm Ag layer, and already reached to the top free surface of Ag. In addition, it was unexpected that the S peaks showed up in the survey spectrum of the vacuum annealed Ag sample, whereas the S peaks were absent in the as plated and the air annealed samples. This distinctive feature will be further discussed in the following sections.

The Ag 3d region spectrum for the as-plated, air annealed and vacuum annealed samples were shown in figure 4.7 (b). According to the literature, Ag 3d 5/2 binding energies for pure

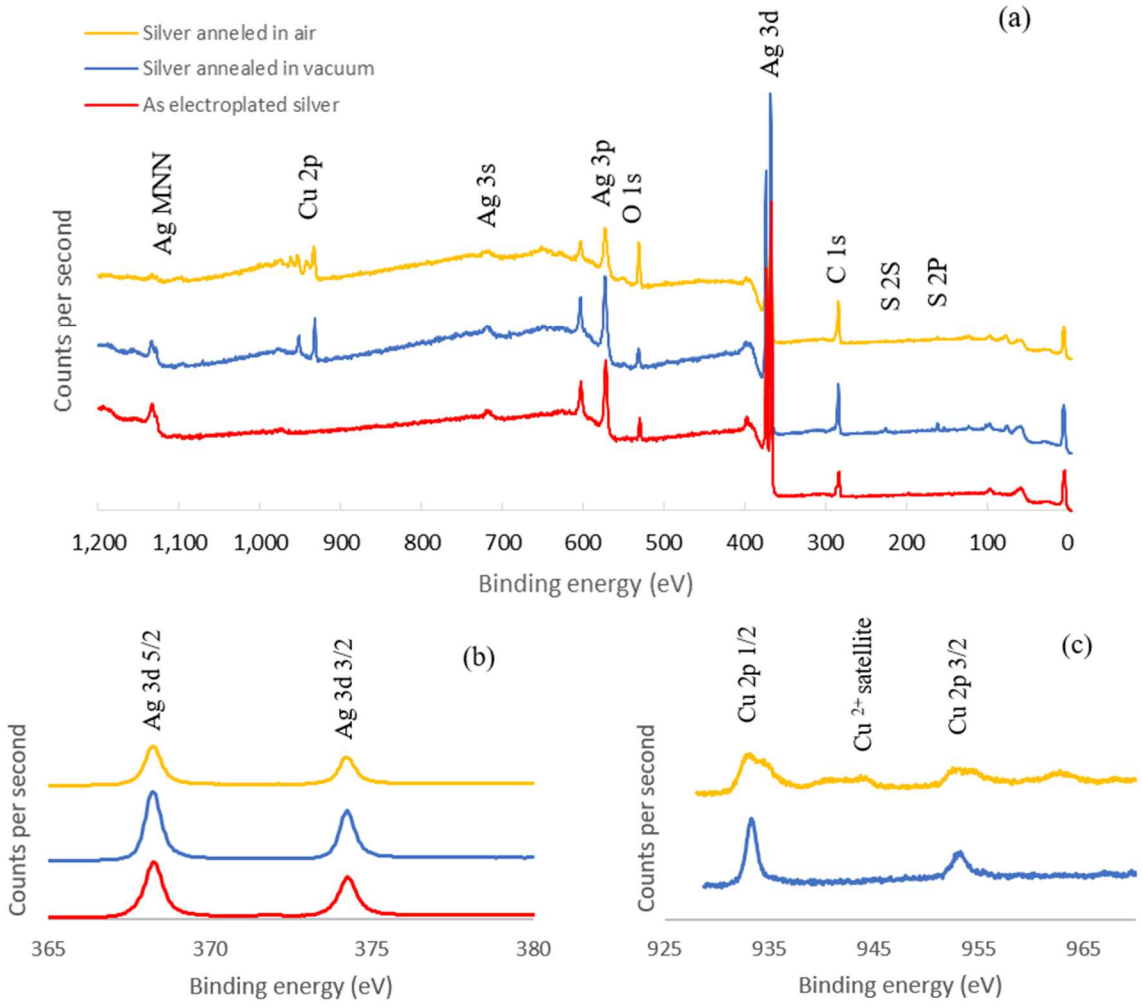

Figure 4.7 The XPS spectra for the electroplated Ag on Cu before and after the prior-to-bond annealing in air and vacuum: (a) the overall survey spectra (b) the region spectra for Ag 3d peaks; (c) the region spectra for Cu 2p peaks

Ag and Ag_2S are at 368.2 eV and 368.1 eV, respectively [17]. If the Ag oxides crystalline formed, a broadening in peaks and shift to lower binding energies should have occurred [9]. The range of the Ag 3d 5/2 was shifted from 368.2 eV to 368 eV, for the annealed Ag in air and vacuum. It indicated that no Ag oxides was formed on the surface after annealing in either environment. However, since Ag_2S occurs at a peak of 368.1 eV without any additional satellite peaks, the existence of such sulfide compound cannot be ruled out for the vacuum annealed specimen.

Figure 4.7 (c) shows the regional scan for the Cu 2p peaks, the existence of satellite peaks along with the peaks at 933.2 eV and 952.5 eV can be assigned to Cu 2p 3/2 and Cu 2p 1/2 of Cu^{2+} in CuO for the case of Ag annealed in air. The regional spectra of Cu 2p in the vacuum annealed sample did not show the satellite peaks of CuO. It showed peaks at 933.1 eV and 952.1 eV, which can be assigned to Cu 2p 3/2 and Cu 2p 1/2 for the pure Cu [18].

4.3.2 Joint Microstructure

For the purpose of brevity, the bonding results are categorized into the following 3 groups:

Design I: As-electroplated Ag is used for the bonding.

Design II: Ag annealed in air is used for the bonding.

Design III: Ag annealed in vacuum is used for the bonding.

4.3.2.1 Design I

Figure 4.8 (a) shows the overall view of the fracture surface on the Cu side after shear tests on the design I specimen. Two types of distinct areas can be identified. As depicted in figure 4.8 (a), the first region contains Cr, indicating the Cr/diamond interface was delaminated at

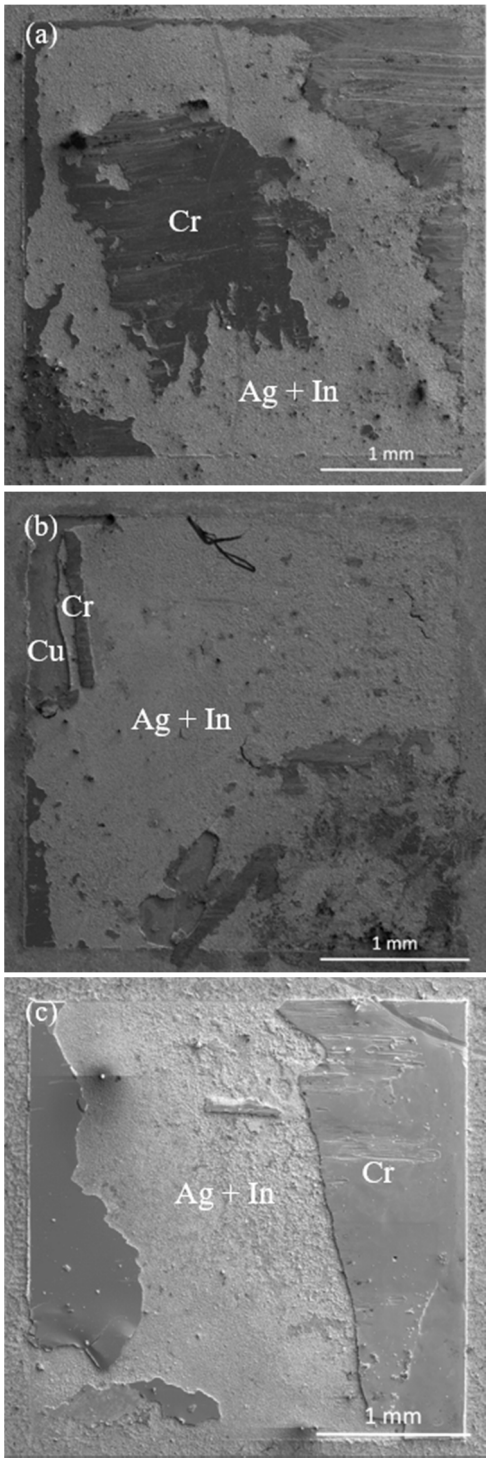

Figure 4.8 The overall view of the fracture surface on the Cu substrate after die shear test (a) Design I (b) Design II and (c) Design III

this region during the shear test. The Cr/diamond delamination occurred in all sheared

samples, implying that interfacial adhesion between Cr and diamond at some region was not strong enough to sustain the shear force. At the other type of fracture surface, a mixture of Ag and In signals were detected by EDX, indicating a cohesive fracture within the joint upon shear. The EDX results showed the mixture of Ag and In quantified as 69.5 at. %, and 30.5 at. % respectively. Since the EDX signal was generated from an interaction volume/depth of few micrometers within the sample, the exact phase and composition at the fracture surface of the layered structure cannot be precisely determined here. At the Cr/diamond delamination region, the original joint was still intact. Therefore, this region was selected for FIB cross-sectioning. A trench was cut into this area with FIB to reveal the microstructure of the Ag-In joint after bonding.

Figure 4.9 (a) shows the FIB trenched cross-section within the joint of design I. Note that left side of figure 4.9 (a) is the Cr/diamond interface, and the right side is the Ag-In joint near the Cu substrate. Thus, the initial bonding interface is at the distance approximately 5 μm from the left side. A number of isolated voids can be found in this region, where In on the Cu side would come into contact with Ag on the diamond side. In figure 4 (a), the height of intact layer (Cr/diamond delaminated area) from the fracture surface (Ag-In mixture area) is also approximately 5 μm, indicating that the majority of cohesive fracture has occurred along the initial bonding interface. Therefore, it is safe to conclude that the initial bonding interface has the weakest interfacial strength in the design I, due to the formation of such isolated voids. As elaborated in the previous study [11], the lack of molten phase during the bonding process was responsible for the generation of isolated voids at the initial bonding interface. As depicted in Figure 4.9 (b), the EDX line scan analysis was conducted from the Cr/diamond

side towards Cu substrate side, matching the corresponding FIB sectioned SEM image above. The EDX point analysis of the Figure 4.9 (a) is also recorded in table 4.I. Based on the EDX data, the composition of the joint from Cr/diamond side to about 13 μm within the joint, is corresponding to Ag_2In. The EDX line scan signals for both Ag and In dropped at the isolated void region along the scan path. Fracture occurred in this phase and along the isolated voids. Moving towards Cu substrate, the relative In EDX signal decreases, and the corresponding phase should be Ag solid solution with In. Some Cu and Au EDX signal were also detected along the line scan path. It is known that Au can dissolve into Ag lattice, whereas Cu is immiscible with Ag. However, the Cu atoms can diffuse through the Ag lattice during the bonding process. At EDX detecting point 5 and point 6, the Cu concentration has reached above 15 at. %. In order to achieve a complete homogenous joint with silver indium solid

solution phase, a post-bonding annealing process must be conducted, which will not be further discussed in the current study.

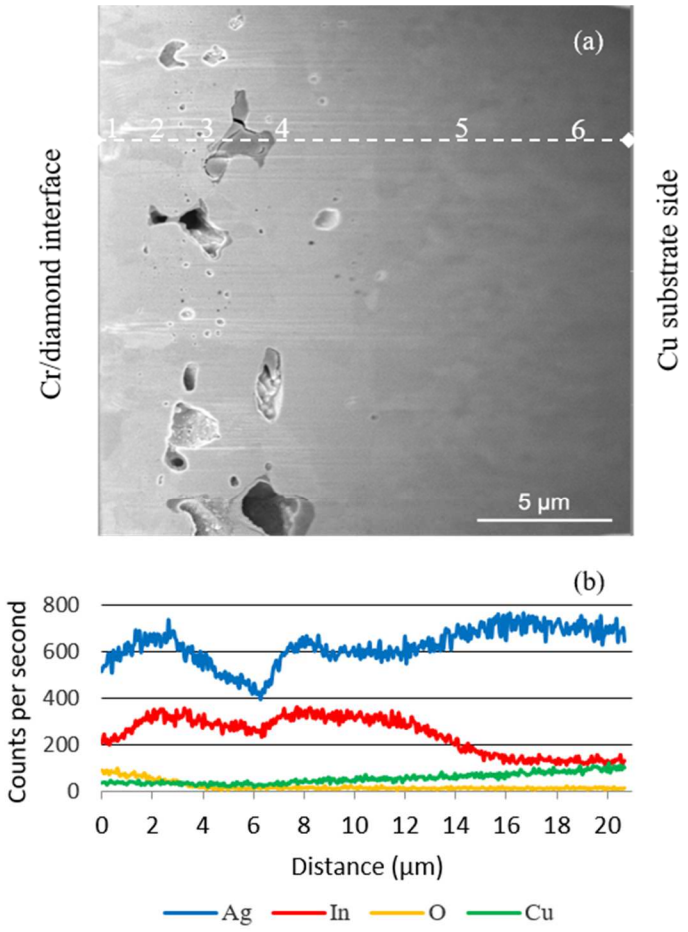

Figure 4.9 (a) The FIB cross-sectioned view through intact joint at the fracture surface of Design I; (b) the EDX line scan results for the line shown in (a).

Table 4.1 The EDX quantitative analysis results for the points marked in Figure4.9 (a)

	1	2	3	4	5	6
Ag at.%	69.3	69.5	72.1	72.3	70.3	77.8
In at.%	24.8	25.6	21.5	19.6	14.2	6.8
Cu at.%	2.3	3.7	6.3	7.9	15.3	15.9
Au at.%	3.4	1.5	–	–	–	–

4.3.2.2 Design II

In design II, the electroplated Ag was annealed in air, followed with the In electroplating process and the subsequent bonding process. As shown in Figure 4.8 (b), similar to design I, there are regions in which fracture happened through the Ag-In joint structure, whereas the Ag-In joint remained intact in the other regions. The EDX spectrum at the Ag-In fracture region in figure 4.8 (b), shows a mixture of Ag and In quantified as 79.5 at. % and 20.4 at. %, respectively, where no major Cu signal was detected. Additionally, as depicted in Figure 4.8 (b), an intensive Cu EDX signal was detected, which was believed to be the initial Ag/Cu interface. The detected Cu at this region has been oxidized to form CuO, as a result of O diffusion through Ag during the prior-to-bond annealing of Ag. At the fracture region where joint has remained intact, the FIB cross-sectioned view of the bonding joint was captured, which was shown in the figure 4.10 (a).

First of all, as shown in figure 4.10 (a), no major voids can be found in the region close to initial bonding interface. This proves that the enlargement of the Ag grain size has effectively slowed the diffusion of In into Ag, by reducing the density of the grain boundary. However, a secondary phase can be found in the microstructure of the bonding joint of design II, as labelled in figure 4.10 (a). The secondary phase has an elongated shape and is parallel to the bonding interface. In design II, the fracture of the joint occurred at a depth corresponding to the location abundant with this secondary phase, approximately at a distance of 15 μm from Cr/diamond interface surface.

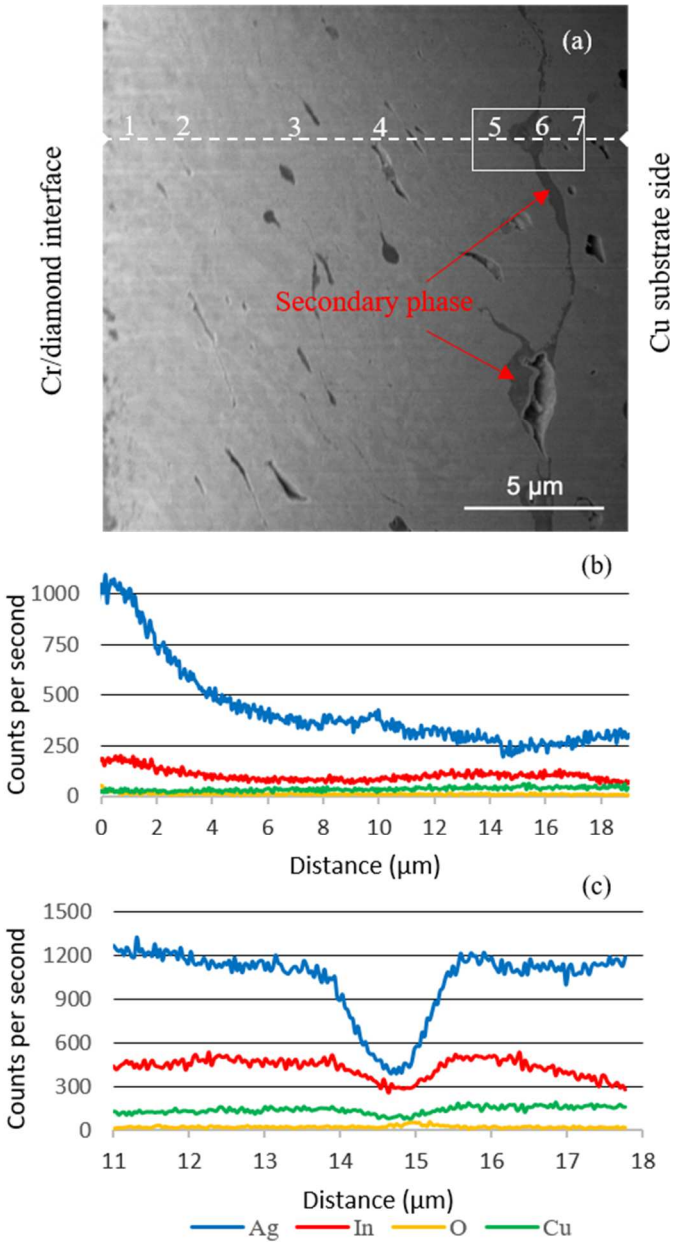

Figure 4.10 (a) The FIB cross-sectioned view through intact joint at the fracture surface of Design II; (b) the EDX line scan for the line shown in (a); (c) the EDX line scan for the second phase within the labeled box in (a).

Table 4.2 The EDX quantitative analysis results for the points marked in figure 4.10 (a)

	1	2	3	4	5	6	7
Ag at.%	90.1	89.6	89.1	88.3	77.8	69.4	74.6
In at.%	6.7	8.7	8.7	9.5	13.75	17.3	13.1
Cu at.%	0.6	1.6	2.2	2.3	8.35	12.4	12.2
Au at.%	2.1	–	–	–	–	–	–

The corresponding EDX line scans are shown in figure 4.10 (b) and (c), and the EDX point analysis is also recorded in table 4.2. As seen from the data, the results of the EDX point scan suggested an abnormal indium diffusion occurred during the bonding process. At the EDX point 1 to 4, the concentration of In was less than 10 at. %. This region was near to the initial bonding interface, which should have been abundant with indium. However, the concentration of In is higher at the region of point 5 to 7, which is corresponding to the location of the secondary phase. As shown in figure 4.10 (c), a localized EDX line scan was performed at the region near the secondary phase. The Ag EDX signal dropped significantly at the 1 μm thick secondary phase region, while the In EDX signal almost remained the same intensity. This region corresponds to the initial Ag/In interface, which already contained CuO before indium electroplating process, as shown in the previous XPS data. Therefore, it is reasonable to identify this secondary phase as a mixture of metallic oxides, a combination of In_2O_3 and CuO. Therefore, it is safe to conclude that the Ag/In interface on the Cu side has the weakest interfacial strength in design II, due to the formation of such metallic oxides phase.

4.3.2.3 Design III

In design III, the electroplated Ag annealed in vacuum was used to bond CVD diamond to Cu substrate. Similar to design I, as shown in the figure 4.8 (c), the fracture surface after shear test had two types of distinct areas, namely, the Cr/diamond delamination and the fracture within the bonding joint. Similarly, the intact bonding joint region was cross sectioned with FIB, and its microstructure was further studied, as shown in figure 4.11 (a). Similar to the

results of design II, no voids exist at the initial bonding interface. Therefore, the issue of the undersupply of the molten phase during bonding process was also resolved by the vacuum annealing process.

However, a different type of voids and another new phase embedded in the joint, were observed at the initial Ag/In interface, whose locations matched the depth of the major cohesive fracture surface within the joint. The EDX data quantified the Ag and In concentration, at the major fracture surface, as 81.3 at. % and 18.2 at. %, respectively. The sulfur (S) elemental signal can be distinctly identified at the region of the embedded phase in both data of the EDX line scan and point analysis.

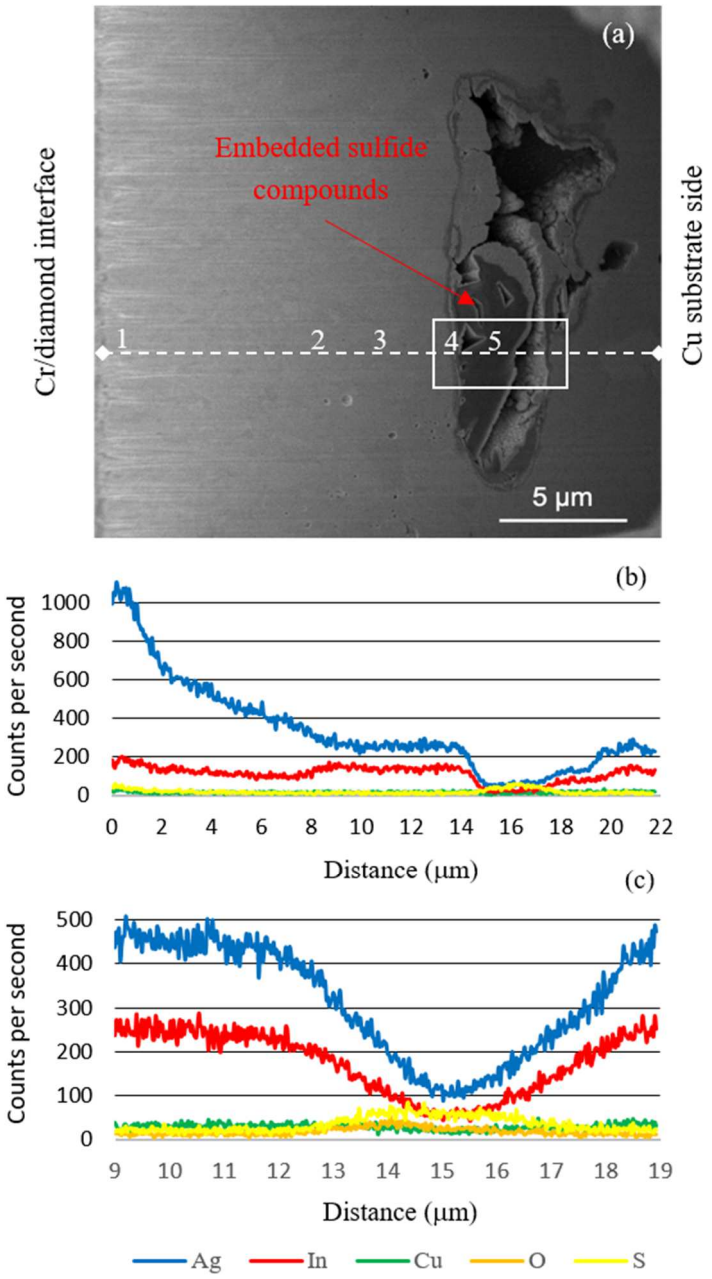

Figure 4.11 (a) The FIB sectioned view through intact joint at the fracture surface of Design III; (b) the EDX line scan for the line shown in (a); (c) the EDX line scan for the second phase within the labeled box in (a)

Table 4.3 The EDX quantitative analysis results for the points marked in figure 4.11 (a)

	1	2	3	4	5
Ag at.%	94.2	74.12	74.4	74.6	70.1
In at.%	5.1	21.1	21.2	17.4	16
Cu at.%	0.6	4.7	4.4	7.2	8.2
S at.%	–	–	–	0.7	5.5

As shown in figure 4.11 (b) and (c), an upsurge in S intensity occurs at the region of the embedded phase with a darker contrast. In the data collected in Table III, the concentration of In showed a normal gradient along the bonding joint. In the meantime, S concentration is considerably high at the points 4 and 5. According to the EDX data, it is believed that this embedded phase is a mixture of Ag and Cu sulfides. This is in agreement with the fact that S was detected on the surface of Ag after annealing in vacuum, as shown in the XPS spectrum previously. Therefore, it is safe to conclude that the Ag/In interface has the weakest interfacial strength in the design III, due to the formation of the embedded sulfide compounds.

4.3.3 Joint Shear Strength

In order to assess the mechanical adhesion of the joint, die shear tests were carried out on 4 samples for each design. Figure 4.12 shows the average shear strength and the variation range of the shear strength for each design. Design I exhibited the highest shear strength,

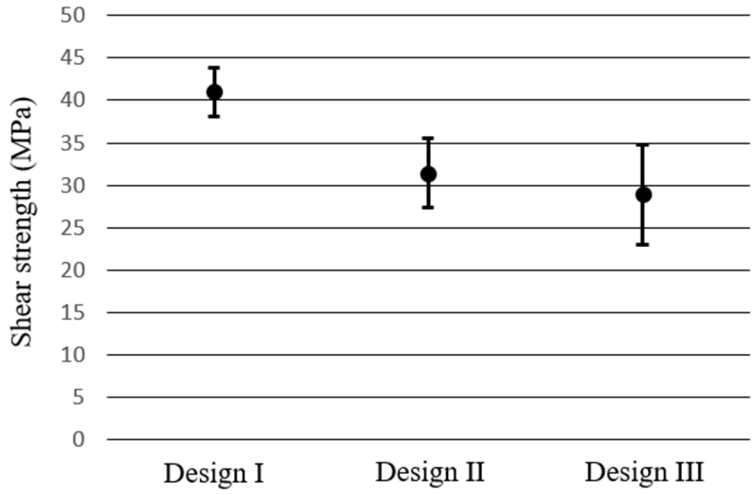

Figure 4.12 The shear strength values and the variation ranges of the silver–indium bonding structure with Design I, Design II, and Design III

showing a maximum value at 43 MPa and an average value of 41 MPa. The shear strength values were lower in design II and design III, with the average shear strength of 32 MPa and 29 MPa, respectively. The decreased strength in design II can be attributed to the formation of oxide layers within joint. For design III, the sulfide compound is believed to be the major cause for reduced shear strength. With the similar bonding conditions (temperature, pressure, time), the shear strength of silver nanoparticles sintered joints, which are widely used commercially in the high-power devices, usually are below 15 MPa [19]. Therefore, even with some extent of degraded mechanical strength, it is safe to claim that all of the three designs were mechanically robust for the diamond heat spreader heterogeneous integration with high-power devices. More detailed analysis of the microstructure-strength relation and the underlying reasons of the degradation will be provided in the following section.

4.4 Discussion

In general, the Ag-In bonding technique is a complicated dynamic physical-chemical process, in which the diffusion of various chemical species plays a dominating role at the different stages of the bonding process. The idea of controlling Ag grain size for the Ag-In bonding is stemmed from the fact that indium-to-silver diffusion process is dominated by the grain boundary (GB) diffusion mechanism [20]. The effective diffusivity (D_{eff}) of indium-to-silver diffusion process at the early stage can be approximately estimated by the grain boundary diffusivity (D_{gb}), as given in eq. (4.1):

$$D_{eff} \approx D_{gb} = D_{0gb} exp \frac{-Q_{gb}}{RT} \tag{4.1}$$

where D_{gb} is the pre-exponential factor of the grain boundary diffusion, and Q_{gb} is the activation energy of the predominant diffusion process through the grain boundary path. Typically, the grain boundary diffusivity is heavily correlated with the grain boundary density, which is inversely proportional to the average grain size [21]. In the indium-silver diffusion couple, with a silver grain size around 100 nm, the activation energy of the indium-to-silver grain boundary diffusion Q_{gb} has been recorded as 0.34 eV [20], which is much smaller than the activation energy of the lattice diffusion from silver-to-indium through the interstitial site with a value of 0.55 eV [22].

In the case of design I, as shown in figure 2 (a) and (b), the microstructure of as-deposited electroplated Ag layer is agglomerated dendritic flakes with nanocrystalline grains. As indium is further deposited onto the electroplated Ag layer, it would rapidly diffuse into the Ag layer, resulting in the fast formation of $AgIn_2$ IMC. During the temperature ramping stage of the bonding process, the consumption of indium and the further growth of the $AgIn_2$ and Ag_2In IMCs is accelerated at the elevated temperature, before reaching the melting temperature of indium and the generation of the liquid phase. The growth kinetics of $AgIn_2$ IMC is diffusional controlled, and the consumption rate of the indium is largely depending on the grain boundary diffusivity D_{gb} of the indium-to-silver diffusion process. Therefore, the microscopic structure of nanocrystalline electroplated Ag determines the fast consumption nature of indium, leading to the undersupply of molten phase during the bonding process. It would result in ineffective wetting of the Ag on diamond side and formation of voids at the initial bonding interface. As seen in figure 4(a) and figure 5(a), during the shear test, the cracks would initiate at those isolated voids under shear stress, leading to the fracture of the

bonding joint. In addition, it is not favorable to have those isolated voids in the bonding structure, in terms of optimizing the thermal dissipation performance of the CVD diamond.

In order to eliminate the isolated voids in the initial bonding interface, it is essential to control the diffusion kinetics of the bonding system. Enlarging the grain size of the silver layer, can effectively reduce the grain boundary density and the grain boundary diffusivity D_{gb}, thereby slowing down the consumption rate of indium before the generation of the molten phase. High temperature treatment of solid materials is one popular approach to increase the grain size through the bulk recrystallization mechanism. Specifically, the bulk transition of Ag occurs above its Tamann temperature ($T_t = 0.5T_m$) at 345℃ (618 K). Therefore, the annealing temperature at 350 ℃ (623 K) in the current study is suitable for the purpose of enlarging the Ag grain size. Typically, the bulk recrystallization and the growth of the grain size can be regarded as purely thermally induced effects.

However, as seen in the case of design II, it is clear that the morphological changes during the annealing process in air were not purely thermally induced, but also were associated with reaction induced restructuring. As shown in figure 4.6 (c) and (d), the air annealed Ag layer has been transformed to a porous structure, whereas this porous structure was not seen neither in design I, nor in design III. The major difference was caused by the presence of oxygen gas (O_2) in air during the annealing process. Silver is not prone to the chemical reaction with O_2 to form oxide compounds, and the most stable oxide of silver, Ag_2O, would thermally decompose at 200℃ (473 K). However, as the electroplated nanocrystalline Ag is annealed in air, the grain boundaries provide low resistance paths for O_2 diffusion into the silver bulk, leading to a significant oxygen dissolution within the bulk. Three different species

of oxygen are associated with the surface and subsurface regions of Ag, namely, adsorbed surface atomic oxygen (O_α), bulk-dissolved oxygen (O_β), and surface segregated oxygen group (O_γ) [16]. Adsorbed surface atomic oxygen O_α would completely cover the silver surface at low temperatures, but this monolayer no longer exists when temperature is raised to above 300°C (573 K) [23]. The diffusion of oxygen into Ag occurs mainly through the grain boundaries of Ag at lower temperatures while at higher temperatures, volume diffusion of O into Ag becomes active. The bulk-dissolved oxygen O_β can be both preserved at the octahedral interstitial sites of the Ag lattice and accumulate along the grain boundaries of silver. According to the thermal desorption spectrum (TDS) measurements, O_β starts its desorption at approximately 300°C (573 K) and shows a peak desorption at around 400 °C (673 K) after air treatment at 300°C (573K). Formation of the surface segregated oxygen group (O_γ) takes place at temperatures higher than 600°C (873 K), where bulk-dissolved oxygen segregates to the surface via interstitially diffusing through densely packed crystalline planes [16].

In the current study, the annealing process in air at 350°C (623 K) has promoted oxygen adsorption and dissolution into the Ag microstructure, i.e., O_β, the bulk-dissolved oxygen. The prior-to-bond annealing and bonding temperature are not high enough for any oxygen desorption processes to take place. Simultaneous to the adsorption and dissolution of oxygen into Ag, restructuring of Ag on the terminating surfaces and within the bulk is happening. This restructuring is made possible by mass transfer at high temperatures. Ag tends to rearrange its surface into a densely packed, low-indexed, e.g., (1 1 1) crystal plane, during the annealing process. This phenomenon is known as faceting, which is driven by the

tendency of lowering the overall free energy of the system. Generally, annealing results in the following three phenomena: (1) formation of low-index, densely packed atomic planes at the terminating surfaces, (2) annihilation of grain boundaries, and (3) growth of grains/crystallites with preferred densely packed crystallographic orientation. At the early stages of the annealing, the electroplated nanocrystalline silver has a strong oxygen dissolving capability due to its high grain boundary density. As the grain boundary density is significantly reduced during the annealing process, the silver microstructure becomes oversaturated with the previously dissolved O_β. It is possible that the dissolved oxygen could be accumulated at the boundaries and triple junctions between grains. This happens because the outwards diffusion capability of O_β into surrounding grains is limited by the formation of densely packed grains with low sticking coefficients for oxygen. Thus, the confinement of O_β at grain boundaries can contribute to the formation of porous Ag microstructure seen in figure 4.6 (c) and (d). Another reason for formation of voids at the grain boundaries is possibly the strain induced by the volume interstitial diffusion of O_β into the Ag unit cell. As the temperature is increased and grain boundary density is reduced, the interstitial volume diffusion of O becomes significant. The incorporation of oxygen into the silver requires anisotropic displacement of silver atoms and subsequently an increase in the Ag unit-cell lattice constant. This leads to increased stress between the neighboring grains. The accumulation of stress could possibly result in rupture and subsequent void formation in the grain boundaries. This cycle of void formation is accelerated as less grain boundary diffusion and more bulk diffusion takes place with the continuation of annealing [16]. All these can be

considered as the underlying reasons for the formation of the porous microstructure in the Ag layer after annealing in air, as seen in figure 4.6 (c) and (d).

When the In layer was electroplated on the air-annealed Ag layer, it would be in contact with the Ag layer abundant with O_β at its subsurface regions. Based on previous discussions, this oxygen species is distributed in the Ag grain boundaries and within the grains. Since the near-surface region of silver is mainly composed of close-packed crystal structures at elevated temperatures, desorption of bulk-dissolved oxygen to the surface would be hindered, thereby confining the oxygen groups in the near-surface regions of Ag. This microscopic process is schematically depicted in figure 4.13, and it has been reported by Nagy et al., through ion scattering spectroscopy (ISS) of silver doped with oxygen [16].

During the bonding process, besides the effect of grain size enlargement, the indium-to-silver through grain boundaries diffusion process could be further impeded by O_β accumulated

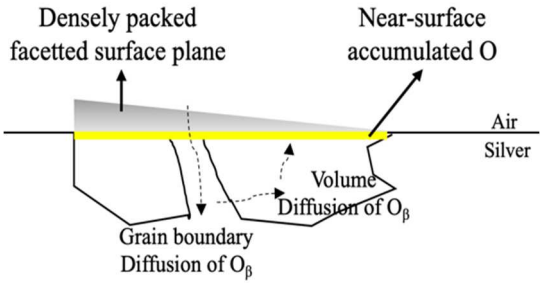

Figure 4.13 The schematic representation of the diffusional processes during prior-to-bond annealing of silver in air.

along the Ag grain boundaries. As demonstrated in figure 4.8 (a), the indium molten phase was largely preserved during the bonding process, indicating the indium-to-silver diffusion rate was effectively reduced. With the indium inwards diffusing flux, it interacts with O_β embedded in the Ag microstructure, leading to the nucleation and growth of In_2O_3 phase,

along the grain boundaries, within the Ag grains and most importantly in the near-surface regions, where outward diffusion of O to the surface is hindered due to presence of close-packed crystal structures. This partially explains the origin of the secondary phase with an elongated shape and the abnormal gradient of the In concentration, as labeled in Figure 4.9 (a) and recorded in Table 4.2, respectively. Moreover, as indicated in the XPS data, which was shown in figure 4.7, Cu from the substrate was able to penetrate through the entire Ag layer and reach to the top surface with the formation of CuO. Since CuO would not thermally decompose at the bonding temperature, the secondary phase can also be partially attributed to the CuO. Therefore, the oxidation induced morphological changes and the residue metallic oxides embedded in the bonding structure become the new pressing issues in the design II of the Ag-In bonding process.

In the case of design III, oxidation is no longer the issue as the annealing of Ag is carried out in the vacuum environment. However, as mentioned earlier, another issue of the metallic sulfide formation, embedded in the bonding structure, was identified to cause the degradation of the mechanical strength of the joint. Both Ag and Cu can be easily tarnished by the S element to form Ag_2S or Cu_2S [24]. The S source could be attributed to the sulfur-containing gas species (such as, H_2S, SO_2, and etc.) in the laboratory environment, and the In sulfamate bath (the indium electroplating bath) which contains indium sulfamate and sulfuric acid. As seen in the XPS survey spectrum, before In plating process, S elemental signal has already been detected from the top surface of the vacuum annealed sample. A good question to ask is why annealing in vacuum has made the Ag layer much more susceptible to the sulfurization process. It was observed that Cu reached to the top surface of silver after

the vacuum annealing, as shown in the XPS data of Figure 4.7. In the Table 4.3, it was recorded that Cu was distributed in the prior-to-bond annealed Ag layer and bonding joint structure, after the vacuum annealing and the bonding process. Therefore, the Ag layer has been effectively alloyed with Cu during the vacuum annealing process. It is well known that the resistance to sulfurization is significantly reduced when Ag is alloyed with Cu (sterling silver) [25], possibly due to the alternation of the Ag valence band structure [9]. In design II, the Ag layer has been also alloyed with Cu after being annealed in air. However, the diffused Cu has been partially oxidized into CuO, and the prior-to-bond Ag layer has been completely covered by the bulk-dissolved O_β at its surface and subsurface, rather than by the loosely adsorbed O_α. Therefore, the design II did not suffer from the sulfurization issue as seen in the design III.

Furthermore, in the literature [26], it is suggested that Ag does not tend to form a uniform film when it corrodes. As demonstrated [25, 26], the Ag_2S would nucleate in the form of isolated islands, and further grow into spikes or dendrites of the tarnished silver layers. This is in accordance with the current observed isolated sulfide compound, as shown in figure 4.11 (a). It is well known that sulfide compounds have extremely poor mechanical properties, so they would become the preferred path for the crack propagation upon shearing the joint, resulting in a degraded mechanical behavior in the design III.

Figure 4.14 shows the summary of microstructural evolutions at each stage for the case of design I, II and III, respectively, based on the findings and the underlying mechanism discussed above. Based on these findings, the prior-to-bond annealing process of Ag has successfully resolved the issue of the molten phase undersupply issue. However, it also led to undesirable consequences on the joint microstructure. The formation of the metallic oxide and metallic sulfide reduced the overall shear strength of the Ag-In bonding joint. The

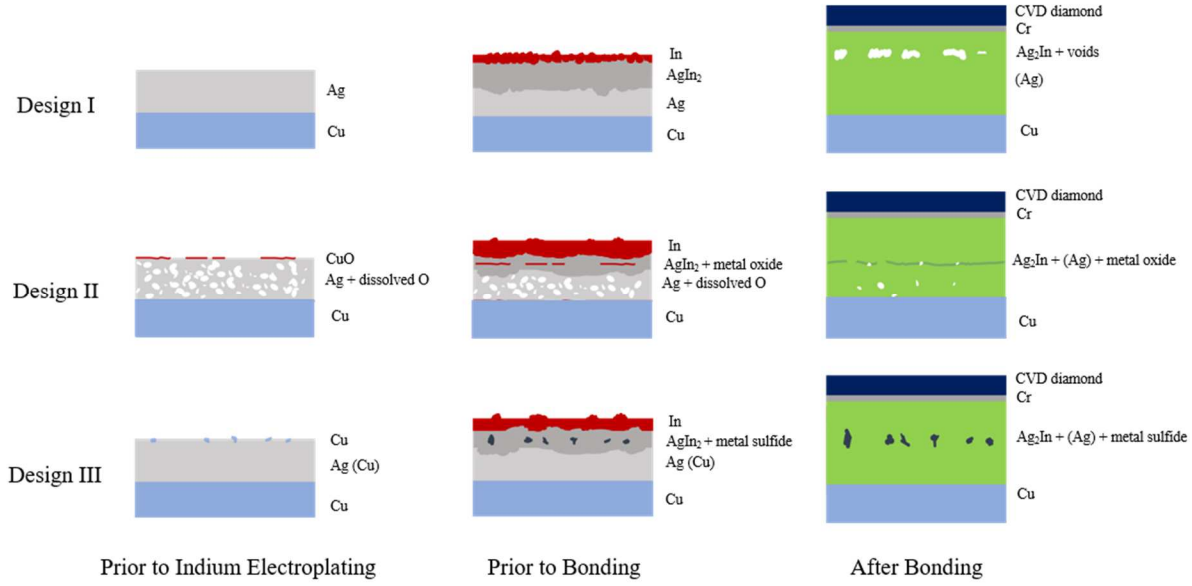

Figure 4.14 Schematic representation of microstructural evolutions for each design during pre-bond and bonding process

diffusion of oxygen and Cu in the prior-to-bond annealed Ag layer were the determining factors for the degradation of the joint.

4.5 Conclusion

In summary, the heterogeneous integration between CVD diamond and Cu substrate with the Ag-In bonding method has been demonstrated with thorough quantitative evaluations,

for utilization in the high-power electronics and photonics packaging technology. The issue of the undersupplied molten phase during bonding process has been successfully resolved by the introduction of the prior-to-bond silver annealing process. Within the current Ag-In bonding structure design scheme, some unexpected adverse effects of the prior-to-bond annealing process have been firstly discovered and systematically discussed in terms of the underlying failure mechanism. Prior-to-bond annealing of Ag in air and vacuum results in formation of metallic oxides and sulfides respectively. These compounds are embedded within the joint and deteriorate the shear strength of the joint. Scientifically, this study has advanced the understandings to the Ag-In bonding system with more detailed thermodynamic considerations, thereby providing a good reference guidance for the future design works. In principle, avoiding the oxidation issues in inert or reducing gas environment can properly resolve the reaction-induced porous structure due to the subsurface reconstruction. A proper design of a diffusion barrier between Ag layer and Cu substrate might be considered to solve the sulfurization issue due to the interdiffusion between Ag and Cu. In the future works, those considerations will be further implemented in the Ag-In bonding design, in order to improve the thermal interface, the joint shear strength and the long-term reliability.

References

1. A. L. Moore and L. Shi, “Emerging challenges and materials for thermal management of electronics,” Materials Today, vol. 17, No. 4, pp. 163–174, 2014.
2. S. Weiss,E. Zakel, and H. Reichl, “Mounting of high power laser diodes on diamond heatsinks,” IEEE Transactions on Components, Packaging, and Manufacturing Technology: Part A, vol. 19, No. 1, pp. 46-53, 1996.
3. K. Yoshida and H. Morigami, “Thermal properties of diamond/copper composite material,” Microelectronics Reliability, vol. 44, No. 2, pp. 303–308, 2004.
4. C. C. Lee, C. Y. Wang, and G. S. Matijasevic, “A New Bonding Technology Using Gold and Tin Multilayer Composite Structures,” IEEE Trans. Components, Hybrids, Manuf. Technol., vol. 14, No. 2, pp. 407–412, 1991.
5. R. W. Chuang and C. C. Lee, “Silver-indium joints produced at low temperature for high temperature devices,” in IEEE Transactions on Components and Packaging Technologies, 2002, vol. 25, No. 3, pp. 453–458.
6. Y. Y. Wu and C. C. Lee, “The strength of high-temperature Ag-In joints produced between copper by fluxless low-temperature processes,” J. Electron. Packag. Trans. ASME, vol. 136, No. 1, 2014.
7. Y. Y. Wu and C. C. Lee, “Bonding silicon chips to aluminum substrates using Ag–In system without flux”, IEEE Transactions on Components, Packaging and Manufacturing Technology, vol. 3, No. 5, pp. 711-715, 2013.
8. Y. Huo and C. C. Lee. “The growth and stress vs. strain characterization of the silver solid solution phase with indium,” Journal of Alloys and Compounds, vol. 661, pp. 372-379,

2016.

9. Y. Huo, J. Wu, and C. C. Lee. “Study of Anti-tarnishing Mechanism in Ag-In Binary System by Using Semi-Quantum-Mechanical Approach,” Journal of Electrochemical Society, vol. 164, No. 7, pp. C418-C427, 2017.
10. Y. Y. Wu, W. P. Lin, and C. C. Lee, “A study of chemical reactions of silver and indium at 180 °C,” J. Mater. Sci. Mater. Electron., vol. 23, no. 12, pp. 2235–2244, 2012.
11. P. J. Wang, C. H. Sha, and C. C. Lee, “Silver microstructure control for fluxless bonding success using Ag-In system,” IEEE Trans. Components Packag. Technol., vol. 33, no. 2, pp. 462–469, 2010.
12. R. Sheikhi, Y. Huo and C. C. Lee. “Fluxless Bonding Technique of Diamond to Copper using Silver-Indium Multilayer Structure,” Electronic Components and Technology Conference (ECTC), 2019 IEEE 69th. IEEE, pp. 150-156, 2019.
13. A. Katz, C. H. Lee, and K. L. Tai, “Advanced metallization schemes for bonding of InP-based laser devices to CVD-diamond heatsinks,” Materials Chemistry and Physics, vol. 37, no. 4. pp. 303–328, 1994.
14. D. Doneddu, O. J. Guy, P. R. Dunstan, T. G. G. Maffeis, K. S. Teng, S. P. Wilks, P. Igic, D. Twitchen, and R. M. Clement, “X-ray photoelectron spectroscopy studies on the formation of chromium contacts to single-crystal CVD diamond,” Surface Science, vol. 602, No. 6, pp. 1135-1140, 2008.
15. C. C. Lee, D. T. Wang, and W. S. Choi, “Design and construction of a compact vacuum furnace for scientific research,” Rev. Sci. Instrum., vol. 77, no. 12, p. 125104, Dec. 2006.
16. A. J. Nagy, G. Mestl, D. Herein, G. Weinberg, E. Kitzelmann, and R. Schlögl, “The correlation

of subsurface oxygen diffusion with variations of silver morphology in the silver-oxygen system," J. Catal., vol. 182, no. 2, pp. 417–429, 1999.

17. J. F. Moulder, W. F. Stickle, P. E. Sobol, and K. D. Bomben, Handbook of X-ray Photoelectron Spectroscopy, Physical Electronics USA Inc., Chanhassen, 1995.
18. M. C. Biesinger, "Advanced analysis of copper X-ray photoelectron spectra," Surf. Interface Anal., vol. 49, no. 13, pp. 1325–1334, Dec. 2017.
19. P. Peng, A. Hu, A. P. Gerlich, G. Zou, L. Liu, and Y. N. Zhou, "Joining of silver nanomaterials at low temperatures: processes, properties, and applications," ACS Applied Materials & Interfaces, vol. 7, No. 23, pp. 12597-12618, 2015.
20. R. Roy, and S. K. Sen, "The kinetics of formation of intermetallics in Ag/In thin film couples," Thin Solid Films, vol. 197, No. 1, pp. 303-318, 1991.
21. A. Oudriss, J. Creus, J. Bouhattate, E. Conforto, C. Berziou, C. Savall, and X. Feaugas, "Grain size and grain-boundary effects on diffusion and trapping of hydrogen in pure nickel," Acta Materialia, vol. 60, No. 19, pp. 6814-6828, 2012.
22. T. Anthony, and D. Turnbull, "Interstitial diffusion of gold and silver in indium," Physical Review, vol. 151, No. 2, pp. 495-498, 1966.
23. C. T. Campbell, "Atomic and molecular oxygen adsorption on Ag (111)," Surface Science, vol. 157, No. 1, pp. 43-60, 1985.
24. R. Roy and S. K. Sen, "The study of diffusion of copper in thin films of silver and AgAl alloys as a function of increasing aluminium concentration," Thin Solid Films, vol. 223, No. 1, pp. 189-195, Jan. 1993.
25. Y. Huo, S. W. Fu, Y. L. Chen, and C. C. Lee, "A reaction study of sulfur vapor with silver and

silver–indium solid solution as a tarnishing test method," Journal of Materials Science: Materials in Electronics, vol. 27, No. 10, pp. 10382-10392, 2016.

26. T. E. Graedel, "Corrosion Mechanisms for Silver Exposed to the Atmosphere Environmental Interactions with Silver Surfaces," Journal of the Electrochemical Society, vol. 139. No. 7, pp. 1963-1970, 1992.

Chapter 5

Nano-silver sintering for high power LED die attach

5.1 Introduction

light emitting diodes (LEDs) are now being used for a variety of applications including displays, signs and lightning. This technology has gained enormous attention due to its excellent properties of long lifetime, low power consumption and low cost. The light extraction efficiency of LEDs has increased significantly over the past few decades while the cost of production has been declining continuously. The global LED lighting market size was valued at USD 54.00 billion in 2019 and is projected to expand at a compound annual growth rate (CAGR) of 13.4% from 2020 to 2027 [1]. Figure 5.1 shows the current LED market size and its expected growth in the coming years. In the chip-level, many improvements have

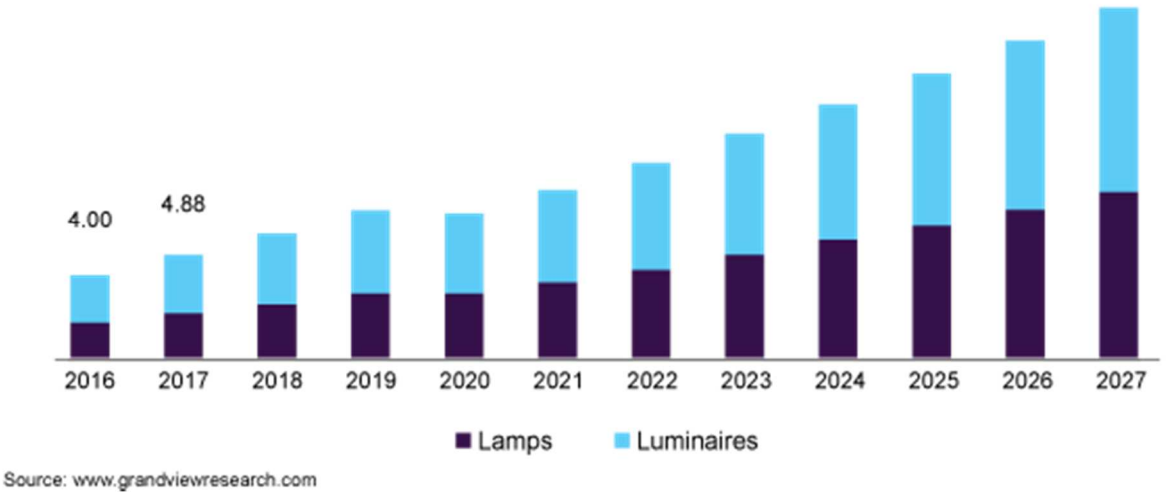

Figure 5.1 US.LED lighting market size, by product, 2016-2027 (USD Billion)

been implemented that has resulted in significant gains in the efficiency and low cost manufacturing of LEDs [2] [3].

The efficiency of light extraction is also greatly affected by the packaging materials and technologies used. Under ideal conditions, in active layer of the LED die, all the electron-hole pairs should combine, and all input power should be converted into optical power. However, in practice, some electrical power is converted into thermal energy. As the LED operates, electrons combine either radiatively or non-radiatively with holes as they are injected into the active region. The radiative recombination will emit photons. However, nonradiative recombination processes within the active layer can result in heat generation. Moreover, Joule heating at the series resistance of the diode and at the interconnect can also contribute to heat generation. At the same time, the light absorption in different materials and interfaces are also sources for heat generation [4][5]. Approximately 15–30% of input power turns into visible light and the rest is dissipated in the form of heat. The increase in junction temperature of LED chips will also result in reduction of output power, forward voltage and mean time of failure, additionally shifting of the output wavelength can occur [6]. Hence in order to increase efficiency and reliability of LEDs, incorporating materials and designs that increase heat dissipation in the package is extremely critical.

In addition to providing high thermal conductivity, the package also protects the LED chip from environmental effects such as electrostatic discharge, moisture, high temperature, shock impact and etc. [7]. Another point to be considered when selecting materials for packaging of LED chips is the coefficient of thermal expansion (CTE) of different components. Since the LED package comprises of various materials that have different CTE, with

increasing temperature, each material will deform at a different rate. This phenomenon can induce stresses within the LED die and LED package. Best practice is to use low temperatures during package fabrication to avoid such thermo-mechanical stresses.

In this chapter, a newly developed nano silver die attach system is introduced. The developed bonding technology forms very thin (~5μm) joints between high power blue LED chips and substrates at relatively low temperatures (200°C). This technique results in LED packages with superior optical and thermal performance compared to commercially available LED packages that utilize Ag epoxy as the die attach system.

5.1.1 LED structure

In order to better understand the package structure, it is necessary to review existing commercially available LED structures. Figure 5.2 shows the three different designs commonly used. These three types of LED chips are (a) lateral (horizontal), (b) vertical and (c) flip-chip (FC) [7].

The conventional lateral type of LED consists of sapphire substrate, GaN buffer layer, n-GaN layer, p-GaN layer, electrodes and active layer. Inside the active layer multi-quantum well (MQW) lead to electron-hole combination and light emission. GaN-based LED is most popular LED which is grown on the sapphire (Al_2O_3). The light efficiency of lateral structure is not high, function needs high forward voltage, and heat dissipation in the chip is poor due to the low thermal conductivity of sapphire substrate.

LEDs with vertical structure has been introduced recently to address the aforementioned shortcomings. In the vertical design the electrodes are placed on the top and bottom of LED

chips. Vertical LED could grow on thermal/electrically conductive substrate such as silicon, silicon carbon and metal alloys. Compared to the conventional lateral LEDs, the vertical LEDs possess uniform current spreading, smaller thermal resistance and smaller series electrical resistance.

The third type of LED structure is flip-chip (FC), in this configuration LED dies are flipped and bonded onto the substrate by metal bump or a uniform bonding layer. In the FC design, the sapphire layer with low thermal conductivity is not within the heat dissipation path and generated heat can flow downward through the thinner epitaxial material, solder/bonding later and substrate; accordingly, thermal performance of this structure is considerably improved, and thus high-power operation can be achieved with this configuration. A drawback in the manufacturing and packaging process of these structures is the precision alignment needed for bonding metals pads onto the substrate.

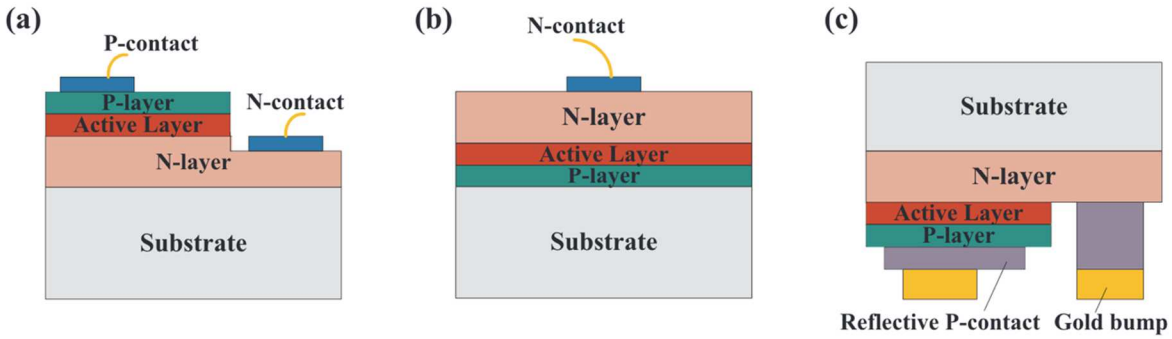

Figure 5.2 Three common types of high-power LED structure: (a) lateral (horizontal), (b) vertical and (c) flip-chip (FC) LED

5.1.2 Die attach for FC LED packaging

The die attach material has become a bottleneck for effective heat dissipation away from the active region of the LED chip. A good die attach material should have excellent adhesion to

the metallization on the chip and the substrate, provide stress relief and high thermal conductivity while having the capability of fabrication at low temperatures. Also, the occurrence of voiding in the die attach layer can result in increased junction temperature and hot spot formation which are undesirable [8]. In the following paragraphs a brief overview of existing die attach material systems for high and medium power LEDs is provided.

Die attach materials can be either organic or inorganic-based. Each of them can provide certain type of advantages and disadvantages and are chosen based on the specific applications. The organic die attach materials are suspensions of conductive metallic particles in a polymer matrix. Among them, Silver epoxy is most popular die attach material in conventional LED packages, but it suffers from low thermal conductivity and thus output power can be limited. However, Ag epoxies also known as electrically conductive adhesives (ECA) provide very low cost processing. For high power LEDs there has been enormous interest in substituting these materials with highly conductive materials. Eutectic gold-tin (Au80Sn20) bonding and SnAgCu (SAC) solder joints are preferable candidates. Eutectic gold-tin was extensively discussed in chapter 2. It has high thermal conductivity, excellent mechanical properties and electrical conductivity and also provides secondary reflow compatibility. It is used either as a pre-coated layer on LED backside, a preform or in form of solder paste.

The high bonding temperature (range from 300°C to 320°C) for AuSn can cause oxidation of substrate materials, thermal damage to the chips and possibly delamination in the epitaxial layers of the LED. Also, high cost of gold should be considered as a drawback for this system.

Table 5.1 Thermal resistance of common die attach materials for LED packaging

Die attach material	Au80Sn20	Sn96.5Ag3Cu0.5	Silver epoxy
Transient thermal resistance (K/W)	2.5	3.2	4

SAC solders are also a compelling candidate since they provide lower bonding temperature at 250°C and lower cost (compared to eutectic gold-tin). Table 5.1 provides the transient thermal resistance values for each of these material solutions [8].

5.1.3 Nano-silver sintering for LED die attach

Materials with small dimensions can be exploited in die attach applications. Metallic nanoparticles such as gold, silver and copper possess unique physical properties that are different from their bulk state and have the potential to be incorporated for sintered joints either purely or as fillers in a carrier. Copper nano-particles has for instance has attracted significant attention because of their excellent electrical and thermal conductivity, however copper oxidation at high temperatures still remains as a major challenge [9]. This chapter evolves around nano silver sintering; thus, it is beneficiary to cover the mechanism and driving force for sintering of silver nanoparticles.

5.1.3.1 Sintering mechanism

In the context of silver sintering for die attach applications, sintering is thought of as densification of nanoparticles by means of solid state diffusion. The sintering process can be divided into three stages, initial stage, intermediate, and final stage. These stages are overlapped during the actual sintering process and usually no distinct difference in term of

occurrence can be made between them. In the first stage, particles are rearranged into more stable positions by rotating and sliding in response to the sintering forces. This contributes to shrinkage and an overall increase in density. This rearrangement stage increases the contact area between neighboring particles, enabling the formation of necks between particles. Neck formation and growth can take place by diffusion, vapor transport, plastic flow, or viscous flow. The initial stage lasts until a neck radius of around 0.4 to 0.5 of the particle's radius is achieved. The intermediate stage begins when the pores have attained their equilibrium shapes as dictated by surface and interfacial energies. At this point, the pores are still continuous or interconnected. Densification takes place by the reduction in cross section of the pores. Eventually, pores become unstable and are cut off from each other, leading to the final stage of sintering. Of the three stages, the intermediate stage covers the majority of the sintering process. In the final stage covers the isolated pores are eliminated until the theoretical density is reached. This stage is also characterized by grain growth in which the larger grains tend to increase in size at the expense of the smaller grains.

The driving force for the sintering and densification is the tendency of material to reduce it free energy. This happens by material transport from regions of high energy to regions of lower energy. Surfaces, interfaces and grain boundaries are inherently high energy regions due to randomness and broken bonds in these regions. By eliminating or minimizing these surfaces the overall free energy of the material is reduced.

Assuming that particles have spherical shape, the same size and are uniformly packed, a simple model for sintering can be considered. This simple geometrical model is shown in Figure 5.3. The sintering phenomenon in polycrystalline materials is rather complex. The

sintering of polycrystalline solids is dependent on the microstructure of the powder system. Thus, simplifications in the models make the corresponding sintering equations rather approximations and tend to be useful in making qualitative descriptions and comparative analysis. Sintering occurs to lower the overall free energy of the system. The sintering equations for different sintering mechanisms can be generally expressed as eq (5.1):

$$(x/r)^n = Bt \tag{5.1}$$

where x/r is ratio of the neck radius to the particle radius. B is a constant which depends on the particle size, temperature, and geometry. t is the sintering time and n is a mechanism-characteristic exponent that depends on the mass transport mechanism responsilble for sintering (viscous flow: n = 2; volume diffusion: n = 4–5; grain boundary diffusion: n = 6; surface diffusion: n = 7). Since exponent n is dependent on the sintering mechanism, the measurement of n may provide information on the dominant sintering mechanism. In general, it is well established that as sintering temperature increases, the mechanism for sintering moves away from surface diffusion towards volume diffusion [10][11].

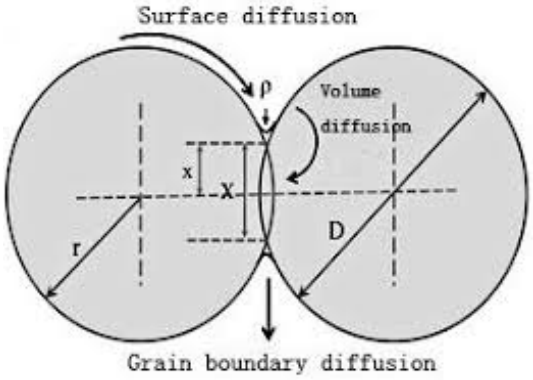

Figure 5.3 Geometric representation of simplified model used for determining sintering mechanism

5.1.3.2 Challenges in sintering of nano-silver

Compared with conventional microscale materials, nanoscale materials have significantly high values of surface energy. Nanoscale materials typically agglomerate and aggregate more easily due to their very fine particle sizes. Due to weak forces such as Van der Waals/electrostatic forces, particles can form agglomerates, while aggregation is a procedure in which the material is bonded together by solid necks of significant strength such as metallic force prior to actual sintering process. Agglomerate can usually be re-dispersed by external forces such as mechanical or ultrasonic energy, but the aggregate cannot.

These phenomena result in inhomogeneous distribution of particles and thus will reduce the capability of reaching high levels of densification. Another challenge for nanomaterial sintering is the non-densifying diffusions at low temperatures. Volume diffusion can produce densification while surface diffusion will only cause particle necking and coarsening rather than meaningful densification.

At low temperatures, the sintering process is controlled by surface diffusions and results in neck formation between particles but little actual densification while at higher temperatures, grain boundary and volume diffusions dominate the sintering process, leading to densification. If a non-densifying diffusion is allowed to proceed excessively, it will exhaust the driving force that is needed for a densifying process to, making the sintering and achieving high densifications rather difficult. An approach to minimize non-densification diffusions is to use fast heating rated to bypass the low-temperature portion of sintering quickly [12].

5.1.3.3 Synthesis of silver nanoparticles

Silver nanoparticles can be formed either through physical or chemical methods. Physical approaches include evaporation-condensation and laser ablation. The absence of solvent contamination in the prepared thin films and the uniformity of NPs distribution are the advantages of physical synthesis methods in comparison with chemical processes. However, these processes are rather complex and expensive. For electronics packaging applications, chemical methods are usually used for the preparation of nanoparticles. Thus, here a brief overview of the information regarding these chemical methods is provided.

In chemical methods, different reducing agents are used for reduction of silver ions (Ag+) in aqueous or non-aqueous solutions. These agents reduce Ag^{+} resulting in the formation of metallic silver (Ag^{0}), which is proceeded by agglomeration into clusters. These atomic clusters eventually lead to the formation of metallic colloidal silver nanoparticles. This process is schematical shown in figure 5.4.

Silver acetate, Silver Nitrate, Silver Chloride, or Silver Ammonia Solution are common silver salts that are used sources for silver ions. Ascorbic Acid, Monohydrate Hydrazine, Sodium

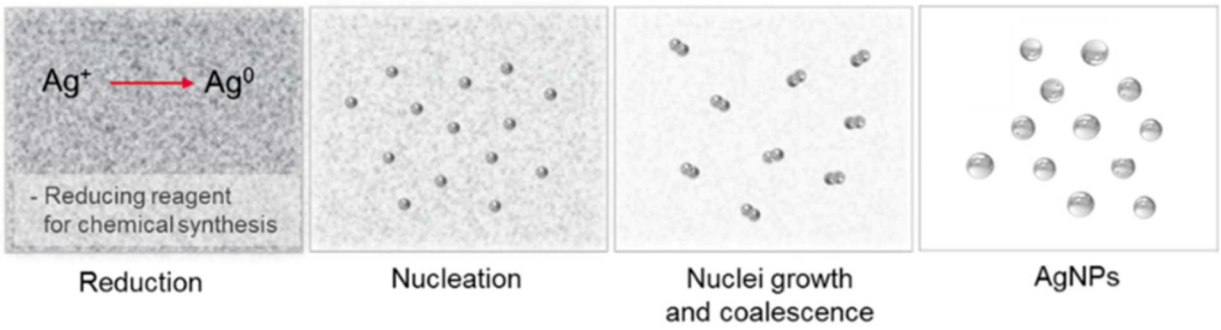

Figure 5.4 Schematic illustration of steps leading to formation of silver nanoparticles using chemical methods

Citrate, Dehydrate Sodium Citrate, Polyvinyl Pyrrolidone are common reducing agents. The chemical reduction reaction will occur in a solvent such as Ethanol, Methanol or Tetrahydrofuran [13][14].

It should be noted that the organic solvent and capping agents should be removed completely before reaching the sintering temperature. This is a bottleneck in achieving low temperature sintering of nanoparticle solutions. The currently available nano-silver pastes usually require temperatures in excess of 200°C for sintering. The novel formulation used in the current study has enabled a lower sintering temperature of 200°C which is extremely desirable since it will minimize the thermomechanical stresses induced in different components of the package.

5.2 Results

5.2.1 Synthesis of Ag Np suspension

Silver acetate (CH_3CO_2Ag) was used as the precursor for Ag ions and 3-Methoxypropylamine ($C_4H_{11}NO$) was used as the solvent. 3-Methoxypropylamine also acts as the capping agent this system where it mitigates nanoparticle agglomeration. Formic acid (CH_2O_2) is the reducing agent in the system. Silver acetate, 3-Methoxypropylamine and Formic acid are mixed in molar ratios of [0.01 : 0.001 : 0.0068]. Initially silver acetate and solvent are mixed with vigorous stirring. Then reducing agent is added. The reducing chemical reaction is an exothermic process that generates significant heat. The generated heat can degrade the nanoparticles through formation of agglomerates and partial sintering. To avoid this, formic acid was added incrementally to the solution while being placed in an

ice bath. Hence the reaction temperature was controlled and maintained bellow 35°C. Throughout the process, the solution was stirred aggressively to avoid any agglomeration. The final product is dark brown suspension that contains silver nanoparticles.

Produced suspension was then applied onto a glass slide and dried to remove the solvent and expose the nanoparticles. High resolution SEM image of the nanoparticle after drying at 60°C

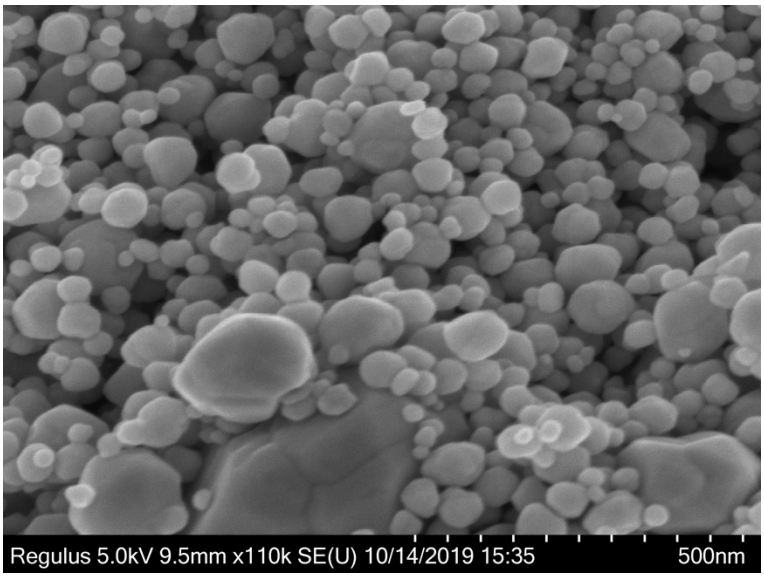

Figure 5.5 silver nanoparticles after drying the prepared suspension at 60°C for 3 hours

for 3 hours is shown in figure 5.5. The low drying temperature was selected in order to avoid any sintering. As seen in figure 5.5, the nanoparticles are not uniform in size. AgNp with size ranging from 25 nm up to 300 nm is observed after drying. Also, it can be observed that necking and agglomeration of nanoparticles has already occurred to a very limited extent. This can be due to lack of effective mixing or excessive heating during preparation of nanoparticles.

5.2.2 Microstructure of sintered of AgNp

Figure 5.6 shows the microstructure of AgNp after sintering at 200°C for 1 hour in vacuum. Here the AgNp solution was applied onto a glass slide by stencil printing and was sintered afterwards. The pressure applied during printing was minimal and just enough to obtain a uniform thickness of the film after printing. It is obvious that almost full sintering can be achieved through this temperature profile.

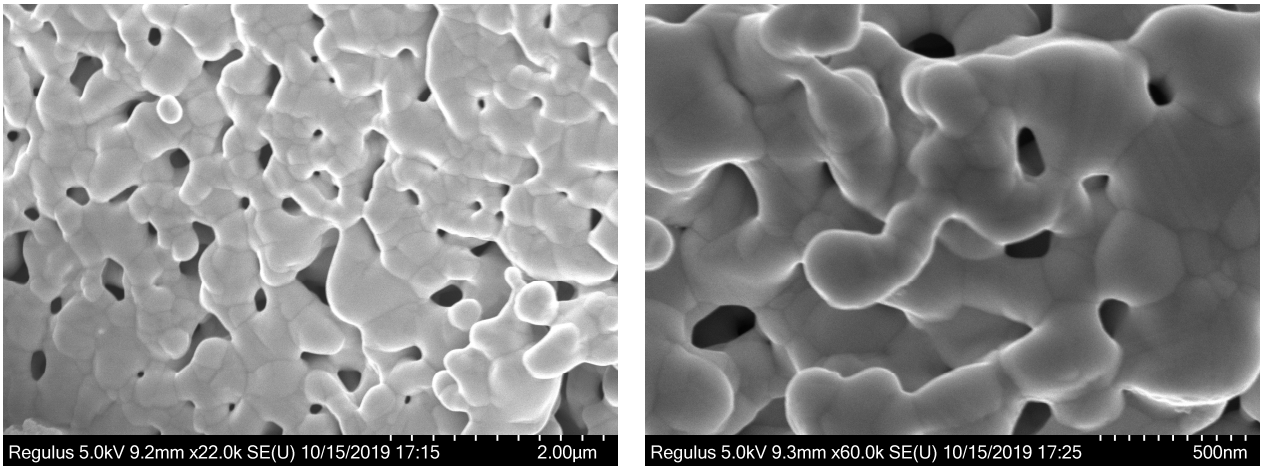

Figure 5.6 AgNp screen printed onto glass slide and sintered at 200°C for 1 hour in vacuum. (left) low magnification (right) higher magnification

5.2.3 Electrical resistivity of AgNp

Resistivity of the sintered AgNp was determined using the four-point probe technique. A thin film of AgNp was screen printed on to a glass slide. Strips of scotch tape were used as pacers for this purpose. Measurements were made after sintering the AgNp at 200°C for 1 hour in vacuum. The resistivity was determined using the following equation:

$$\rho = 2\pi a s \, {}^{V}/_{I} \quad (5.2)$$

Where a is the correction factor based on the configurations [15], s is the spacing, V is the voltage and I is the current.

In the four-point probe test, four probes are placed onto the film to be measured, by passing a current through two outer probes and measuring the voltage through the inner probes, the film's resistivity can be measured. Four-probe configuration eliminates measurement error due to the contact resistance between the probe and sample.

Table 5.2 lists the measured resistivity of sintered AgNp along with commercially available eutectic gold-tin and silver epoxy paste. The electrical resistivity data for bulk silver is also provided for the purpose of comparison. The resistivity of newly developed AgNp is higher than eutectic gold-tin and lower than Ag epoxy. This is rather expected, due to the porous microstructure of sintered AgNp.

Table 5.2 Electrical resistivity of newly developed AgNp compared with common die attach materials

	AgNp	Eutectic gold-tin	Silver epoxy	Silver
Electrical resistivity (Ω.m)	29.6×10^{-8}	16.4×10^{-8}	35×10^{-8}	1.6×10^{-8}

5.2.4 LED bonding process

In this study pin transfer was utilized in order to apply the AgNp solution onto the bonding surface. Pin transfer consists of using a pin to stamp the bonding material off a reservoir and on to the substrate. The die is then aligned and placed on the substrate using the die bonder (Mech-EI manual die bonder), pressure is applied to ensure uniformity of the BLT and then sintering takes place at 36 mtorr vacuum and 200°C for 1 hour. During the bonding, static

pressure of 1.37 Mpa is applied onto the assembly. Pin transfer is a very simple process that can provide high throughput production at very low cost. It can also guarantees a thinner BLT compared to conventional stencil printing techniques. Both the substrate and LED die (purchase from Lumileds) are commercially available items. The composition of metal pads on the LED die is a layer of Ti/Ni/Au deposited on the p- and n-GaN, and the composition of metal pads on the substrate is Ag-plated Cu. The high-power LED die is of flip-chip type with the size of 1×1 mm^2 and a forward voltage of 3.0 V. Its specified maximum operating DC current is 700 mA with an emission peak at 455 nm. After bonding, the die is encapsulated by a commercially available encapsulant, which is cured at 150℃ for 2 hr. Then, the encapsulated die is soldered to an Al-based printed circuit board. Following these steps the lumen output is evaluated and SEM-FIB is used to expose the microstructure of the joint.

5.2.5 Optical performance of LED

After assembling the package on the PCB. the LabSphere integrating sphere was used to evaluate the lumen output of the LED. Similar LED dies were also bonded with eutectic gold-tin and Ag epoxy to compare the optical performance of newly developed AgNp with the conventional die attach systems. Figure 5.7 shows the normalized lumen output for the three material systems.

The eutectic gold-tin hast the highest lumen output while, AgNp's ouput is approximately 3% lower. Interestingly, the lumen output for AgNp is 6.5% higher than that of Ag epoxy. It should be noted that the BLT for gold-tin and Ag epoxy are 25 and 20 μm respectively. Thus, the lower value of BLT for AgNp compared to Ag epoxy has caused this enhancement, while

the porosity of the AgNp joint does not make up for the thinner BLT while comparing with eutectic gold-tin bonds. For each case, 15 test vehicles were built and corresponding lumen output was measured.

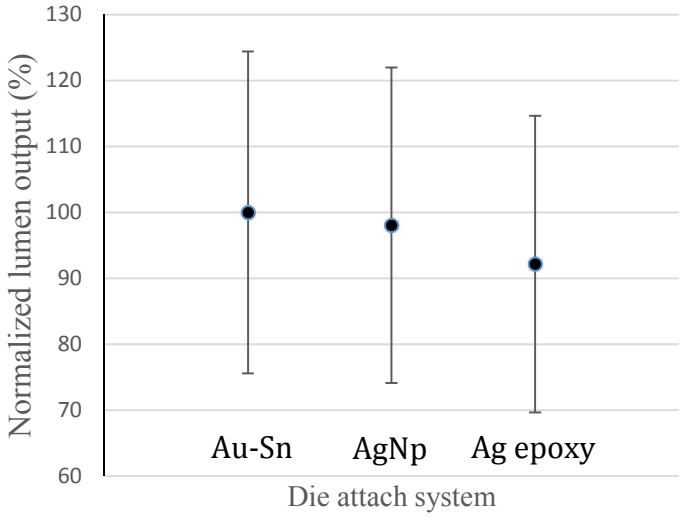

Figure 5.7 Normalized lumen output of LEDs packaged with different die attach materials.

5.2.6 Microstructure of the joint

Conventional cross-sectioning and polishing of the joint area was shown not be possible due to the smearing effects and differences in hardness of multi-layer materials that resulted in steps in the joint area. Thus, after sectioning and initial polishing, SEM-FIB was used to cut trenches perpendicular to the bond line, in order to expose the bonding AgNp layer. According to figure 5.8, the nanoparticles are sintered and have jointed the bonding pads on both the die and substrate. A significant amount of sintering is also observed between the AgNp and the silver finishing layer on the substrate bond pad. This indicates that this

sintering temperature is sufficient for achieve sintering between metallization layer and AgNp. On the die side where the bond pad is gold, there is also good adhesion and joining happening between sintered silver and gold.

The BLT is below 5 μm, which ensures high rates of heat dissipation away from the die. However, the porosity is a drawback in terms of thermal conductivity. The voids are pockets of air or possible solvent residue, with high dielectric constants. Thus, the porosity is detrimental to the heat dissipation capability of the dia attach. However, the lumen output measurements have indicated that still with the voiding this AgNp bonding system has superior performance compared to Ag epoxy. This enhancement can be attributed to the very thin BLT achieved through this method.

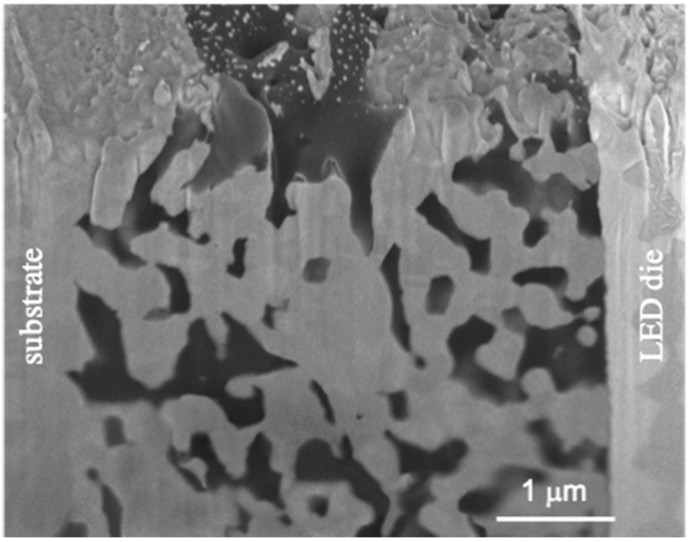

Figure 5.8 SEM image of cross section of the joint made with AgNp suspension. The cross section is prepared by FIB.

5.3 Conclusion

A new die attach technique for high-power LEDs using a novel silver nanoparticle suspension is proposed. The AgNp suspension can be applied onto the bonding surface using pin transfer. This technique results in joints with thickness of below 5μm which enhances the optical and thermal performance of the LED compared to commercially available Ag epoxy pastes that have BLTs in the range of 25 μm. Optical output data indicates performance slightly inferior to eutectic gold-tin bonding, however author believes that the simple and low cost nature of this technique can be a strong incentive for replacing conventional gold-tin bonding with the proposed technology. Preliminary results indicate the potential for use of this technique in mass production. Complementary studies on the thermal behavior and longtime reliability of this die attach system are strongly suggested. Obtaining this information will paint a better picture of the performance capabilities and possible drawbacks of this die attach system and can pave the way for use of this system for high throughput production.

References

[1] "LED Lighting Market Size & Share | Industry Report, 2020-2027." [Online]. Available: https://www.grandviewresearch.com/industry-analysis/led-lighting-market. [Accessed: 19-Feb-2021].

[2] J. Piprek, "Efficiency droop in nitride-based light-emitting diodes," *Phys. status solidi*, vol. 207, no. 10, pp. 2217–2225, Oct. 2010.

[3] N. F. Gardner *et al.*, "Blue-emitting InGaN-GaN double-heterostructure light-emitting diodes reaching maximum quantum efficiency above 200 A cm2," *Appl. Phys. Lett.*, vol. 91, no. 24, p. 243506, Dec. 2007.

[4] S. Kyatam, P. Camacho, L. Rodrigues, L. N. Alves, J. C. Mendes, and M. C. Figueiredo, "Thermal analysis of high power LEDs using different PCB materials," in *2017 European Conference on Circuit Theory and Design, ECCTD 2017*, 2017.

[5] C. Lasance and A. Poppe, *Thermal management for LED applications*. 2014.

[6] X. Tong, *Advanced materials for thermal management of electronic packaging*. 2011.

[7] M. Hamidnia, Y. Luo, and X. D. Wang, "Application of micro/nano technology for thermal management of high power LED packaging – A review," *Applied Thermal Engineering*, vol. 145. Elsevier Ltd, pp. 637–651, 25-Dec-2018.

[8] L. Yin *et al.*, "Effects of die-attach materials on the optical durability and thermal performances of HP-LED," in *ICEPT-HDP 2011 Proceedings - 2011 International Conference on Electronic Packaging Technology and High Density Packaging*, 2011, pp. 1116–1119.

[9] B. H. Lee, M. Z. Ng, A. A. Zinn, and C. L. Gan, "Application of copper nanoparticles as die attachment for high power LED," in *Proceedings of the Electronic Packaging Technology Conference, EPTC*, 2016, vol. 2016-Febru.

[10] J. K. Mackenzie and R. Shuttleworth, "A phenomenological theory of sintering," *Proc. Phys. Soc. Sect. B*, vol. 62, no. 12, pp. 833–852, Dec. 1949.

[11] J. D. Hansen, R. P. Rusin, M.-H. Teng, and D. L. Johnson, "Combined-Stage Sintering Model," *J. Am. Ceram. Soc.*, vol. 75, no. 5, pp. 1129–1135, May 1992.

[12] J. Yan *et al.*, "Sintering mechanisms and mechanical properties of joints bonded using silver nanoparticles for electronic packaging applications," *Weld. World*, vol. 59, no. 3, pp. 427–432, Apr. 2015.

[13] S. H. Lee and B. H. Jun, "Silver nanoparticles: Synthesis and application for nanomedicine," *International Journal of Molecular Sciences*, vol. 20, no. 4. MDPI AG, p. 865, 02-Feb-2019.

[14] K. Sweatman, T. Nishimura, and T. Komatsu, "A NANO SILVER REPLACEMENT FOR HIGH LEAD SOLDERS IN SEMICONDUCTOR JUNCTIONS."

[15] L. B. Valdes, "Resistivity Measurements on Germanium for Transistors," *Proc. IRE*, vol. 42, no. 2, pp. 420–427, 1954.

Chapter 6

Design and fabrication of a compact vacuum bonding chamber for laboratory-scale electronics packaging experiments

6.1 Introduction

There are certain experimental studies that demand high temperature in a vacuum enviroment. These instruments can be utilized for the soldering and bonding process. At elevated temperature, oxidation of surfaces can impose challenges to the reliability and quality of joints being made, thus such instrumentation is extremely useful for bonding related studies. This was the motivation for the authors to design and construct a laboratory scale chamber that is capable of reaching high temperatures (approximately 400°C) and high vacuum levels (30 mtorr). This project was carried out in the first few months of the author's PhD studies and provided a valuable opportunity for learning a number concepts in mechanical design.

This chamber can be used for a variety of electronic packaging related applications. As mentioned, elevated temperature can induce oxidation of the molten solder and in the electronics packaging houses, fluxes are used extensively to avoid such oxidation reactions. With the help of the vacuum chamber discussed in this chapter fluxes are not needed anymore. Flux is an organic material used in nearly all soldering processes to remove oxides, thus making solder reaction possible.2 There are a variety of devices that cannot be exposed to flux, such as microelectromechanical systems MEMS, photonic, and biomedical devices. Thus, fluxless process becomes necessary for packaging these devices.

In the context of current dissertation since Indium, which is highly prone to oxidation was used as a component of the bonding layers, a bonding chamber capable of reaching medium vacuum levels is extremely crucial [1]. One way to form such high temperature vacuum environments is to place a small vacuum chamber inside a laboratory oven. The sample is loaded into the chamber that is pumped continuously to achieve the vacuum level required. The oven is then heated and the temperature of the sample is monitored. In this configuration, the heat would need to transport from the hot air in the oven to the sample inside the vacuum chamber. Specifically, the hot air heats up the chamber enclosure by convection. Inside the chamber, convection heat transfer from the wall to the sample is very small because of vacuum environment. Thus, the sample would have to be fastened onto the chamber wall and have adequate thermal contact. The temperature of the chamber enclosure is higher than the temperature of the sample. This causes a great challenge in sealing the feedthroughs and the ports of the vacuum chamber with O-rings or even with metallic seals. It also consumes a great deal of electrical power and takes a long time to reach the desirable temperature on the sample.

On the other hand, the design presented here, produces the vacuum within the furnace area, thus it is a much more efficient technique. In the following paragraphs an overview of design elements of the chamber is presented. Information provided here can be utilized in future for design and construction of similar furnaces with enhanced capabilities in the future.

6.2 Design features

Figure shows the actual furnace and initial Solidworks model used to design the equipment. The chamber consists of a quartz bell jar sitting on a stainless-steel plate, a heating platform, and a ceramic post. Its outer diameter of the bell jar is 26 mm, and its height is 30.5 cm with a thickness of 10 mm. The transparent cylinder allows us to have full view of the sample during operation. The interface between the cylinder and the steel plate is sealed by an L gasket. Three type-K thermocouples are used to measure the temperature at different locations within the chamber. One of the thermocouples is used by a temperature controller as its input, and thus, provides the process value of the controller. The controller switches the electricity applied to the heating platform on and off until the desired set point value is reached. Additional thermocouples can be utilized for screening the temperature on different areas of the specimen.

A Leybold model D16B mechanical pump is used to bring the chamber to near vacuum conditions during operation. 20 mtorr vacuum is achievable after pumping for 20 minutes.

Figure 6.1 vacuum bonding chamber after assembly (left) and initial model of chamber area prepared by Solidworks

The heating platform is a 75x75x10 mm^3 graphite block. This surface size provides the capability of annealing 3-inch wafers. Many holes were drilled into the platform to allow for resistive heating wire of nickel-chromium alloy to be looped around and integrated into the body of the block. Figure 3 shows the detailed design of the machined holes into the graphite block.

The wire is electrically insulated from the graphite using ceramic tubes. Graphite was chosen as the material of the platform because it is known to be a nearly perfect absorber and emitter of radiation. Therefore, the heating block is able to absorb the maximum amount of heat given off by the wires. It can also withstand very high temperatures.

The heater block needs to be thermally isolated from the base plates so that heat does not transfer to the temperature sensitive L gaskets. The polymer-based L gaskets and feedthroughs that are on the base plate are prone to high temperature degradation. Thus, the block is mounted on a ceramic post, whose other end is fixed at the base plate. Also, the

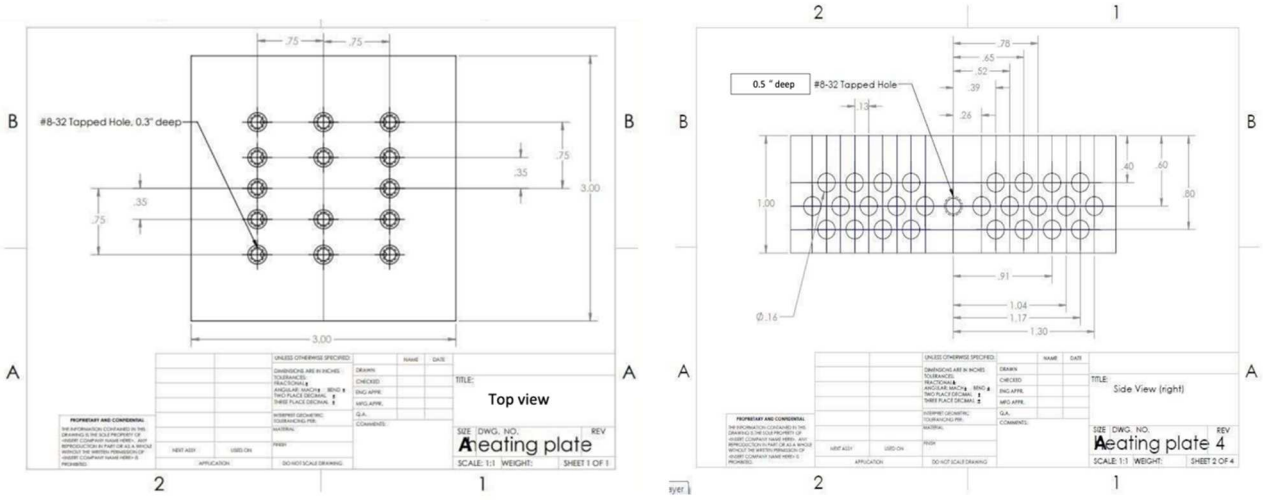

Figure 6.2 Dimension and placement of the holes machined into the graphite heating block (left) top view of the holes used for fixing the specimen on top (right) view of the side holes used for looping the resistive wire

maximum allowable distance/height between the heating block and the base plate was considered for the design for good thermal isolation between the heater and the base plate. The base plate has four ports. Figure 6.3 shows the detailed design and threading used for each feedthrough. Two of these are occupied by feedthroughs. One feedthrough is for a pair of copper wires to pass into the chamber to connect to the two ends of the heating wire. This will provide the driving current for the heating block. The two other feedthroughs are for thermocouple wires. The third port is used for the vacuum gauge, and the fourth port is for connecting to the mechanical pump. The plates are constructed of stainless steel because of its strength, cleanness, and ability to reflect and scatter radiation. By doing so, the plates will not absorb much heat radiation and can be cooled to low temperature with natural convection by ambient air.

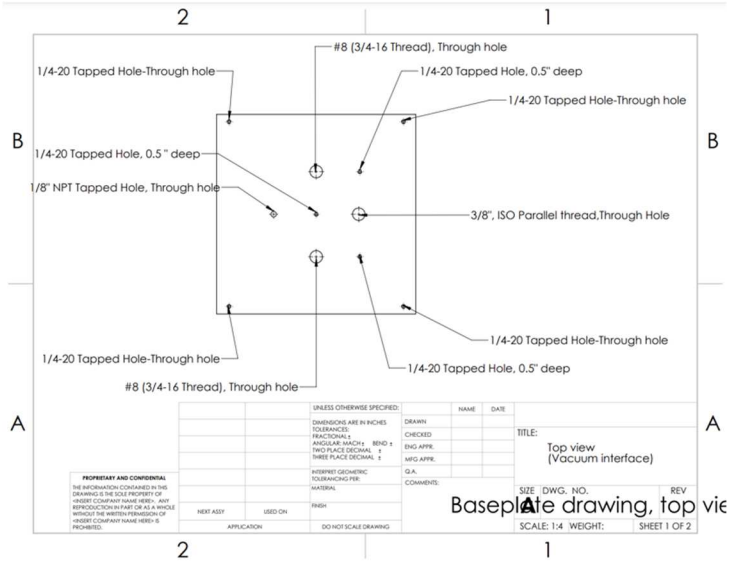

Figure 6.3 Dimension and placement of threaded holes machined into the Stainless-steel baseplate

6.3 Conclusion

This chamber was designed based on a version that was designed many years ago in Professor Chin C. Lee's research lab [2]. In the new design, we were able to provide better performance while using a much simpler design. The earlier version had two baseplates, one on top and one at the bottom, by using the bell jar the top plate is eliminated. This revision resulted in significant reduction in cost of production. Also, the earlier version used o rings that were placed into ring groves that were machined into the baseplate. By using L gaskets, the need for machining the base plate (for ring grove) was eliminated thus resulting in reduced cost of manufacturing. All in all, this vacuum bonding chamber was manufactured with a simple design and low cost. It has been used in all of the vacuum bonding processes mentioned in this dissertation and has proven to be a reliable instrument for laboratory-scale electronics packaging experiments.

References

[1] H. Schoeller and J. Cho, “Oxidation and reduction behavior of pure indium,” *J. Mater. Res.*, vol. 24, no. 2, pp. 386–393, Feb. 2009.

[2] C. C. Lee, D. T. Wang, and W. S. Choi, “Design and construction of a compact vacuum furnace for scientific research,” *Rev. Sci. Instrum.*, vol. 77, no. 12, p. 125104, Dec. 2006.

Chapter 7

Conclusions and future perspectives

This dissertation demonstrates the excellent potential of using silver-based systems for heterogenous integration of high-power photonics. In the context of OP-VECSEL packaging, Ag-In bonding technology is shown to be beneficial. Void free, thin joints can be made using Ag-In bonding that can help manage the thermal load of the VECSEl chip. Moreover, the low bonding temperature is shown to suppress thermomechanical stresses during fabrication. Developed Ag-In bonding technology is also shown to be a mechanically robust choice for integration of highly CTE mismatched components, in the case of this study, CVD diamond and copper. All of these advantages also come at a cost lower than conventional technologies that utilize gold based bonding techniques. Disadvantages such as void formation due to rapid consumption of Indium by silver prior to bonding can occur in this system, however prior to bond annealing of Ag is shown to be able to address this issue. Also, the very unique spinodal nanostructure observed in the Ag-In system can act as a nanocomposite that is able to suppress crack propagation and result in superior impact resistance.

Hence, the author believes that the developed Ag-In bonding system has significant potential for use in many high-power electronic and photonic devices due to all these unique characteristics. It is highly recommended that more studies on electrical and thermal properties of this system be done, so that this technology can find its place in commercially available devices.

The nano-silver sintering technique introduced, also has many compelling features such as simple synthesis, ease of dispense, low temperature sintering and the ability to form very

thin joints. These features can be utilized for many high-power devices, since superior heat dissipation can be guaranteed. The study on nano-silver sintering presented here, provides a very introductory picture of the capabilities of this system, thus the author believes more studies on the sintering mechanism and its long-term reliability are instrumental for further use of this technology.